LA-13299-MS

Approved for public release;
distribution is unlimited.

#69792

(45)

Simulations of Groundwater Flow and Radionuclide Transport in the Vadose and Saturated Zones beneath Area G, Los Alamos National Laboratory

MAY 17 2001

Los Alamos
NATIONAL LABORATORY

Los Alamos National Laboratory is operated by the University of California for the United States Department of Energy under contract W-7405-ENG-36.

16399

An Affirmative Action/Equal Opportunity Employer

This report was prepared as an account of work sponsored by an agency of the United States Government. Neither The Regents of the University of California, the United States Government nor any agency thereof, nor any of their employees, makes any warranty, express or implied, or assumes any legal liability or responsibility for the accuracy, completeness, or usefulness of any information, apparatus, product, or process disclosed, or represents that its use would not infringe privately owned rights. Reference herein to any specific commercial product, process, or service by trade name, trademark, manufacturer, or otherwise, does not necessarily constitute or imply its endorsement, recommendation, or favoring by The Regents of the University of California, the United States Government, or any agency thereof. The views and opinions of authors expressed herein do not necessarily state or reflect those of The Regents of the University of California, the United States Government, or any agency thereof. Los Alamos National Laboratory strongly supports academic freedom and a researcher's right to publish; as an institution, however, the Laboratory does not endorse the viewpoint of a publication or guarantee its technical correctness.

LA-13299-MS

Issued: July 1999

Simulations of Groundwater Flow and Radionuclide Transport in the Vadose and Saturated Zones beneath Area G, Los Alamos National Laboratory

Kay H. Birdsell
Kathleen M. Bower*
Andrew V. Wolfsberg
Wendy E. Soll
Terry A. Cherry
Tade W. Orr**

*Graduate Research Assistant at Los Alamos National Laboratory, Department of Geology/Geography, Eastern Illinois University, Charleston, IL
**Graduate Research Assistant at Los Alamos National Laboratory, US Geological Survey, Tumamoc Hill Project Office, 1675 W Anklam Road, Tucson, AZ 85745

Los Alamos
NATIONAL LABORATORY
Los Alamos, New Mexico 87545

TABLE OF CONTENTS

ABSTRACT 1
1. INTRODUCTION 3
2. STUDIES OF SPECIFIC FLOW PROCESSES 4
2.1 Addition of Deeper Vadose-Zone Units 4
2.1.1 Introduction and Problem Description 4
2.1.2 Hydrologic Properties and Their Effects 6
2.2 Effects of Transient Percolation 13
2.2.1 Modeling Approach 14
2.2.2 Transient Flow Results 16
2.2.3 Transient Transport Results 19
2.2.4 Summary of Transient Results 21
2.3 Fracture Flow 22
2.3.1 Single Fracture Modeling 22
2.3.2 Dual-Permeability Fracture Modeling 25
2.4 Evaporation 25
2.4.1 From Mesa Sides and Fractures 25
2.4.2 From Surge Beds 28
3. THREE-DIMENSIONAL VADOSE ZONE MODEL 30
3.1 Vadose-Zone Model Definition 30
3.1.1 Stratigraphy 31
3.1.2 Grid 32
3.1.3 Boundary Conditions 33
3.1.4 Hydrologic Properties 36
3.1.5 Transport Properties 36
3.1.6 Source Term 38
3.2 Vadose-Zone Flow Results 40
3.3 Vadose -Zone Transport Results 41
3.3.1 Downward Transport toward the Water Table 45
3.3.1.1 Base-Case Flow Field 45
3.3.1.2 Other Flow Fields 47
3.3.2 Lateral Transport toward the Mesa Sides 50
3.3.2.1 Base-Case Flow Field 50
3.3.2.2 Other Flow Fields 54

3.3.3 Generic Transport Calculations for Nonradiological Contaminant 56
3.3.3.1 Simulation Results 56
3.3.3.2 Discussion of Generic Cases 60
4. THREE-DIMENSIONAL SATURATED ZONE MODEL 61
4.1 Saturated Zone Model Definition 61
4.1.1 Geology and Hydrogeology 61
4.1.2 Grid 63
4.1.3 Boundary Conditions 63
4.1.4 Hydrologic and Transport Properties 65
4.2 Saturated-Zone Flow Results 65
4.3 Saturated-Zone Transport Results 66
4.3.1 Downward Transport toward the Water Table 66
4.3.2 Lateral Transport toward the Mesa Side 68
4.3.3 Dose Assessment 68
5. UNCERTAINTY 70
5.1 Vadose-Zone Flow 70
5.2 Saturated-Zone Flow 72
5.3 Transport Properties 72
6. CONCLUSIONS 73
ACKNOWLEDGMENTS 74
REFERENCES 75

LIST OF FIGURES

Figure 2.1-1. Cross section of Western MDA G used for 2-dimensional simulations.

Figure 2.1-2. Comparison of site data to calculated steady-state saturation profiles for several infiltration rates. Calculated profiles are located at the center of the cross section.

Figure 2.1-3. Comparison of site data to calculated steady-state saturation profiles at 1 mm/yr using various hydrologic properties for the Guaje Pumice and the Cerros del Rio Basalts. Calculated profiles are located at the center of the cross section.

Figure 2.1-4. Simulated solute pathways for the two-dimensional cross section shown in Figure 2.1-1, a) particle release only at mesa top, matrix-type basalt properties, b) particle release at mesa top and canyon floor, matrix-type basalt properties, c) particle release at mesa top, fracture-type basalt properties.

Figure 2.1-5. Contaminant plume with and without lateral flow along the Guaje Pumice Bed.

Figure 2.1-6. Flux-versus-time curves at the water table for the plumes shown in Figure 2.1-5. The equivalent continuum basalt properties give more conservative transport results.

Figure 2.2-1. Two-dimensional cross section used for numerical simulations, modified to indicate five waste disposal pits.

Figure 2.2-2. Variation in saturation with time for the steady and four transient simulations at various depths.

Figure 2.2-3. Source term for the C-14 decay chain based on a pit infiltration rate of 4 mm/yr.

Figure 2.2-4. Cumulative breakthrough curve for C-14 to the Guaje Pumice for four transient infiltration simulations and one steady infiltration simulation.

Figure 2.3-1. System configuration for fracture flow study.

Figure 2.4-1. Problem setup for the study of evaporative effects from mesa sides and from fractures.

Figure 2.4-2. Resulting saturation profiles for evaporation along a mesa edge and from fractures with 5-m and 10-m spacing, Unit 2.

Figure 2.4-3. Resulting Saturation Profiles for Evaporation along a Mesa Edge and from fractures with 5-m and 10-m spacing, Unit 1v-u.

Figure 2.4-4. Resulting saturation profile for evaporation along the surge beds at the Unit 2/1v-u interface compared to that for infiltration alone.

Figure 2.4-5. Resulting capillary pressure profile for evaporation along the surge beds at the Unit 2/1v-u interface compared with infiltration alone and with data from Rogers et al. (1995) for Borehole G-5.

Figure 3.1-1. Three-dimensional stratigraphy for the vadose-zone model of Area G.

Figure 3.1-2. Pit boundaries, internal pit nodes, and mesa edge nodes for the three-dimensional vadose-zone calculations.

Figure 3.1-3. Boundary condition map of the topographic surface for the vadose-zone flow and transport calculations.

Figure 3.1-4. Bottom boundary divided into 28 regions for which temporally and spatially dependent flux from the vadose-zone calculation is reported.

Figure 3.1-5. Velocity-dependent portion of the rapid-release source term.

Figure 3.2-1. Steady-state vadose-zone saturation field (top view) for the base-case flow field.

Figure 3.2-2. Saturation profiles near Pit 1 for the three mesa-top infiltration rates.

Figure 3.2-3. Saturation profiles for the base-case flow rate (5_1_50) at the three locations of interest.

Figure 3.3-1. I-129 plumes (concentration, moles/liter) in the vadose zone at 1000 years for the four different source regions, base-case flow field.

Figure 3.3-2. Total flux of C-14 from the vadose zone to the saturated zone from the four source regions, base-case flow field (5_1_50).

Figure 3.3-3. Total flux of I-129 from the vadose zone to the saturated zone from the four source regions, base-case flow field (5_1_50).

Figure 3.3-4. Total flux of Tc-99 from the vadose zone to the saturated zone from the four source regions, base-case flow field (5_1_50).

Figure 3.3-5. Total flux of the historical I-129 inventory from the vadose zone to the saturated zone for various flow cases.

Figure 3.3-6. Total flux of (a) C-14, (b) I-129, and (c) Tc-99 from the vadose zone to the saturated zone for the highest flow case (10_5_100) from the four source regions.

Figure 3.3-7. Total flux of (a) C-14, (b) I-129, and (c) Tc-99 from the vadose zone to the saturated zone for the lowest flow case (1_1_20) from the four source regions.

Figure 3.3-8. Total lateral flux of C-14 toward the mesa sides along (a) Cañada del Buey and (b) Pajarito Canyon from the four source regions, base-case flow field (5_1_50).

Figure 3.3-9. Total lateral flux of I-129 toward the mesa sides along (a) Cañada del Buey and (b) Pajarito Canyon from the four source regions, base-case flow field (5_1_50).

Figure 3.3-10. Total lateral flux of Tc-99 toward the mesa sides along (a) Cañada del Buey and (b) Pajarito Canyon from the four source regions, base-case flow field (5_1_50).

Figure 3.3-11. Generic total flux from the canyon floors through the vadose zone to the saturated zone for an extreme case of lateral transport. Pajarito Canyon (south) flow rate is 50 mm/yr. Cañada del Buey (north) flow rate is 1 mm/yr.

Figure 3.3-12. Generic total flux from the floor of Pajarito Canyon through the vadose zone to the saturated zone for an extreme case of lateral transport. Pajarito Canyon flow rates are 100 mm/yr, 50 mm/yr, and 20 mm/yr.

Figure 3.3-13. Total flux from the unsaturated zone as a function of Kd-generic contaminant (Co = 1), released from the historic pits and shafts, base-case flow field.

Figure 3.3-14. Total flux from the unsaturated zone as a function of Kd-generic contaminant (Co = 1), released from the historic pits and shafts, highest flow field.

Figure 3.3-15. Total flux from the unsaturated zone as a function of Kd-generic contaminant (Co = 1), released from the oldest pits and shafts, base-case flow field.

Figure 3.3-16. Total flux from the unsaturated zone as a function of Kd-generic contaminant (Co = 1), released from the historic pits and shafts, base-case flow field.

Figure 4.1-1. Three-dimensional finite element grid used for the saturated-zone flow and transport calculations.

Figure 4.1-2. Saturated-zone model configuration.

Figure 4.3-1. Historic I-129 plume (concentration, moles/liter) in the aquifer for the base-case, vadose-zone flow field: (top) side view at 1,000 years, (middle) top view at 1,000 years, (bottom) top view at 10,000 years.

Figure 4.3-2. Concentrations in the saturated zone for the I-129 historic inventory at the point of maximum concentration and at the 100-m compliance point with the base-case flow field in the vadose zone.

Figure 4.3-3. Time-dependent concentration plots for the generic case of lateral transport at the location of maximum concentration in the saturated zone.

LIST OF TABLES

Table 2.1-1. Hydrologic properties.

Table 2.2-1. Statistics of pit percolation over the first 5000 years used for transient simulations.

Table 2.2-2. Comparison of C-14 arrival times and peak concentrations for the steady and four transient flow simulations.

Table 3.1-1. Infiltration rates (mm/yr) used as upper boundary conditions.

Table 3.1-2. Median distribution coefficients Kd mg/gP for nuclides on intact and crushed, unsaturated Bandelier Tuff and on saturated samples.

Table 3.1-3. Disposal unit classification and location.

Table 3.3-1. Scale factors to correct generic concentration breakthrough curve for each nuclide and waste category using the base case flow field (5_1_50).

Table 3.3-2. Scale factors to correct generic concentration breakthrough curve for each nuclide and waste category using the highest flow rate (10_5_100).

Table 3.3-3. Scale factors to correct generic concentration breakthrough curve for each nuclide and waste category using the lowest flow rate (1_1_20).

Table 3.3-4. Minimum Kd value required to result in a contaminant flux of 10^{-3} times the peak flux value after 1,000 years of migration.

Table 4.3-1. Maximum ground water and all-pathways doses for the PA and CA wastes, base case flow field.

SIMULATIONS OF GROUNDWATER FLOW AND RADIONUCLIDE TRANSPORT IN THE VADOSE AND SATURATED ZONES BENEATH AREA G, LOS ALAMOS NATIONAL LABORATORY

by

Kay H. Birdsell, Kathleen M. Bower,
Andrew V. Wolfsberg, Wendy E. Soll,
Terry A. Cherry, and Tade W. Orr

ABSTRACT

Numerical simulations are used to predict the migration of radionuclides from the disposal units at Material Disposal Area G through the vadose zone and into the main aquifer in support of a radiological performance assessment and composite analysis for the site. The calculations are performed with the finite element code, FEHM. The transport of nuclides through the vadose zone is computed using a three-dimensional model that describes the complex mesa top geology of the site. The model incorporates the positions and inventories of thirty-four disposal pits and four shaft fields located at Area G as well as those of proposed future pits and shafts. Only three nuclides, C-14, Tc-99, and I-129, proved to be of concern for the groundwater pathway over a 10,000-year period. The spatial and temporal flux of these three nuclides from the vadose zone is applied as a source term for the three-dimensional saturated zone model of the main aquifer that underlies the site. The movement of these nuclides in the aquifer to a downstream location is calculated, and aquifer concentrations are converted to doses. Doses related to aquifer concentrations are six or more orders of magnitude lower than allowable Department of Energy performance objectives for low-level radioactive waste sites.

Numerical studies were used to better understand vadose-zone flow through the dry mesa-top environment at Area G. These studies helped define the final model used to model flow and transport through the vadose zone. The study of transient percolation indicates that a steady flow vadose-zone model is adequate for computing contaminant flux to the aquifer. The fracture flow studies and the investigation of the effect of basalt and pumice properties helped us define appropriate hydrologic properties for the modeling. Finally, the evaporation study helped to justify low infiltration rates.

1 INTRODUCTION

Transport calculations are used to predict the long-term migration rates of water-soluble radionuclides and nonradiological constituents at Material Disposal Area G (MDA G) at Los Alamos National Laboratory (LANL) to the main aquifer that underlies the site. The calculations support a radiological performance assessment (PA) and composite analysis (CA) for this low-level radioactive solid waste (LLW) site (Hollis et al., 1997) as well as a site assessment of metals migration. The PA considers those wastes buried since September 1988, and those projected to be buried through facility closure, which is projected to be in 2044. The CA considers all radioactive wastes buried at the site since its inception in 1957 through facility closure. The distinction of these wastes is driven by regulatory considerations as described in the formal Area G PA/CA (Hollis et al., 1997). The calculations span a 10,000-year time period in order to predict transport to the aquifer for the required 1,000-year compliance period along with a 10,000-year uncertainty period. We examine the flow behavior of the site in order to predict radionuclide migration from the site through the vadose or unsaturated zone and into the main aquifer that underlies Area G. All calculations presented in this report are run with the finite element code FEHM (Zyvoloski, 1995), which simulates fluid flow, heat transport, and contaminant transport through porous and fractured media.

Before the vadose-zone calculations are performed, we study some of the factors that complicate the prediction of flow and transport in the vadose zone (Section 2.0 of this report). These factors include (1) uncertainties in hydrologic properties for the deeper vadose-zone units (Section 2.1), (2) the effects of transient percolation through the mesa top, including the disposal pits (Section 2.2), (3) the effects of infiltration into fractures (Section 2.3), and (4) the effects of evaporation from the mesa sides, fractures and surge beds (Section 2.4). These studies helped to determine (1) the hydrologic properties that are used for the final vadose-zone flow and transport calculations, (2) that a steady-flow model is adequate to perform the PA/CA simulations, (3) that transport through fractures has a minimal effect on the calculation of flux to the saturated zone, and (4) that evaporative effects can reasonably account for the low moisture content observed in the mesa-top units at the site and justify a small infiltration value. These results support the subsequent assumptions used for predictions of flow and transport of radionuclides through the vadose zone.

The transport calculations are performed in two parts. In Section 3, we compute the transport of nuclides and nonradiological metals through the vadose zone using a three-dimensional model that describes the complex mesa-top geology of the site. Infiltration is assumed to be steady, although the mesa top and two canyons that border Area G receive different infiltration rates. Results for a base-case flow field are compared to those for some variations on the flow field as part of an uncertainty analysis. The model incorporates the position and inventories of nuclides from the thirty-four disposal pits and four shaft fields already located at Area G along with those of four future pits and another shaft field. Two pathways are considered. One is downward migration through the vadose zone to the aquifer. The other is lateral migration to the mesa sides, deposition into the nearby canyon, and subsequent migration through the vadose zone to the aquifer. In these simulations, only three nuclides, C-14, I-129, and Tc, reach the water table by either of the two pathways during the 10,000-year period considered in this study. These nuclides are nonsorbing. The remainder of the nuclides have distribution coefficients that retard their migration so that they remain within the vadose zone for a period greater than 10,000 years. Time and spatially dependent results for the

flux of the three nuclides from the vadose zone feed the saturated-zone model. The transport of nonradioactive metals is calculated through a series of generic simulations that are used to determine the threshold sorption coefficients that result in breakthrough to the water table.

In Section 4, the continued migration of nuclides into the main aquifer is calculated again using a three-dimensional, steady-flow model. This model has a simple configuration but maintains the spatial and temporal distribution of nuclide flux from the vadose zone. Preliminary results for the PA and CA dose assessments are made. Simulated doses related to aquifer concentrations are several orders of magnitude smaller than DOE performance objectives for LLW sites. In Section 5, we discuss the uncertainties associated with the predictions presented in this report. Finally, the conclusions are summarized in Section 6.

2 STUDIES OF SPECIFIC FLOW PROCESSES

2.1 ADDITION OF DEEPER VADOSE-ZONE UNITS

2.1.1 Introduction and Problem Description

This introduction summarizes a previous work (Birdsell et al., 1995) in order to explain the need for adding detail to the model of the deep, vadose-zone hydrologic units. To choose appropriate infiltration rates for Area G, simulated saturation profiles for a number of different infiltration rates were compared to site field data. The study used a two-dimensional cross section defined by Krier (Krier et al., 1996) as shown in Figure 2.1-1. We assumed steady infiltration along the mesa top. Several infiltration rates were applied uniformly over the top of the mesa as shown in Figure 2.1-1: 1.0 cm/yr, 0.1 cm/yr, 0.01 cm/yr, 0.001 cm/yr, and 0.0 cm/yr.

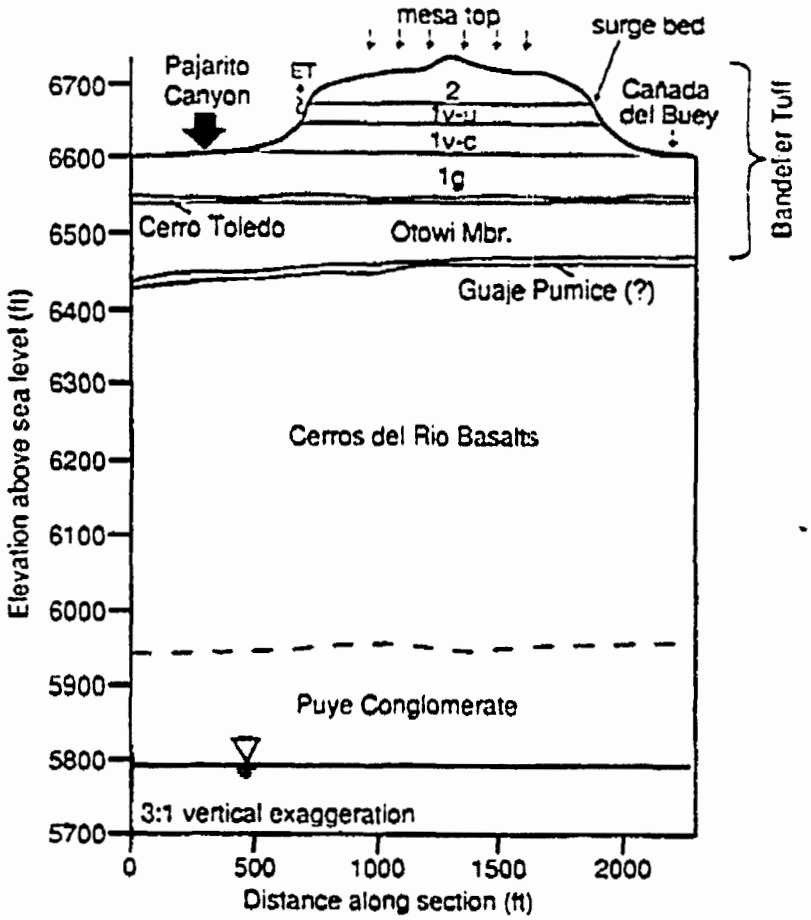

Figure. 2.1-1. Cross section of western MDA G (based on Krier et al., 1996) used for the two-dimensional simulations.

Evaporation and runoff from the mesa top were indirectly accounted for in the assumed low infiltration rates that are much lower than the average precipitation rate measured at MDA G, 35.6 cm/yr (Bowen, 1990). Mean hydrologic properties (Krier et. al, 1995) were assigned from Units 2 down through the Otowi Member. These properties are shown in Section 2.1.2. Originally, hydrologic properties for the Otowi Member were assigned to the Guaje Pumice, the Cerros del Rio basalts, and the Puye Conglomerate because no information was available for those units.

Figure 2.1-2 shows calculated steady-state saturation profiles at the center of the mesa for the five infiltration rates discussed above. The measured *in situ* saturation data are also shown. The simulation results are compared to saturation data from Unit 2 down through the Otowi Member. Here we see that the shape of the curves mimic the shape of the data (e.g., saturations decrease from Unit 2 to

Unit 1v-u and then increase again in Unit 1v-c, etc.). However, no single infiltration rate fits through the entire set of saturation data. Results for the lowest infiltration rates (0.001 and 0.0 cm/yr) most closely match the site saturation data in Units 2 and 1v-u, the two mesa-top units. Higher infiltration rates (0.1 and 0.01 cm/yr) are needed to match the saturation data from Units 1v-c and 1g, and an even higher rate (~1 cm/yr) is needed to match the data in the Cerro Toledo and Otowi Member.

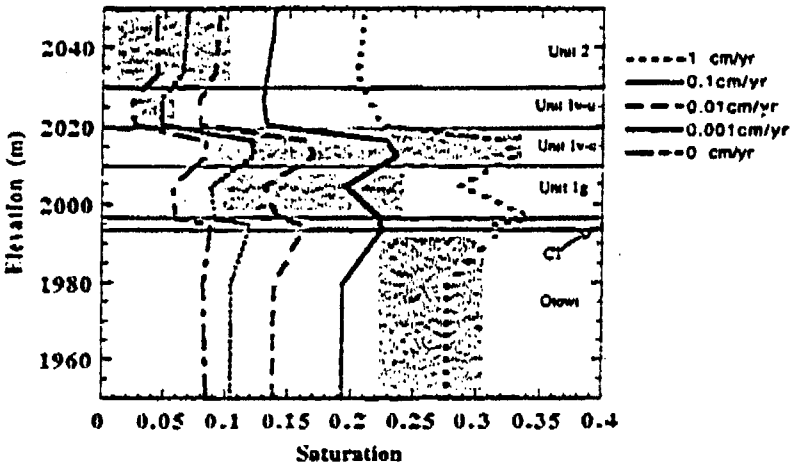

Figure 2.1-2. Comparison of site data (gray boxes) to calculated steady-state saturation profiles for several infiltration rates. Calculated profiles are located at the center of the cross section.

In the current study, we build upon the previous study by assigning hydrologic properties to the three deepest vadose-zone units, the Guaje Pumice, the Cerros del Rio Basalt, and the Puye Conglomerate, to test the effect of the addition of these layers on flow (specifically, its effect on the calculated saturation in the Otowi Member) and on transport at the site. This addition was suggested by a Department of Energy (DOE) Peer Review Committee (Hollis et al., 1997) after reviewing a previous draft of the PA.

2.1.2 Hydrologic Properties and Their Effects

As mentioned above, the mean hydrologic properties supplied by Krier et al. (1996) are used for Units 2 down through the Otowi Member. Unsaturated hydrologic parameters for a single core of Guaje pumice were measured and added to the model. These properties, as well as those used for the deeper units, are given in Table 2.1-1. In addition, estimates of *in situ* saturation in the Guaje Pumice bed are now available. Gravimetric moisture measured for samples from the Gauje Pumice bed in wells 54-1015 and 54-1016 (Krier, personal communication, 1996) range from 13.7% to 28.3%. Using a bulk density and porosity measured on a different sample (Springer, personal communication, 1996), this converts to saturations ranging from 0.17 to 0.34.

Table 2.1-1. Hydrologic properties			
Unit	Ksat (cm/s)	porosity	van Genuchten θ_r, α (cm^{-1}), n
Unit 2[a]	4.27×10^{-4}	0.481	0.013, 0.0060, 1.890
Unit 1v-u[a]	1.48×10^{-4}	0.517	0.002, 0.0030, 1.932
Unit 1v-c[a]	1.67×10^{-4}	0.509	0.009 0.0033,1.647
Unit 1g[a]	1.88×10^{-4}	0.480	0.006, 0.0053, 1.745
Cerro Toledo[a]	8.65×10^{-4}	0.473	0.008, 0.0152, 1.506
Otowi Member[a]	2.49×10^{-4}	0.435	0.0188, 0.0059, 1.713
Guaje Pumice[b]	1.5×10^{-4}	0.667	0.0, 0.00081, 4.0264
Puye Formation[d,e]	4.6×10^{-3}	0.25	0.045, 0.145, 2.68
Cerros del Rio basalts[c] (matrix only)	9.7×10^{-5}	0.228	0.015, 0.0384, 1.474
Cerros del Rio basalts[c] (fracture properties) (equivalent continuum)	9.7×10^{-5} 9.7×10^{2}	1×10^{-4} 1×10^{-4}	6.6×10^{-6}, 0.0384, 1.474 3.0×10^{-6}, 0.0384, 1.474

[a]Mean values from Krier et. al, 1996, [b]E. Springer (personal communication, 1996), [c]Bishop (1991), [d]Purtymun (1984), [e]Carsel and Parrish (1988).

Very little hydrologic data are available for the Cerros del Rio Basalts or for the Puye Conglomerate. Samples collected from the basalts display wide variability (Turin, 1995) ranging from extremely dense with no apparent porosity, to highly fractured, to vesicular so as to appear foamy. This variability leads to large uncertainty in calculating flow and transport through this unit because, without further characterization, we cannot predict whether the hydrologic properties of the matrix or of the fractures control water flow in this unit.

Our method for modeling the basalt has evolved as our understanding of the system sensitivity to this unit's properties has increased. Originally, the basalt was modeled as an intact matrix material with properties based on analysis of a vesicular basalt located beneath Idaho National Engineering Laboratory (Bishop, 1991) (Table 2.2-1, *matrix only*). The air entry pressure, $1/\alpha$, for the matrix basalt material is significantly greater than for the overlying pumice in our study. Also, the saturated hydraulic conductivity is slightly lower. These two factors lead to significant lateral flow in the overlying pumice bed that yields high pumice saturations and increased saturation in the Otowi Member as shown in Figure 2.1-3. The saturation in the Guaje Pumice bed reaches a value of 0.8, which is significantly higher than the data suggest.

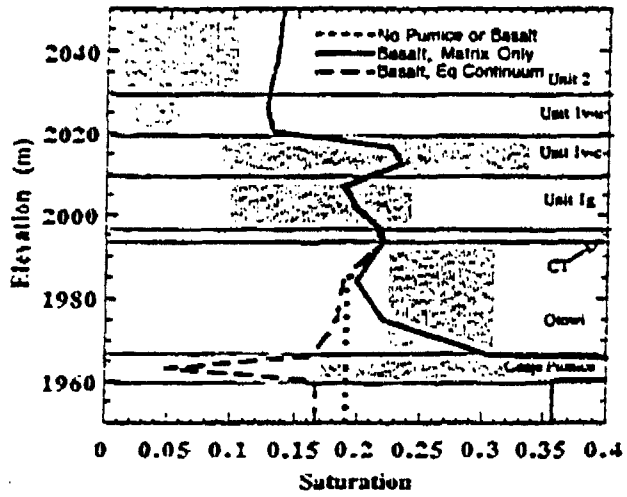

Figure 2.1-3. Comparison of site data (gray boxes) to calculated steady-state saturation profiles at 1 mm/yr using various hydrologic properties for the Guaje Pumice and the Cerros del Rio Basalts. Calculated profiles are located at the center of the cross section.

In the two-dimensional cross section (Figure 2.1-1), the water flows downdip through the pumice bed until it encounters water entering from Pajarito Canyon where it is diverted vertically. The position of this diversion is highly sensitive to the infiltration rates through the mesa top and in the two canyons. Figure 2.1-4 shows results for particle tracking calculations performed on the two-dimensional cross section. In Figure 2.1-4(a), particles released from the center of the mesa travel vertically to the Guaje Pumice, then downdip laterally in the pumice bed. Their lateral movement ceases, and they move vertically again when they encounter the effects of flow coming in from Pajarito Canyon. This is demonstrated in Figure 2.1-4(b) where particles are released in Pajarito Canyon as well as from the mesa top using the same flow field. The particles from the canyon travel vertically and laterally to the location where the mesa top particles stop traveling laterally, thus indicating the divide for the water coming from the two source locations. All of the particles are forced downward at the location where the mesa top and canyon flow fields merge. The no-flow side boundary plays an important role in this result. Figure 2.1-4(c), to be discussed later, shows the effects on particle transport when the fracture permeability of the basalts is increased. In the three-dimensional model of the site, the pumice bed dips toward the southwest. Simulated flow runs laterally toward the southwest end of the grid where it is diverted downward along the no-flow western boundary. This is demonstrated with the plume shown in Figure 2.1.-5(a).

Because the lateral flow in both the two- and three-dimensional simulations is so strongly controlled by the no-flow side boundary conditions, the behavior is considered to be unsatisfactory. Our uncertainty about the flow field in these two layers prompted a sensitivity study performed by Soll (Birdsell et al., 1997, Appendix A). The study considered a three-layered system consisting of the Otowi Member, the Guaje Pumice, and the Cerros del Rio Basalt. Various system characteristics were varied, such as the thickness, slope, and hydraulic conductivity of the pumice bed and the hydraulic conductivity of the basalt layer to determine which factors most strongly affect lateral flow in the pumice bed. The simulations show that the basalt conductivity has the strongest influence on lateral flow. With the matrix properties shown in Table 2.2-1, the basalt acts as a barrier, thus diverting flow laterally in the overlying pumice bed. By increasing the basalt conductivity or adding fracture characteristics, fluid can more readily enter the basalt, thus minimizing the diversion. Sensitivities to the thickness, slope, and conductivity of the pumice layer were secondary.

We expect that dense, unfractured basalt acts as a barrier that promotes lateral flow in the pumice bed in some places, although fractured basalt acts as a conduit for fast vertical flow in others, but the spatial distribution of basalt properties at this site is unknown. There is probably some lateral transport in the Guaje Pumice bed with a corresponding increase in the saturation of the overlying Otowi Member. However, this is a conceptualization and cannot be quantified with available data. Therefore, we have chosen to assign equivalent continuum properties that are dominated by fracture flow to the basalt. This modification leads to fast travel times through the basalt and eliminates lateral flow in the pumice layer, thus resulting in conservative transport results. However, as shown in Figure 2.1-3, this also yields pumice saturations that are lower than the measured values and decreases the calculated saturation in the Otowi Member. The matrix only and equivalent continuum curves shown in Figure 2.1-3 represent the end members for flow regimes in these deeper units: the basalt acting as a barrier to flow and the basalt acting as a conduit. Because the pumice saturation lies between these two end members, our hypothesis that the behavior of the basalt lies between these two extremes is supported.

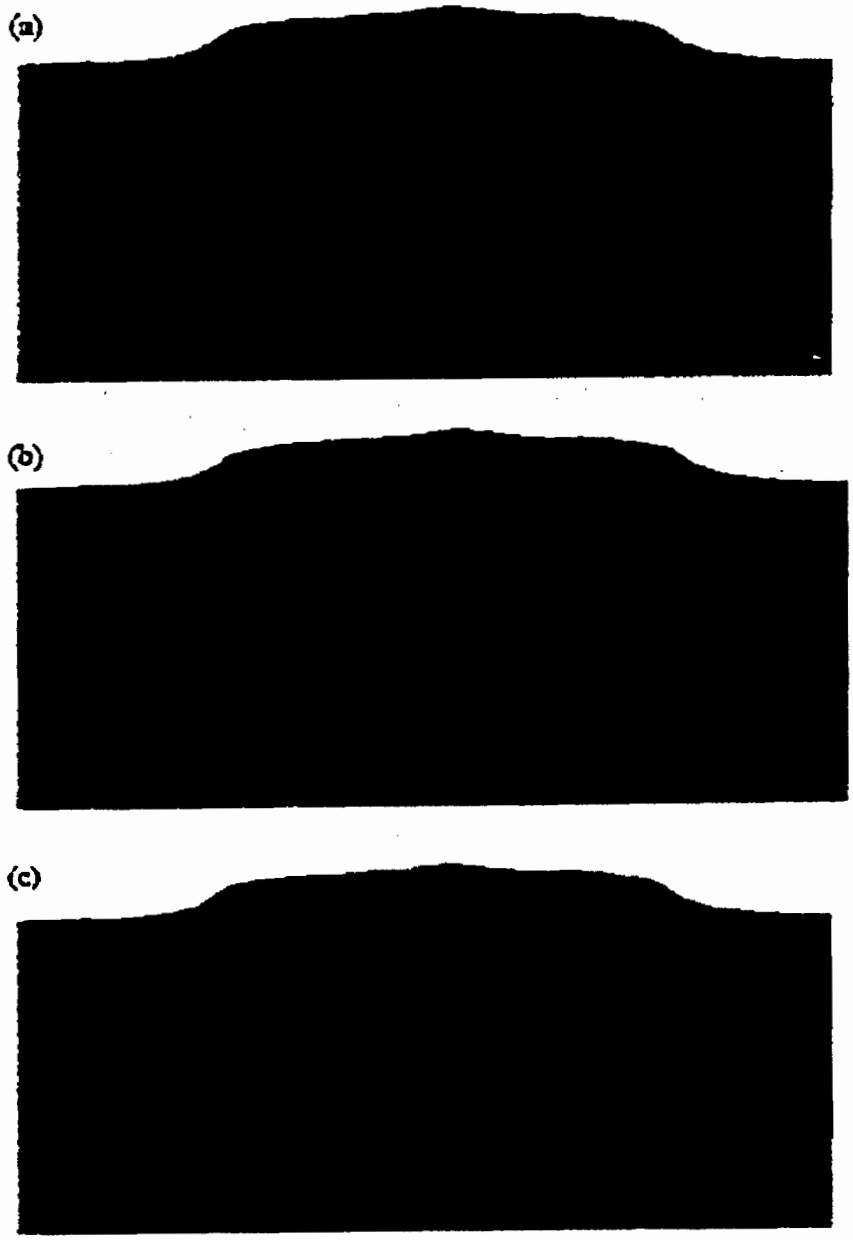

Figure 2.1-4. Simulated solute pathways for the two-dimensional cross section shown in Figure 2.1-1, (a) particle release only at mesa top, matrix-type basalt properties, (b) particle release at mesa top and canyon floor, matrix-type basalt properties, (c) particle release at mesa top, fracture-type basalt properties.

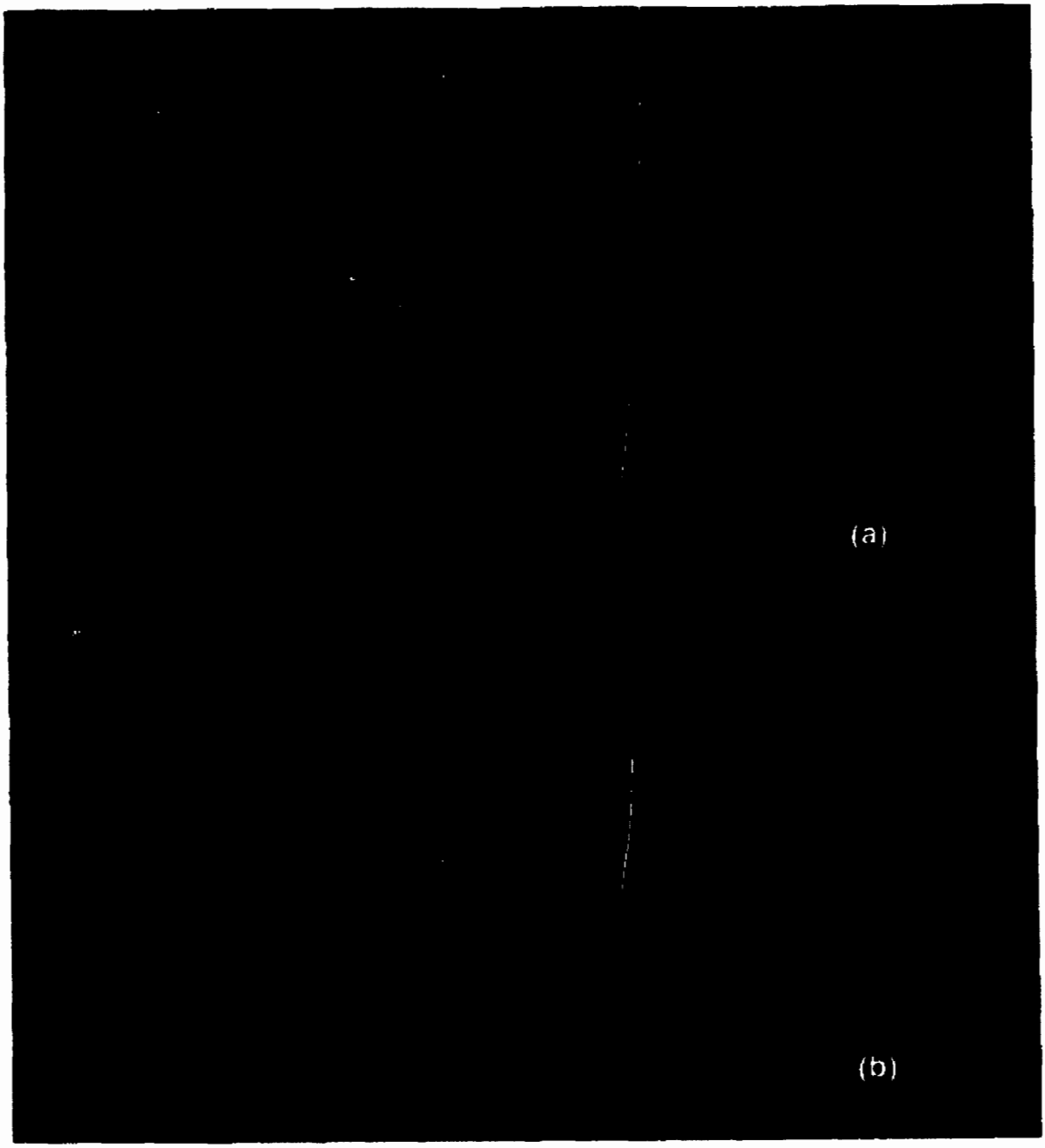

Figure 2.1-5. Contaminant plume (a) with and (b) without lateral flow along the Guaje Pumice Bed.

In order to obtain the fast basalt travel times, we conservatively treat the basalts as a system dominated by vertical fracture flow. This is done by modeling the basalt as an equivalent-continuum medium, (Table 2.2-1, *equivalent continuum)* made up of both fractures and matrix material (Klavetter and Peters, 1986). Matrix properties are derived from the analogue basalts in Idaho (Bishop, 1991). Fracture properties are chosen so that no lateral diversion occurs at the top of the basalts, even if the flow exceeds the matrix, saturated hydraulic conductivity. Then, because it is not known under which conditions fracture flow actually initiates, matrix and fracture porosity are set equal to the fracture volume fraction, 10^{-4}, to ensure rapid transport of one to five years through this unit, hence forgoing any retardation due to matrix flow or sorption. This treatment of transport through the basalt yields a conservative PA result (e.g., faster groundwater travel times and higher peak doses than actually expected). The basalts are also assumed to be nonsorbing, consistent with the assumption of rapid transport through this unit. Figures 2.1-4.(c) and 2.1-5.(b) respectively show the resulting two-dimensional particle tracking profile and a three-dimensional plume using these modified basalt properties. Figure 2.1-6 shows flux-versus-time curves at the water table for the two plumes in Figure 2.1-5. The dose assessment considers saturated-zone concentrations at a location 100 meters down gradient from the Area G fence line, as is discussed further in Section 4.3.3. That location is east of Area G. As shown in Figure 2.1-5, the plume that travels downward lies closer to the eastern end of Area G. This plume would reach the monitoring point more quickly and undergo less dilution and dispersion than the plume that flows laterally toward the west along the unsaturated pumice bed. The use of the equivalent-continuum basalt properties is therefore a good approach for handling the uncertainty associated with this unit's properties.

Adding additional conservatism to the model, the porosity of 10^{-4} may be up to two orders of magnitude lower than the fracture porosity of the Cerros del Rio basalts (Rogers, personal communication, 1996), leading to simulated ground water travel times up to 100 times faster than might actually occur in this unit. With better characterization of the Cerros del Rio basalts, less-conservative travel times could be simulated in which solute retarding processes of matrix flow and transport, diffusion from fractures to matrix material, and lateral diversion at the pumice/basalt interface are incorporated in the model.

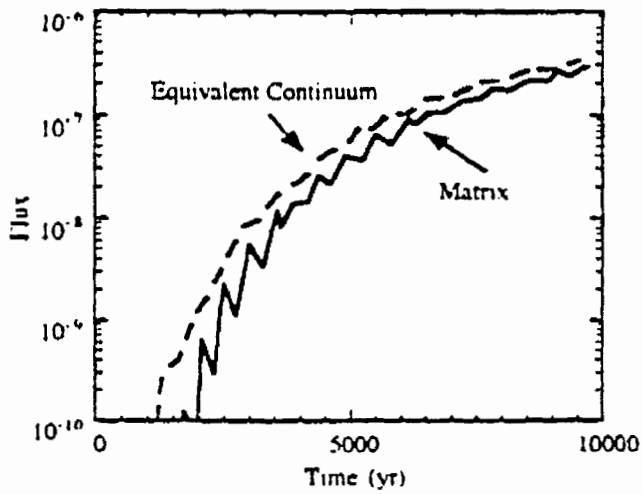

Figure 2.1-6. Flux-versus-time curves at the water table for the plumes shown in Figure 2.1-5. The equivalent continuum basalt properties yield more conservative transport results.

Although hydrologic properties for the Puye Conglomerate are unknown, we expect flow through this unit to be similar to that through coarse sand. Therefore, we estimate properties that lead to a conservative (faster than expected) travel time through the Puye Conglomerate that is not virtually instantaneous, as it is in the basalts. The layer is modeled as a coarse sand (Carsel and Parrish, 1988) with the porosity reduced by 60% (from 0.43 to 0.25) to account for cobbles and gravel that reduce the available pore space.

2.2 EFFECTS OF TRANSIENT PERCOLATION

The near-surface moisture balance in the mesa tops on the Pajarito Plateau is controlled by alternating periods of episodic infiltration and normal drying cycles (Rogers et al., 1997, Turin et al., 1995). Results presented by Springer (1996) indicate that such episodic events lead to transient percolation rates through the disposal pits at Area G. In this section, the system response to transient flow is estimated by applying transient percolation rates to the pits as well as to the undisturbed, upper surface of the mesa. The effects of the transients on the saturation distribution throughout the mesa and on radionuclide transport to the base of the Otowi Member are examined with these simulations. The value of such calculations is to evaluate the efficacy of the steady-state assumption against the transient conditions. Namely, these calculations serve to investigate whether the steady-flow approximation conservatively predicts contaminant transport rates even though moisture actually enters the system episodically.

12

An assumption of this study is that if fluctuations in flow are damped at depth and if cumulative contaminant flux for the transient runs is similar to that for the steady-flow run, then the subsequent dose calculated from the transient flow and steady-flow simulations will be similar. The purpose is to determine whether the transient and steady results are essentially the same. If the results prove to be similar, then steady-flow simulations can be run to address compliance issues. Use of a steady flow field for these simulations is desirable because the time step size for the transient-flow runs is limited by the yearly or possibly daily fluctuations in the flow field. This time step limitation makes the transient flow runs far more computationally intensive than the steady-flow runs. As a result, it would prove difficult to complete the entire suite of simulations required for the Area G PA using transient flow fields.

2.2.1 Modeling Approach

In order to study the effects of transient percolation on flow and transport at Area G, a number of transient-flow simulations are run, and the results are compared to those for a steady-flow simulation that uses the average percolation rate. Moisture profiles at various depths and solute transport rates are compared. C-14 is one of the fastest moving nuclides because it is nonsorbing. Cumulative breakthrough to the Guaje Pumice for this nuclide under steady- and transient-flow conditions is calculated. The simulations are performed for 5000 years, which proved to be a long enough time period for saturations to dampen at depth and for the cumulative breakthrough curves to level out.

The computational grid for these studies is also based on the north-south, two-dimensional cross section of Krier et al. (1996) shown in Figure 2.1-1. This study also uses the hydrologic properties shown in Table 2.1-1 with the "matrix only" properties for the Cerros del Rio Basalts. The calculations were performed before the choice of the equivalent continuum basalt properties for the final vadose-zone flow model, as described in Section 2.1.2. However, the basalt properties are not of great importance here because the analysis is based on breakthrough at the top of the Guaje Pumice bed. The extensive lateral flow in the pumice layer that occurs for the given pumice and basalt properties complicates the interpretation of breakthrough to the deeper layers or to the water table. If contaminant fluxes compare well at this horizon, they should compare well at deeper horizons.

In this study, it is assumed that fracture flow is not induced, even during high flow years, because sustained high flow rates would be required to increase the very low saturations at the site to near-saturated conditions. Therefore, fracture properties are not considered. Orr has further studied this issue through some one-dimensional modeling (Birdsell et al., 1997, Appendix B). The study looks at steady and transient flow through this same system using a dual permeability approach (Zyvoloski, 1995) that accounts for fractures in the two upper units (Unit 2 and Unit 1v-u). With these studies, we find that groundwater travel times to the top of the basalt layer through the fractured system do not vary by more than 100 years from the unfractured system, even when applying transient infiltration rates. Therefore, the two-dimensional calculations are performed with matrix-only properties.

Although the matrix-only properties may seem to misrepresent the system and limit the study, many studies performed for the Yucca Mountain Site Characterization Project (Klavetter and Peters, 1984; Wang and Narisimhan, 1987; Montazar and Wilson, 1984) indicate that high threshold matrix saturations (often close to full saturation) are required before the induction of fracture flow in volcanic tuffs. With *in situ* saturations generally less than 10% in the upper two units of the mesa, which are the only highly fractured tuff units, it seems unlikely that transient pulses would elevate matrix saturations high enough to reach the threshold values. Also, simulation results for flow in a single fracture indicate that extremely high flow rates or ponded conditions are required to sustain fracture flow in the Bandelier Tuff (Soll and Birdsell, 1998). This study also concluded that water flowing from unsaturated crushed tuff into fractured tuff, as is the case of water flowing through the disposal units, is unlikely to induce fracture flow.

The system starts with an initial saturation distribution that results from long-term steady infiltration at 1 mm/yr applied uniformly over the top of the mesa. The simulation is then modified to include the five disposal pits shown in Figure 2.2-1. Transient percolation, with an average of 5.5 mm/yr into the disposal units and an average of 1 mm/yr over the undisturbed mesa top, is applied to the previous steady flow field. The steady runs use a flow field that has equilibrated with the 5.5-mm/yr pit infiltration rate and the 1.0-mm/yr infiltration rate for the undisturbed mesa top.

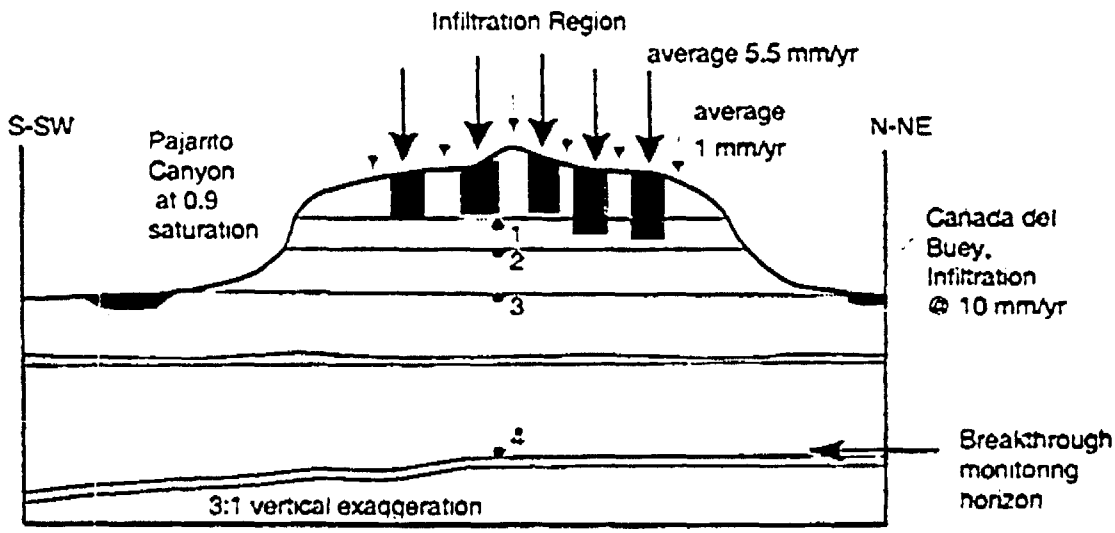

Figure 2.2-1. Two-dimensional cross section used for numeriocalsimulations, modified to indicate five waste disposal pits.

The transient realizations of percolation were determined by the water balance algorithm from the SPUR model (Wight and Skiles, 1987). Precipitation input used a stochastic weather generator with precipitation parameters derived from the Los Alamos gauge at TA-6 (just south of TA-59). The average annual precipitation at TA-6 is approximately 457.2 mm (18 in.) as opposed to the 355.6 mm (14 in.) average annual precipitation at Area G (Bowen, 1990). The pit had a depth of 15.2 m (50 ft.). The upper 0.1 m was topsoil, and the remaining depth was crushed Bandelier Tuff. A plant rooting depth of 0.457 m (18 in.) was assumed. The percolation response was estimated by performing 100 simulations that were 10,000 years long using the stochastic weather generator to provide input. More details on the model and the parameters are available in Springer (1996).

Each realization of pit percolation extends for 10,000 years and has an average percolation rate close to 5.5 mm/yr with most years (approximately 72% to 75%) having no net percolation. Maximum annual percolation rates are near 100 mm/yr. A yearly transient was applied to the upper surfaces of the pits. A similar transient percolation rate, but of decreased magnitude to average 1 mm/yr, was applied to the undisturbed mesa-top infiltration regions. Only four of the one hundred realizations were actually run: Cases 1, 2, 6, and 17. Springer suggested Cases 6 and 17. Case 6 has ten consecutive years of nonzero flow, and Case 17 has the highest number of years with nonzero flow. Some statistics for these four cases are given in Table 2.2-1. The statistics apply for 5,000 years rather than the full 10,000 years because that is the duration over which these transient studies were performed.

Transport parameters are required for the calculations of C-14 migration. Recent studies by Conca (1992) show that the diffusion coefficient decreases with decreasing saturation. The diffusion coefficient was modeled in this fashion and decreases parabolically from 10^{-9} m^2/s at full moisture to 10^{-15} m^2/s at a moisture content of 0.001. The dispersivity is 1 m in the vertical direction and 0.1 m in the horizontal direction.

2.2.2 Transient Flow Results

Simulated saturations at four locations are examined for 3000 years in order to understand the propagation of transient infiltration through the mesa. These locations represent (1) the top of Unit 1v-u, (2) the top of Unit 1v-c, (3) the top of Unit 1g, and (4) the base of the Otowi Member, as shown in Figure 2.2-1. The time dependent saturation plots are given in Figure 2.2-2.

Recall that for the transient calculations, the initial flow field is the result of a steady 1-mm/yr infiltration rate. At each horizon, we can see the saturation front (caused by the higher pit infiltration rate) arrive. There is scatter on the order of 200 years for the arrival time of this front at each horizon due to variations in the applied transient infiltration rate. Case 1 has an average infiltration rate near 10 mm/yr for the first 100 years, which is reflected in the early arrival time of the saturation front at the various depths for this case. Distinct transient responses in saturation are seen for the three more-shallow locations with fluctuations of less than 3%. However, these fluctuations are damped near the base of the Otowi Member, which is directly above our contaminant flux monitoring horizon. Once the initial front has arrived at each level, the mean saturation for each transient simulation is very close to the mean for the steady simulation. The steady simulation has equilibrated with the pit infiltration rate of 5.5 mm/yr; therefore, the arrival of the saturation front is absent in

the steady solution. As shown in Table 2.2-1, Case 17 has the highest average flow (5.81 mm/yr), and Case 2 has the lowest average flow (5.27 mm/yr). This is reflected as slightly higher and lower average saturations, respectively, as seen in Figure 2.2-2.

The percolation estimates used in these simulations are intentionally conservative (high). Actual percolation rates are expected to be lower based on lower precipitation rates and deeper rooting depths. Springer's (1996) base-case pit percolation estimate has evolved as more data have become available. His current estimate of the mean pit percolation rate is 0.99 mm/yr based on a 1-m rooting depth. In a previous study (Birdsell et al., 1995) the effects of applying various single 5-year pulses to various steady flow fields were examined for this same cross section. That study showed that with a lower background flow rate (0.01 mm/yr), damping of an increased flow pulse (10 mm/yr) occurred at higher elevations within the mesa top than for the same pulse applied to a 1-mm/yr steady flow field. This implies that transient pulses should dampen at higher elevations for lower (more realistic) percolation estimates for the site.

Table 2.2-1. Statistics of pit percolation over the first 5,000 years used for transient simulations.

	Case 1	Case 2	Case 6	Case 17
Average pit percolation rate (mm/yr)	5.49	5.27	5.50	5.81
Maximum pit percolation rate (mm/yr)	99.2	88.1	90.8	105.4
Percentage of years with nonzero percolation	26.4%	26.1%	26.4%	27.4%

4

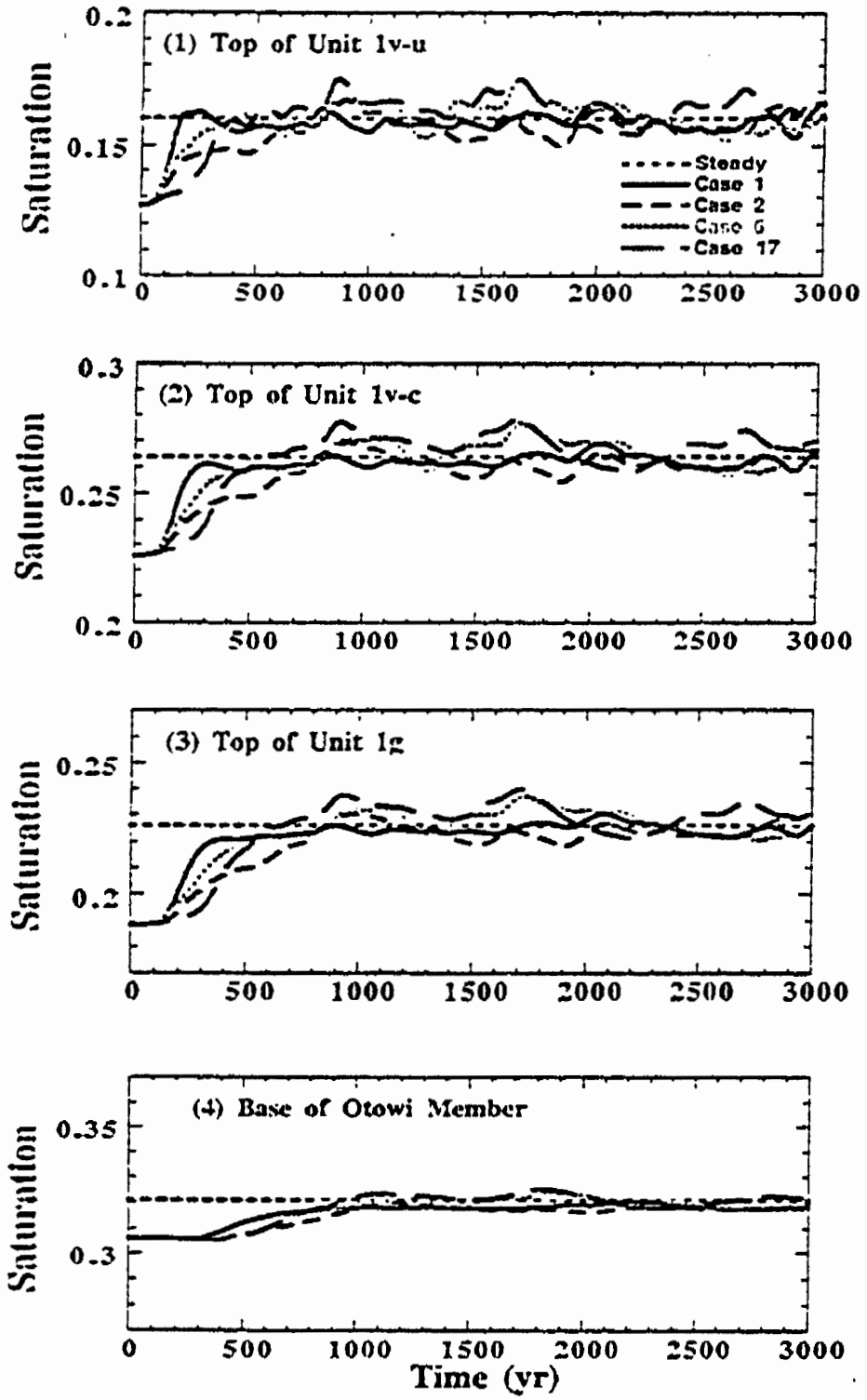

Figure 2.2-2. Variation in saturation with time for the steady and four transient simulations at various depths.

2.2.3 Transient Transport Results

Figure 2.2-3 shows the source term for the flux of liquid-phase C-14 from the waste package to the disposal units. It assumes that the steady flow rate of 4 mm/yr calculated to be passing through the disposal unit (Springer, 1995) is also the percolation rate through the waste package (Vold et al., 1996). We assume this is an adequate representation of the source for these calculations because the water velocity through individual waste packages is unknown and expected to be highly variable. Nearly the entire C-14 inventory (99%) is released over an 80-year period. If the source term were recalculated to account for the higher percolation rate, this mass would be released over a shorter time frame of approximately 60 years because the release is proportional to the ratio of the flow rates. In either case, most of the mass is released from the waste packages over a time frame that is short compared to the simulation time. The flux of C-14 from the disposal units (pits) is dependent on the water velocity through the pits and is calculated self-consistently with respect to the transient infiltration in the simulations. Solubility-limited species such as uranium may have significantly higher fluxes from the waste to the disposal unit when the water flow rate is high, but these species have long travel times (Birdsell et al., 1995) compared to the 10,000-yr uncertainty period.

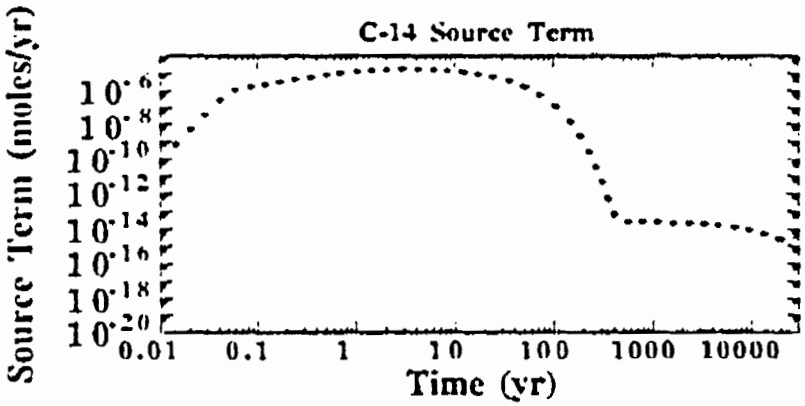

Figure 2.2-3. Source term for the C-14 decay chain based on a pit infiltration rate of 4 mm/yr.

Figure 2.2-4 shows the C-14 cumulative breakthrough curves for the steady-flow case and the four transient-flow cases. These curves represent the total number of moles that have reached the Guaje Pumice (see Figure 2.2-1). There is some scatter in the arrival of mass to the Guaje Pumice, but the curves converge. Table 2.2-2 shows values for time of first arrival at the pumice layer (taken as 1% of the total moles at 5,000 years) and for the total moles to reach the pumice at 5,000 years. The earliest breakthrough occurs for the steady-flow simulation because the flow field is in equilibrium with the higher pit infiltration rate. The first breakthrough for Case 1 precedes the other transient cases because it has a higher average flow rate for the first 100 years. The greatest cumulative flux at 1,000 years is for the steady-flow case because the flow field has already equilibrated with the higher pit percolation rate. The cumulative moles reaching the pumice layer at 5,000 years for the

transient simulations agree within 3% to that calculated for the steady-flow case, with the steady-flow case having the highest value. The steady solution provides a conservative estimate for both the time of first arrival and for the cumulative breakthrough. From a performance standpoint, all of the simulations behave similarly, and the overall agreement is considered to be very good.

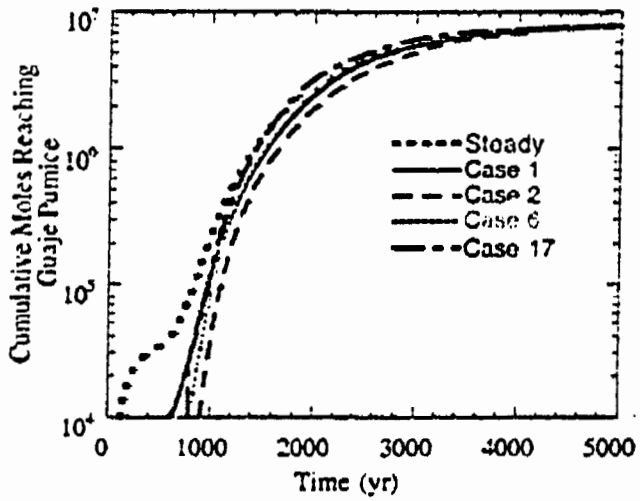

Figure 2.2-4. Cumulative breakthrough curve for C-14 to the Guaje Pumice for four transient infiltration simulations and one steady infiltration simulation.

Table 2.2-2. Comparison of C-14 arrival times and peak concentrations for the steady and four transient flow simulations.

Case	First Arrival (yr)	Cumulative Moles to Pumice at 5,000 yr
Steady	800	8.05e6
Case 1	940	7.81e6
Case 2	1080	7.55e6
Case 6	1000	7.88e6
Case 17	950	7.99e6

2.2.4 Summary of Transient Results

In order to study the effects of transient percolation on flow and transport at Area G, four transient flow simulations are run, and the results are compared to those for a steady-flow simulation that uses the average percolation rate. Before performing these calculations on the two-dimensional cross sections, a set of preliminary one-dimensional calculations were performed to examine whether fractures needed to be explicitly accounted for. These preliminary calculations were performed using the dual permeability model that permits different fluxes in the fractures and matrix. The dual permeability formulation is also appropriate for these scoping calculations related to the effect of transient percolation because it does not force capillary pressure equilibrium between the matrix and fracture material. The results of these dual-permeability, transient-flow scoping calculations show that flow and transport in the upper layers of this system tend to remain in the matrix material. These results are, of course, strongly related to the choice of the fracture characteristics, which are derived from the parallel plate theory of fracture flow. Simulations of steady-state and transient percolation with and without the dual-permeability, formulation all yielded approximately the same travel times.

The investigation of transient percolation flux was extended to the two-dimensional cross section. For these calculations, the matrix, hydrologic properties were used, thereby neglecting rapid transport in fractures. Moisture profiles at various depths are compared. The simulations show that fluctuations in infiltration produce distinct responses in saturation (less than 3%) through Unit 1g that dampen at the base of the Otowi Member. Damping would presumably continue as the water percolates through the deeper units toward the water table.

Transport of C-14 is modeled along with the transient flow in the two-dimensional system. The steady-flow solution provides a conservative estimate for both the time of first arrival and for the cumulative breakthrough of the C-14. From a performance standpoint, all of the simulations behave similarly, and the overall agreement is considered to be very good. The simulations are for a conservative radionuclide and are based on an average percolation rate that is thought to be quite high for this site. Higher sorption coefficients delay the arrival time of the contaminant but yield results having similar spread in arrival time. Lower percolation rates are expected to produce results with even better agreement.

The one- and two-dimensional modeling of transient and steady state percolation with or without the dual permeability formulation support the use of matrix properties and the steady-flow assumption when calculating radionuclide transport at Area G. However, the investigation of the role of fractures was limited in scope to a set of characteristic curves based on the theoretical parallel plate fracture model. We must point out that other than the deep basalt, only the upper two geologic units, Unit 2 and Unit 1v-u, are considered to be significantly fractured. The disposal pits are excavated through Unit 2; therefore, waste can only really travel in fractures through Unit 1v-u until it reaches the basalt. These studies have shown that the matrix material damps transient pulses. Even if transient pulses propagate through the fractures in Unit 1v-u, the tuff units below will most likely attenuate them. Additional support for our conceptual model of very little sustained fracture flow is further supported with the study of flow in a single fracture that is described in the following section.

2.3 FRACTURE FLOW

2.3.1 Single Fracture Modeling

We have performed another study using FEHM to analyze the influence of different characteristics of a fractured system on the movement of fluids in the subsurface. The study focuses on conditions that are relevant to our local system, particularly the influence of fracture coatings and fracture fills on infiltration of water, and on the extent of matrix-fracture communication. Soll and Birdsell (1998) and Soll (1995) describe this work in full, but the results are summarized here as they pertain to the development of the flow model for MDA G.

In an attempt to isolate behaviors, we have chosen a system that is a single vertical fracture centered in an otherwise uniform block of matrix (Figure 2.3-1). There are four parts of the system: the matrix, the fracture, the fracture coating, and the fracture fill. The matrix characteristics represent Bandelier Tuff properties from Mesita Del Buey, Unit 1v-u. The fracture aperture and spacings are average values from local measurements (Krier et al., 1996). In this study, the fracture is given the hydrologic properties of a highly porous and highly permeable sand. This assumption allows us to study a fractured system using a porous media simulator, but the results must be interpreted in context with field observations and measurements.

The system is discretized so that a thin coating layer can be assigned along the walls of the fracture. For simulations that have no coating present, these elements are assigned matrix properties, thus maintaining the 5-mm fracture aperture through all simulations. Fracture fill can be emplaced by replacing the fracture's hydrologic properties with fill properties for some given length of the fracture. When present, fracture coatings and fracture fills are assigned clay parameters. We use clay parameters from the literature because there are no values available for the local clays and caliches.

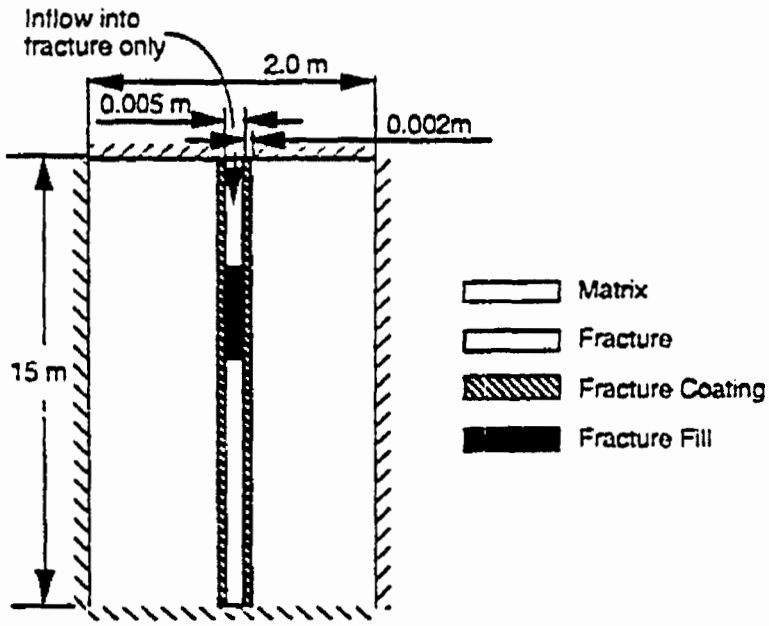

Figure 2.3-1. System configuration for fracture flow study.

Two different inflow conditions are used at the top of the fracture. One inflow condition assumes a constant influx, at a rate of 5 cm/day, which we considered to be representative of an extreme event for a single day. However, this inflow rate was applied for the entire time period of the simulations, often up to 100 days. The other inflow condition used was a ponded condition at the top of the fracture applied for 0.5 days, followed by removal of the source. This was effectively an infinite source of water for 0.5 days with infiltration rates controlled by the fracture-matrix system. Both of these inflow conditions result in an amount of water entering the system in a matter of days that far exceeds the amount of precipitation seen at Los Alamos over a period of years. These extreme conditions allow us to focus on absolute worst cases.

The most dominant observation from the simulations is that in all but the most extreme infiltration events, fractures in the Bandelier Tuff of MDA G do not appear to provide a "fast flow path" for liquids. Even under extremely high infiltration events, fractures with no coatings or fills are not able to carry liquids very far, and the invading saturation front looks very similar to that observed in an unfractured system with point injection.

We found that the effect of a coating along the walls of the fracture is dependent on the relative conductivities of the coating and the matrix. A coating with only 2 orders of magnitude less conductivity than that of the matrix does virtually nothing to prevent liquid in the fracture from being imbibed by the matrix. When there is a larger (4 orders of magnitude) reduction in conductivity at the fracture-matrix interface, water is strongly channeled in the fracture. Any conductivity reduction acts to spread the infiltrating front further down the matrix, allowing water to penetrate deeper

during an infiltration event. However, a discontinuity in the low conductivity coating interrupts the fast flow down the fracture. This suggests that the high capillarity of the Bandelier tuff will rapidly draw water into the matrix near any break in a fracture coating. The simulations also show that fracture flow driven by the ponded boundary condition ceases once the source is removed.

When we consider the role of fills in affecting water infiltration, we find that fractures that are filled at the exposed surface of the fracture are effective barriers to inflow into the fracture. These observations are in agreement with Rosenberg et al. (1993). Fills below the surface are effective barriers to continuous flow down the fracture. With no coating or only minimal conductivity reduction above the fill, water entering the fracture is simply imbibed into the matrix and proceeds down as matrix flow. When a continuous, low-conductivity coating is present, the water does not pass beyond the fill, and simply ponds at the surface. A fracture that ends within a unit of the Tshirege Member or at the interface between two units will behave like a fracture that is filled at that level. The path for the water in the fracture is eliminated, and the water must find an alternate route through the subsurface.

We have also run a simulation with a 1-m "cap" of matrix material placed across the entire fracture-matrix system. This condition represents the current surface cap at MDA G and the conditions at the floor of the waste disposal pits, both of which are made up of crushed (unfractured) tuff. The matrix cap was then held at saturations ranging from 50% to 90%. In none of the simulations did water break into the fracture, although it moved as a steady front through the remaining matrix material. These results are consistent with results obtained by Rosenberg et al. (1993) using a different numerical model.

Although most of these results indicate that fractures do not play a significant role in moving water from the surface to the water table, there are reasonable, possible local conditions that may be sufficient to produce significant flow. There are high influx conditions such as snow melt or large runoff events or ponding of runoff resulting from surface disturbances such as buildings, roads, soil compaction, and removal of vegetation that could cause water to move a significant distance in a fractured system. There is some evidence for such flow at other LANL locations (Turin, 1995). It must also be kept in mind that there is wide variation between the different fractures and that it is possible for one or two fractures to be carrying water although most others do not.

We do not expect fractures to be a fast path for contaminants out of the bottom of the pits because these fractures are covered with crushed tuff. However, if water is able to pond within the pit, it may be possible for that water to exit the pit through fractures on the face of the pit that are not filled or covered. Fractures that are not directly beneath the pits may play an indirect role in the movement of water and contaminants from the pits. Increases in matrix saturation as a result of water moving in the fractures are a potential source of water beneath the pits. As observed in the simulations, water that enters the matrix rapidly redistributes throughout the matrix block toward a uniform saturation. This can act to increase saturation beneath the pit, thus raising the hydraulic conductivity and allowing more rapid movement through the matrix.

2.3.2 Dual-Permeability Fracture Modeling

The fractured system can also be modeled with FEHM using a dual permeability formulation (Zyvoloski et al., 1995). For this formulation, an identical numerical grid is constructed for the matrix and fracture materials so that a one-to-one correspondence exists between a fracture node and the matrix node at that same position. Fluid flow occurs within each continuum, and a transfer term accounts for fluid flow and contaminant transport between the fracture and matrix. Orr has run a number of one-dimensional simulations with this model. Fracture properties are defined for Units 2 and 1v-u based on parallel plate theory. Travel times to the top of basalt for both steady and transient simulations show no significant variation with the addition of the fractures to the model. Orr shows interesting variations in saturation and travel times at different depths within the one-dimensional column for the transient simulations. The reader is referred to Appendix B for more details.

2.4 EVAPORATION

2.4.1 From Mesa Sides and Fractures

Very low net infiltration rates are required to match the field-observed saturation in the two mesa-top units, Units 2 and 1v-u. Evaporation from the top and sides of the mesa and possibly from fractures is a likely player in keeping the mesa dry. Some data (Rogers et al., 1995, Rogers and Gallaher, 1995) suggest that groundwater flow may be upward toward the volcanic surge beds located at the base of Unit 2. This flow could be driven by evaporation occurring in the surge beds. Some simple simulations are used to study these effects.

First we consider evaporation from the mesa sides and from vertical fractures with both 10-m and 5-m fracture spacing. A two-dimensional rectangular grid (25 m wide, 5 m tall) composed of a homogeneous material, either Unit 2 or Unit 1v-u, is used. Figure 2.4-1 shows the problem configuration. Uniform infiltration of 0.1 cm/yr occurs along the upper boundary. This infiltration rate accounts for evaporation from the mesa top, but is higher than the flow rates found previously to best match the *in situ* saturations of Units 2 and 1v-u (0 to 0.001 cm/yr). We compare the resulting vertical saturation profiles for the following cases: infiltration only, infiltration with evaporation occurring along the right boundary (mesa edge), and infiltration with evaporation along the right boundary and from fractures of either 10-m or 5-m spacing. For the infiltration-only case, the right boundary is impermeable. The evaporative boundary is modeled by fixing the saturation at that boundary to a low saturation corresponding to 50% relative humidity. For the fracture runs, the fractures are also held at a low saturation corresponding to 50% relative humidity, which is close to the average annual relative humidity for the area. The corresponding saturation values are 0.032 for Unit 2 and 0.00892 for Unit 1v-u.

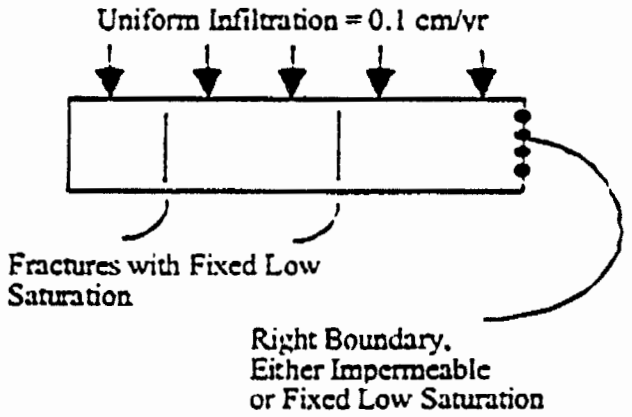

Figure 2.4.1. Problem setup for study of evaporative effects from mesa sides and from fractures.

Figures 2.4-2 and 2.4-3 show the simulated saturation profiles for a horizontal slice through the center of the grid for Units 2 and 1v-u, respectively. For both units, it appears that evaporation affects the saturation profile to a distance of about 7 m from the mesa edge—not much for a mesa that is over 300 m wide. However, assuming that fractures with 5-m spacing act as conduits for air flow, evaporative effects may decrease saturations throughout both units in the mesa top. With fractures spaced 5 m apart, average saturation decreases by ~0.03. From Figure 2.1-2 we see that this order of decrease in saturation corresponds to approximately an order of magnitude decrease in the net steady infiltration rate. Actual fracture spacing in these units is 1.0 to 1.3 m, but only a fraction of these may be open to airflow. Some air flow would be required to remove water vapor from tuff because the relative humidity of the air in a nonflowing fracture would equilibrate with that of the surrounding matrix. It is quite possible that fluctuations in the barometric pressure (Nilson et al., 1991), thermal gradients, and topographic effects (Weeks, 1987) could drive such air flow in a fractured system located on a mesa top.

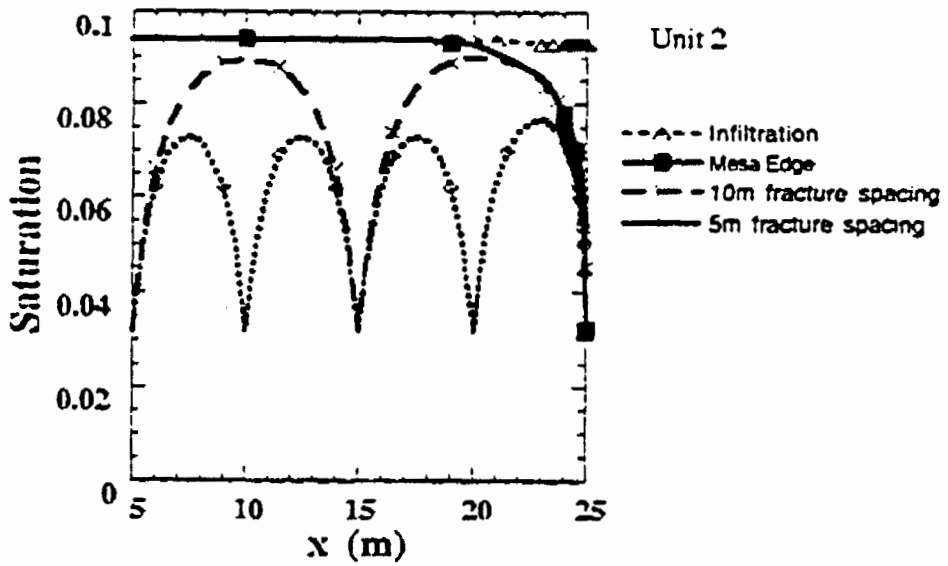

Figure 2.4-2. Resulting saturation profiles for evaporation along a mesa edge (right side) and from fractures with 5-m and 10-m spacing, Unit 2.

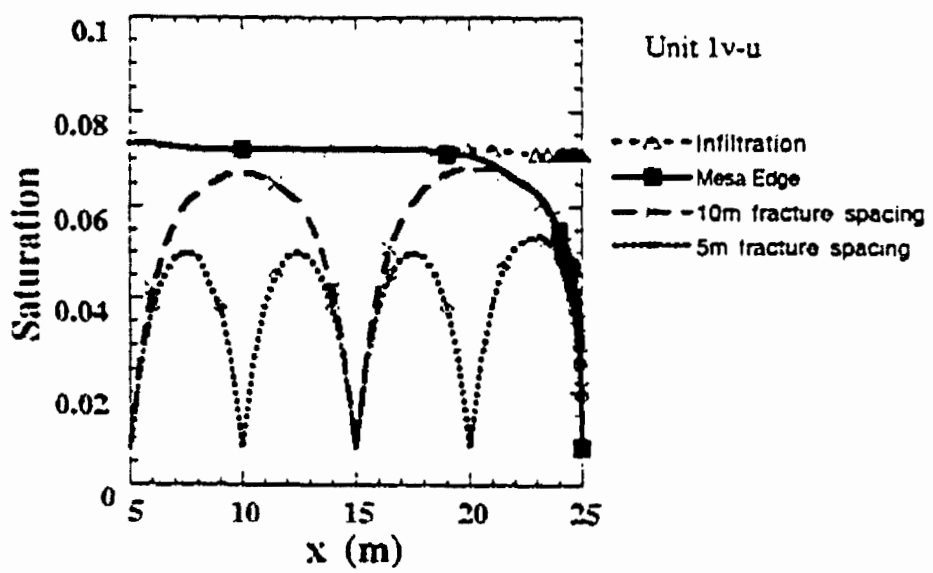

Figure 2.4-3. Resulting saturation profiles for evaporation along a mesa edge (right side) and from fractures with 5-m and 10-m spacing, Unit 1v-u.

We note here that evaporation in these simulations and the one that follows is modeled as an isothermal process with saturations fixed at low values corresponding to a relative humidity of 50%. These results are nearly identical to simulated results, also calculated with FEHM, under nonisothermal conditions that account for vapor pressure lowering and binary diffusion of air and water vapor. For these examples, evaporation results in a simple, capillary-pressure-driven wicking toward the drier, atmospheric boundary. Water vapor contributes less than 1% of the mass in the system for these particular examples that were held at or very close to 20°C, even for the nonisothermal simulations. However, the more complex processes may have a larger effect under more realistic nonisothermal conditions (e.g., geothermal gradients or solar heating of the mesa sides).

2.4.2 From Surge Beds

The next test examines the hypothesis that air flow through the volcanic surge beds located at the base of Unit 2 can cause upward moisture flux from Unit 1v-u. The surge beds, a thin interval of fine, sand-sized material, are attributed to deposition from the basal surge associated with violent eruptions (Krier et al., 1996). There is some evidence that this interval is conductive to higher air flow rates than is the rest of the mesa interior. Two layers, Units 2 and 1v-u, are modeled with their appropriate hydrologic properties and thicknesses. Uniform infiltration at a rate of 0.1 cm/yr is applied along the upper boundary. Again, we compare the results with infiltration alone to results that include evaporation along the surge bed. The surge bed is modeled simply as a set of low saturation nodes, corresponding again to a relative humidity of 50% along the interface of the two layers. Figures 2.4-4 and 2.4-5 show the steady-state saturation and capillary pressure profiles for this case. Saturation values throughout both units are significantly lowered by the fixed low saturation at the interface. In Figure 2.4-5, the calculated values are compared to suction data reported by Rogers et al. (1995) for borehole G-5, which is located at MDA G. The data are translated spatially to force the surge bed to align with that from the simulation. We see that the calculated capillary pressure lies between the two data sets reported by Rogers.

These simulations show that evaporation along fractures and surge beds can contribute to significant drying of the mesa top units, possibly causing the very low saturations seen in these units. We feel that the mesa may act as a natural dry barrier that substantially blocks deeper penetration of liquid flow as described in the site conceptual model (Rogers et al., 1997). This theory needs to be substantiated with more data and modeling studies.

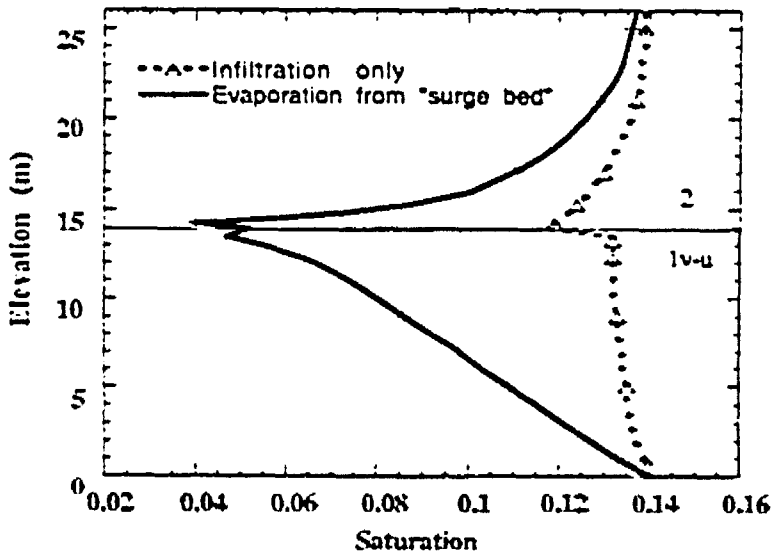

Figure 2.4-4. Resulting saturation profile for evaporation along the surge beds at the Unit 2/1v-u interface compared to that for infiltration alone.

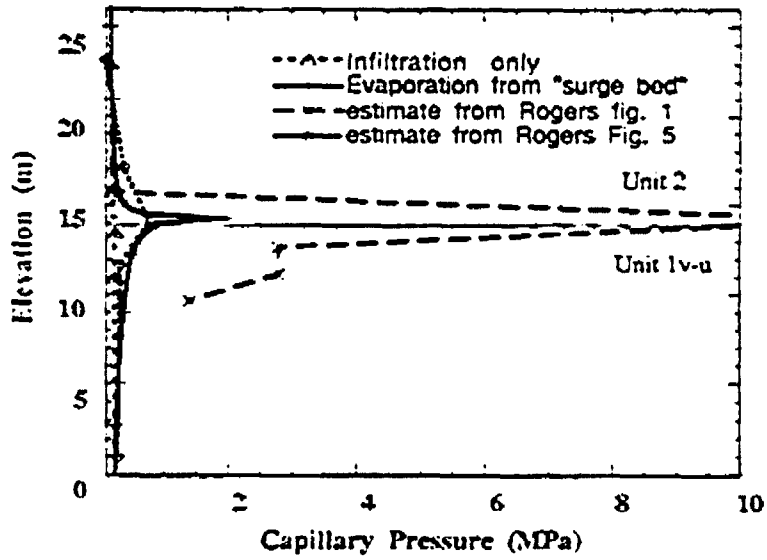

Figure 2.4-5. Resulting capillary pressure profile for evaporation along the surge beds at the Unit 2/1v-u interface compared with infiltration alone and with data from Rogers et al. (1995) for Borehole G-5.

3 THREE-DIMENSIONAL VADOSE-ZONE MODEL

3.1 VADOSE-ZONE MODEL DEFINITION

The vadose-zone model is based on a three-dimensional representation of the site that describes the complex mesa-top geology. Infiltration is assumed to be steady, although the mesa top and two canyons that border Area G receive different infiltration rates. Results for a base-case flow field are compared to those for some variations on the flow field as part of an uncertainty analysis. The model incorporates the position and inventories of the thirty-four disposal pits and four shaft fields already located at Area G along with those of future pits and shafts. Two pathways are considered: downward migration through the vadose zone to the aquifer, and lateral migration to the mesa sides, deposition into the nearby canyon, and subsequent migration through the vadose zone to the aquifer. Time and spatially dependent results for nuclide flux from the vadose zone feed the saturated-zone model. The simulations are run for 10,000 years to cover the 1,000-year compliance period and the 10,000-year uncertainty analysis.

The assumptions used for the vadose-zone model rely heavily on the studies of specific flow processes presented in Section 2.0. The equivalent continuum parameters chosen to represent the basalts in Section 2.1 are used. These properties produce fast travel times through the basalt in order to compensate for the lack of hydrologic information about the unit. All flow is forced vertically through the basalt, thereby eliminating lateral diversion at the basalt-pumice interface.

In Section 2.2, we studied the effects of transient percolation on vadose-zone transport at Area G and found that at the flow rate considered, transient pulses are damped with depth and cumulative contaminant flux results at depth are similar under transient and steady flow fields. Steady infiltration is also assumed in PA calculations used for other sites (Barnard and Dockery, 1991, and Wood et al., 1994). By using a high, steady infiltration rate and other conservative assumptions concerning flow at the site, the subsequent transport calculations are expected to yield conservative results, assuming that fracture flow is not induced.

The fracture flow studies presented in Section 2.3 indicate that transport through fractures has a minimal effect on contaminant flux at depth. Therefore, fractures are not included in the three-dimensional vadose-zone model. In Section 2.4 we found that evaporative effects can reasonably account for the low moisture contents observed in the mesa-top units at the site and justify a small infiltration value.

Previous modeling studies for Area G assumed that the pit percolation rate was likely to be higher than the percolation rate for the undisturbed mesa top (Birdsell et al., 1995 and Section 2.2 of this report). The pit density at Area G is high enough that the area can almost be considered "one big pit" in terms of infiltration (see Figure 3.1-2). Recent studies by Newman (1996), Vold (1996), and Springer (1996) show enough variability and overlap in estimates of pit and undisturbed mesa top percolation rates that a single value for the pit and mesa top rates is justifiable and is therefore used in this study. However, we do consider three different rates as described in Section 3.1.3.

3.1.1 Stratigraphy

The stratigraphy was constructed from various sources. The topography and the bases of the Otowi Member (Qbo) and the Tshirege Member (Qbt or Unit 1g) were obtained at 15.24 m (50 ft) spacings (northing and easting) from the LANL site-wide geologic model (Vaniman, et al., 1996). Well-log picks were used to define Units 2, 1v-c, the Cerro Toledo, and the Guaje Pumice. Data were used for wells 54-1102, 54-1105, 54-1106, 54-1107, 54-1108, G-2, 54-1110/G-3, 54-1111/G-4, 54-1112, 54-1114, 54-1115, 54-1116, 54-1117, 54-1120, 54-1121, 54-1123, 54-1124, 54-1125, 54-1126, 54-1128, 54-1001, 54-1002, 54-1003, 54-1004, 54-1005, 54-1006, 54-1008, 54-1009, 54-1015, and 54-1016 (Vaniman, et al., 1996). Some of these holes are inclined, and the northing, easting and depth values required corrections. Surface observations for the contact between Units 2 and 1v-u obtained from Broxton (personal communication, 1996) were used to further constrain this contact. A data point from Well TH-5 (Purtymun, 1995) was also used to constrain the Guaje Pumice layer. The overall number of data points that were available in the vicinity of MDA G for each of the surfaces was 76 for Unit 2, 30 for Unit 1v-c, 25 for Unit 1g, 14 for the Cerro Toledo, and 4 for the Guaje Pumice.

The data set was interpolated at 45.72-m (150-ft) intervals with the Stratigraphic Geocellular Modeling (SGM) Software (Version 3.10, Copyright 1994, Stratamodel, Inc.). The topographic surface truncates any surface that it crosses. The Guaje Pumice was calculated by adding the layer thickness to the Qbo unit rather than by using its elevation because so few data are available to constrain this unit. Likewise, the Cerro Toledo Unit was calculated as a thickness below Unit 1g. The surface for the base of 1v-u was poorly defined by the well-log elevation data resulting in unrealistic undulations that caused overlapping of layers above and below. This surface was ultimately defined as a surface parallel to Unit 1v-c with a thickness of 7.62 m (25 ft) as suggested by Krier who said that this interface is difficult to identify in core samples. Some other minor modifications were made to the surfaces to avoid unphysical crossing of surfaces. The Puye Conglomerate is defined as a 30.48 m (100 ft) thick flat unit within the vadose zone at the base of the model. This layer is probably thicker than 30.48 m (100 ft) in the vadose zone (Krier, 1996), but again too few data are available to justify a more sophisticated representation. The Cerros del Rio Basalts occupy the region between the Guaje Pumice and the Puye Conglomerate. The water table is defined as a flat surface at an elevation of 1767.8 m (5800 ft) although it actually dips downward at the eastern end of the mesa.

Figure 3.1-1 shows the resulting three-dimensional stratigraphic, vadose-zone model. The Bandelier Tuff units generally dip and thin toward the east. However, the Guaje Pumice dips toward the west.

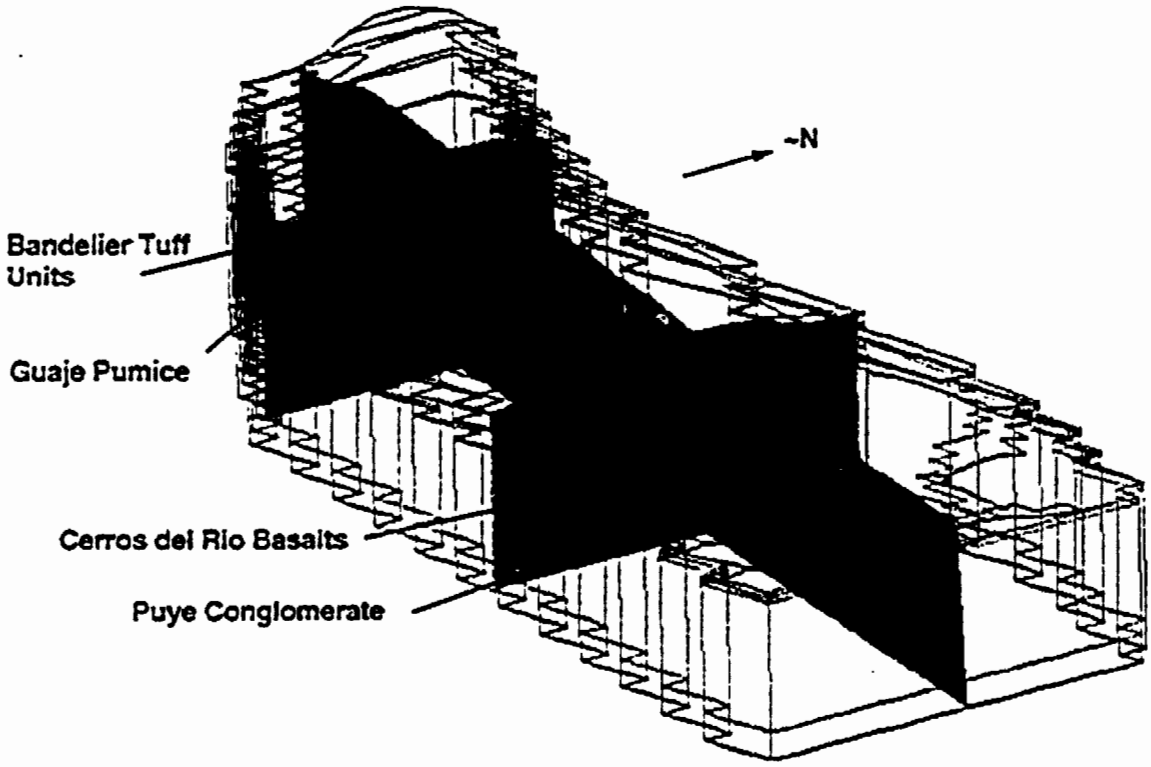

Figure 3.1-1. Three-dimensional stratigraphy for the vadose-zone model of Area G.

3.1.2 Grid

The surfaces generated with SGM were used to construct the three-dimensional grid. The grid is generated with the Geomesh/X3D software (Gable, et al. 1995). An initial grid based on the stratigraphy is constructed with 45.72-m (150-ft) grid spacing. This grid is then refined to include the 38 waste disposal pits and to better define the mesa sides. The final grid is made of 41,542 nodes and 254,614 tetrahedral elements. The surface definition for the pits was obtained from the Facility for Information Management, Analysis, and Display (FIMAD) at LANL. Each pit is assumed to be 10.7 m (35 ft) deep. Pit regions are defined by a set of nodes that outline several adjacent pits both at the surface and at a 13.7-m (45-ft) depth. A set of internal nodes is added down the centerline of each pit at a depth of 7.62 m (25 ft). The volume associated with these nodes approximates true pit volumes. Because the volume of finite element nodes extends halfway to the next node, the resulting pit depth is the desired 10.7 m (35 ft). These internal pit nodes are assigned hydrologic properties for crushed tuff and are the nodes that release waste during the transport calculations. Figure 3.1-2 shows the outline of the waste disposal pits, the internal pit nodes, as well as the outline of the mesa.

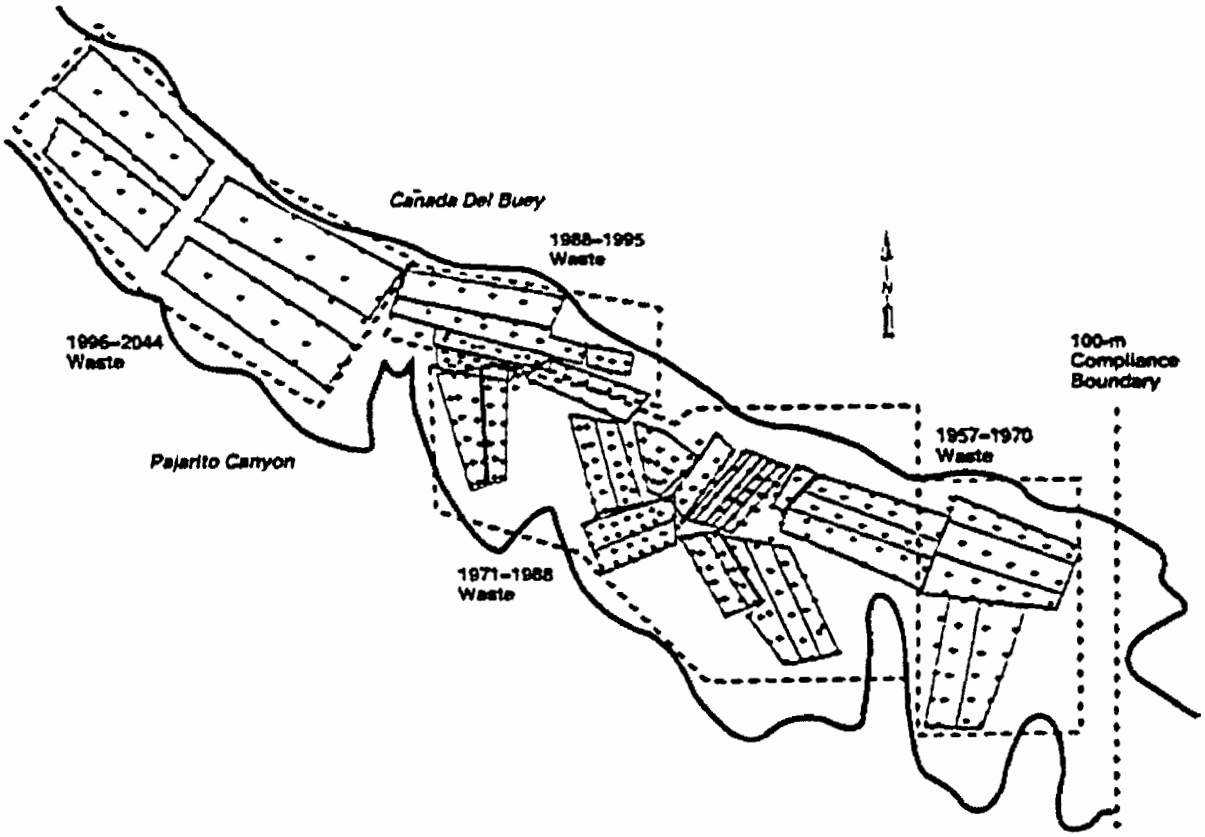

Figure 3.1-2. Pit boundaries, internal pit nodes, and mesa edge for the three-dimensional vadose-zone calculations.

3.1.3 Boundary Conditions

The mesa/canyon setting in which MDA G exists leads to a complicated set of boundary conditions. A very low net percolation rate (1 to10 mm/yr) is thought to occur within the mesa. Pajarito Canyon is quite wet with an estimated percolation rate of 10 to 100 mm/yr, but Cañada del Buey is dry with a percolation rate similar to the mesa top. The mesa sides are steep enough that they should represent an evaporative region (water sink) rather than a source region. For these reasons, the top surface nodes of the grid are categorized by position so that various boundary conditions can be applied to the mesa top, to Pajarito Canyon, to Cañada del Buey, and to the mesa sides. Figure 3.1-3 shows a boundary condition map for the topographic surface. The center portion of the grid receives the mesa-top percolation rate, and the outer portions receive canyon percolation rates. The outline of

the mesa is clearly defined in this figure by the evaporative boundary nodes. The evaporative nodes are held at a fixed saturation of 0.03, which is equivalent to an ambient relative humidity near 50%. Some nodes are not categorized and are assigned no-flow boundary conditions. These nodes are adjacent to the evaporative nodes and act as buffers between the different boundary regions.

Five different flow fields are considered in order to study the sensitivity of the calculated saturation fields and the transport results to background flow rates. Three mesa-top flow rates are used (1 mm/yr, 5 mm/yr, and 10 mm/yr), two flow rates for Cañada del Buey are considered (1 mm/yr and 5 mm/yr), and three flow rates for Pajarito Canyon are used (20 mm/yr, 50 mm/yr, and 100 mm/yr). Table 3.1-1 summarizes the five cases. The base case, 5_1_50, is thought to be conservative for the site. Using chloride flux estimates, Newman (1996) reports near-surface, mesa-top flux rates of 3 to 6 mm/yr, midmesa flux rates ranging from 0.03 to 1.5 mm/yr, and submesa flux rates near 5 mm/yr. Vold (1996) gets similar results using moisture profile analysis. Springer (1996) estimates a mean pit percolation rate of 0.99 mm/yr using a water balance algorithm. Simulated moisture profiles (Figure 2.1-2) show that the range 1 mm/yr to 10 mm/yr conservatively fits the available moisture data. Rogers et al. (1996) estimate recharge at 4.4 mm/yr in Cañada del Buey and 20 to 100 mm/yr in Mortandad Canyon, which is considered to be hydrologically similar to Pajarito Canyon.

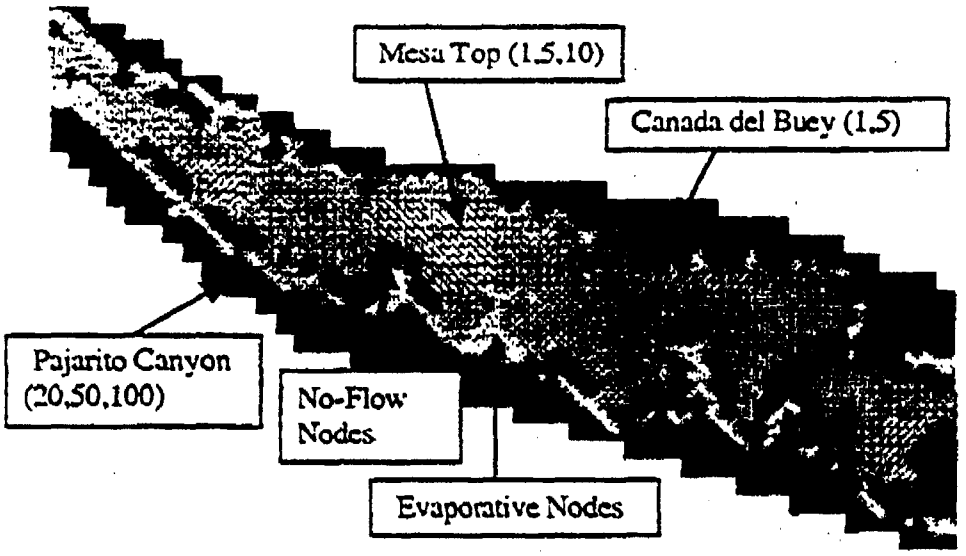

Figure 3.1-3. Boundary condition map of the topographic surface for the vadose-zone flow and transport calculations. Parenthesized values indicate flow rates in mm/yr.

Table 3.1-1. Infiltration rates (mm/yr) used as upper boundary conditions.			
	Mesa Top	Cañada del Buey	Pajarito Canyon
1_1_20 (Lowest Flow Case)	1	1	20
5_1_20	5	1	20
5_1_50 (Base Case)	5	1	50
10_1_20	10	1	20
10_5_100 (Highest Flow Case)	10	5	100

No-flow boundary conditions are applied to the sides of the grid. The bottom boundary represents the water table with a fixed saturation of 0.99. Both water and radionuclides can exit this boundary. Time dependent radionuclide flux through the bottom of the vadose-zone grid is recorded at each time step to be used as input to the saturated-zone model. In order to supply an adequate spatial flux distribution, the bottom boundary is divided into 28 regions for which fluxes of radionuclides are reported as shown in Figure 3.1-4.

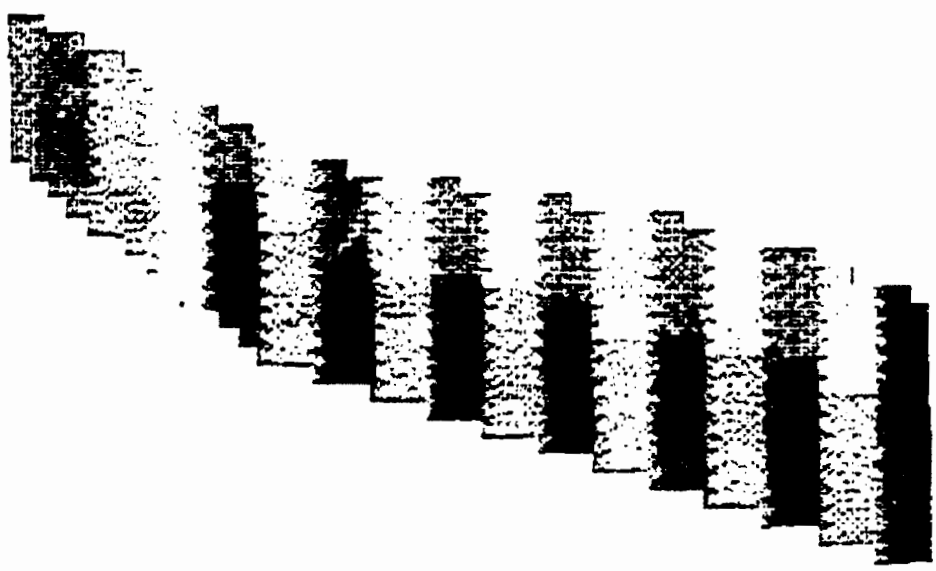

Figure 3.1-4. Bottom boundary divided into 28 regions for which temporally and spatially dependent flux from the vadose-zone calculation is reported.

3.1.4 Hydrologic Properties

The hydrologic properties for the units are given in Table 2.1-1. As described in Section 2.1.2, basalt properties are chosen that produce rapid vertical transport through the fractures of this unit. The basalts are treated as an equivalent continuum medium (Klavetter and Peters, 1986) made up of both fractures and matrix material. The fractures are assigned a high permeability and porosity that promote vertical flow from the pumice into the basalts, thus minimizing lateral flow within the pumice. The porosity of the basalt continuum is set equal to 10^{-4}, the estimated volume fraction of fractures, causing most flow to occur in the fractures and resulting in extremely rapid groundwater travel times of between 1 and 5 years through the basalts.

Although hydrologic properties for the Puye Conglomerate are also unknown, we expect that our intuition for flow through this unit is better. The layer is modeled as coarse sand (Carsel and Parrish, 1988) with the porosity reduced by 60% (from 0.43 to 0.25) as described in Section 2.1.2. This should lead to conservative (faster than expected) travel times through the Puye Conglomerate.

3.1.5 Transport Properties

Recent studies by Conca (1992) show that the diffusion coefficient decreases with decreasing saturation. The diffusion coefficient was modeled in this fashion and decreases parabolically from 10^{-9} m^2/s at saturation to 10^{-15} m^2/s at a moisture content of 0.001. The dispersivity is 1 m in the vertical direction and 0.1 m in the horizontal direction.

Table 3.1-2 shows the distribution coefficients (Kd) for each nuclide in the simulations. The column "Intact Tuff" applies for the vadose-zone Bandelier Tuff units. The values for Am, Np, Pu, Tc-99, and U were measured at a pH of 9.8 on Bandelier Tuff samples, using a sodium-bicarbonate-carbonate-rich synthetic solution representing pore water extracted from the tuff (Longmire et al., 1996). The remaining values are based largely on sorption measurements for Yucca Mountain tuffs (Krier et al. 1996). These distribution coefficient values apply from Unit 2 down through the Guaje Pumice Bed. No distribution coefficient is applied in the basalt layer in order to be consistent with the assumption of rapid transport through that unit.

Table 3.1-2. Median distribution coefficients (Kd (ml/g) for nuclides on intact and crushed, unsaturated Bandelier Tuff and on saturated samples.

	Intact Tuff	Crushed Tuff	Aquifer
Nonsorbing Nuclides			
^{14}C, ^{129}I, ^{99}Tc	0	0	0
Weakly Sorbing Nuclides			
^{237}Np	2.25	7.5	0.151
^{233}U, ^{234}U, ^{235}U, ^{236}U, ^{238}U	2.43	2.61	4.85
^{93}Mo	4	4	4
^{238}Pu, ^{239}Pu, ^{240}Pu, ^{241}Pu, ^{242}Pu	4.13	711	13.95
Strongly Sorbing Nuclides			
^{40}K	15	15	15
^{210}Pb	25	25	25
^{32}Si	35	35	35
^{244}Cm, ^{152}Eu, ^{154}Eu, ^{148}Gd, ^{231}Pa, ^{147}Sm, ^{151}Sm	50	50	50
^{113}Cd-m	80	80	80
^{108}Ag-m	90	90	90
^{93}Nb-m, ^{94}Nb	100	100	100
^{90}Sr	116	116	116
^{227}Ac, ^{249}Cf, ^{252}Cf	130	130	130
^{226}Ra, ^{228}Ra	200	200	200
^{137}Cs	428	428	428
^{182}Hf, ^{229}Th, ^{230}Th, ^{232}Th, ^{44}Ti	500	500	500
^{133}Ba	946	946	946
^{241}Am, ^{243}Am	2359	2050	141

Different values for the distribution coefficients of Am, Np, Pu, Tc-99, and U are applied in the waste disposal pits as shown in the column "Crushed Tuff" in Table 3.1-2. These values were measured on four samples of Bandelier Tuff Unit 2 from a depth interval of 3.3 to 3.7 m (10.8 to 12 ft) and are representative of the crushed tuff that is used to fill the disposal units (Longmire et al., 1996). The Kd values for the remaining radionuclides are assumed to be the same as for intact tuff.

Kd values that are representative values for the saturated zone have also been measured for Am, Np, Pu, Tc-99, and U. These are shown in the "Aquifer" column of Table 3.1-2. These values were measured on Bandelier Tuff samples at a pH of 7.3 using Water Canyon Gallery groundwater (Longmire et al., 1996), which is expected to be closer to the pH of the saturated-zone waters. These values are applied to the saturated zone and also to the deep vadose zone for the Puye Conglomerate, which we presume has pore water more similar to the saturated zone than to the shallow vadose zone. Again, for the remaining radionuclides, distribution coefficients measured on Yucca Mountain tuffs are used.

3.1.6 Source Term

The source-term models to calculate time dependent total nuclide release rate, Φ (moles/yr), from each disposal unit (Vold et al., 1996; Vold and Shuman, 1997a) are incorporated directly into FEHM for the three-dimensional simulations. Two source-term models are included: rapid release and solubility limited. The rapid-release model takes the form $\Phi = Q\lambda^2 te^{-\lambda t}$, where Q is the total inventory (moles) of the nuclide in the disposal unit, and λ is the release constant ($\lambda = q/\theta h$) where q is the Darcy flux through the waste package, θ is the average moisture content of the disposal unit (taken to be 0.08), and h is the representative height of a waste package (taken to be 1 m). The rapid-release source term is highly dependent on the Darcy flux through the waste package (q) as shown in Figure 3.1-3. For the 10-mm/yr flux, most of the source is released over a 60-year period, but for the 1-mm/yr flux, a similar quantity is released over about 360 years. The solubility-limited model takes the form $\Phi = f_{ij}VqC_{sl}/h$, where V is the total initial nuclide waste volume in the disposal unit, and C_{sl} is the nuclide solubility limit. The fraction f_{ij} is a correction factor for the solubility limit contributions from multiple nuclides, i, of the same element and from multiple waste forms, j. This was determined to be a significant correction factor only for uranium (Vold and Shuman, 1996). The maximum pore water concentration of each nuclide is compared to its solubility limit to determine the appropriate source release model for each nuclide in each disposal unit. The Darcy flux (q) is set equal to the fixed mesa-top infiltration rate (1, 5, or 10 mm/yr) for the flow field of interest. Source-term information describing the total inventory (Q), source-release model, initial nuclide waste volume (V), and solubility limit (C_{sl}) were obtained from Vold and Shuman (1996), which in turn was derived from the complete inventory analysis (Shuman, 1997a).

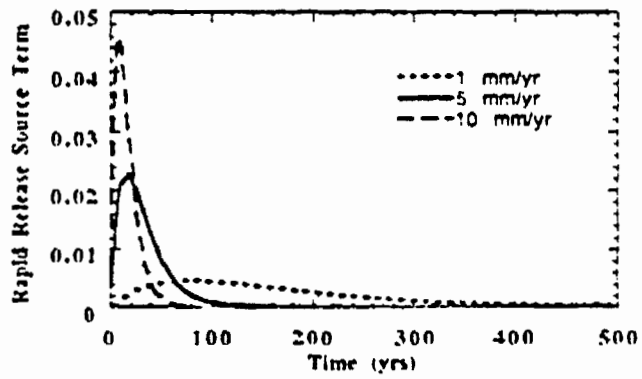

Figure 3.1-5. Velocity-dependent portion of the rapid-release source term ($\lambda^2 t e^{-\lambda t}$).

The source-term information described above was supplied for each of the four disposal unit classifications and are described in Table 3.1-3. Shaft fields were added as surface nodes near their true location. The oldest shafts are 2 nodes located west of pits 2 and 4, 71 to 88 shafts are 4 nodes located west of pit 16, historical shafts are 3 nodes located west of pit 22, and future shafts are 2 nodes located west of the two easternmost future pits.

The inventory data (Shuman, 1997a) for the Oldest and Future wastes are extrapolated or projected values. For each nuclide in these inventory classes, a total inventory and waste volume is given for all of the pits combined and also for the shafts. In this case, the pit inventory is distributed between all of the pit nodes for the waste class (Oldest or Future), and solubility-limited wastes are then

Table 3.1-3. Disposal unit classification and location.

Disposal Unit Classifications	Referred to in Text by	Locations
Extrapolated 1957 to 1970	Oldest	Pits 1 through 6 and in shafts located to the west of Pits 2 and 4
Recorded 1971 to 1988	71 to 88	Pits 7 through 36, except for pits 30 and 31, and in shafts located to the west of Pit 16
Recorded 1988 to 1995	Historic	Pits 30, 31, and 36 through 39 and in shafts located to the west of Pits 22
Projected 1996 to 2044	Future	Four large pits and in shafts to the west of Pits 37 and 38

considered to be solubility limited in all of the pits. Inventory and waste volume are known in greater detail for the 71 to SS and for the historic wastes. For each nuclide in these inventory classes, a total inventory and waste volume is given for each individual pit and for the shafts. The individual pit inventory is distributed between the pit nodes for the appropriate waste disposal pit. Wastes may be solubility limited in some pits or shaft fields and rapid release in others depending on the inventory and waste volume in the particular pit or shaft field.

3.2 VADOSE-ZONE FLOW RESULTS

The base-case flow model uses a 5-mm/yr percolation rate for the mesa top, which includes the undisturbed mesa top as well as the pit areas. Percolation for the adjacent canyons is fixed at 1 mm/yr for Cañada del Buey and 50 mm/yr for Pajarito Canyon. These flow rates are varied in order to quantify the effects of uncertainty in flow rate on dose assessment results. Figure 3.2-1 shows the saturation field looking down on the mesa for the base-case flow field. The outline of the mesa top is evident from the low saturation (dark blue) boundary conditions applied along the mesa edge. A higher saturation (green) is also evident in Pajarito Canyon where the infiltration rate is the highest. This figure shows how well the grid captures the topography of the site and also the application of the boundary conditions.

Saturation profiles as a function of depth at three locations are developed for the various infiltration boundary conditions shown in Table 3.1-1. The three locations are near the eastern end of the proposed future pits, at the eastern end of the historic pits beneath Pit 39, and at the eastern end of Area G just west of Pit 1. The purpose of looking at saturation as a function of depth at these locations is to determine whether modeling the three-dimensional geometry of the topography and of the gently dipping beds coupled with the combination of canyon and mesa infiltration rates can predict the *in situ* saturation measured in the Cerro Toledo and Otowi Member. The relatively high saturations in these units proved difficult to match with the two-dimensional simulations presented in Section 2.1.

Figure 3.2-2 shows saturation profiles at three different mesa infiltration rates but the same canyon infiltration rates (1_1_20, 5_1_20, and 10_1_20) for the location near Pit 1. This figure indicates results similar to those shown in Figure 2.1-2. An increase in the mesa-top infiltration rate leads to increased saturations throughout the depth of the vadose zone. An increase in mesa infiltration from 1 mm/yr to 10 mm/yr results in an approximate increase in saturation on the order of 0.03 to 0.1. Figure 3.2-3 shows saturation profiles at the three locations of interest for the base-case flow rate (5_1_50). The three saturation profiles differ from one another, on the order of 0.02 to 0.05 in saturation, for the same flow field, which is about half the variation seen for the change in flow rate from 1 mm/yr to 10 mm/yr at the location near Pit 1. These results show that *in situ* saturation is not only controlled by the infiltration rate but that the local topographic and stratigraphic configuration are also controlling factors. This suggests that calculated saturation profiles at various locations might better be compared to saturation measurements made at like locations (i.e., individual borehole measurements) than to ensemble average saturation values.

We also examined the effect of canyon flow rates on the saturation profiles at the three locations. A change in infiltration from 1 mm/yr to 5 mm/yr in Cañada del Buey shows no effect on submesa saturations even in the units that lie beneath the canyon floor. However, a variation in infiltration in Pajarito Canyon does affect saturations slightly, for the units from the Otowi Member down to the water table, at the location near the future pits. For example, saturations at this location calculated for the Otowi Member increase by about 0.02 with an increase in the Pajarito Canyon infiltration rate from 20 mm/yr to 100 mm/yr. This increase at the other two locations is almost indistinguishable. There are some geological differences at the location near the historic pits that may explain why the saturation at depth responds more strongly to the boundary condition on Pajarito Canyon than at the other two locations. The mesa narrows, the canyon floor is quite steep, and the canyon cuts the strata differently at the western end of Area G. All of these factors may contribute to a more lateral distribution of canyon flows beneath the mesa top. The location near the future pit is also the closest to Pajarito Canyon of the three sites, and proximity to the canyon may also be a factor.

In general, the calculations indicate that variations in mesa-top flow rate and in monitoring location more strongly affect saturation profiles beneath the mesa than do canyon flow rates. This agrees with a previous two-dimensional modeling study (Birdsell et al., 1995) for the site that considered the effects of canyon flow on submesa saturation profiles. However, the results of this current study and the two-dimensional study do not include a component of lateral flow at the pumice/basalt interface. The inclusion of lateral diversion of flow within the pumice bed not only leads to increased saturation in the Otowi Member, as discussed in Section 2.1, but also leads to calculated submesa saturation profiles that do depend on canyon flow rates. Recent stable isotope studies (Newman, 1996) indicate that canyon waters may flow laterally beneath the mesa. A better understanding of the mechanisms and hydrologic properties that control flow in the deep vadose zone will help to clarify issues related to the interaction of the canyon and mesa flow fields.

3.3 VADOSE-ZONE TRANSPORT RESULTS

Vadose-zone transport calculations were run for C-14, I-129, Np-237, Tc-99, and U-238 using the base-case, steady flow field (5 mm/yr for the mesa top, 1 mm/yr in Cañada del Buey, and 50 mm/yr in Pajarito Canyon). These nuclides were chosen because of their low distribution coefficients, ranging from zero to 2.43 in most of the vadose zone, as shown in Tables 3.1-2 through 3.1-2. Downward flux to the water table and lateral flux to the mesa sides were examined. Interestingly, only C-14, I-129, and Tc-99, the nonsorbing nuclides (Kd = 0), show any breakthrough to either the water table or to the mesa side over the 10,000-year time frame considered. This result enables us to eliminate the remaining nuclides (except for Co-60 and H-3) from consideration in the dose assessment because their distribution coefficients are larger than those of either Np-237 or U-238, which did not break through to either the water table or to the mesa sides. This screening technique includes the consideration of all daughter products in the radionuclide decay chains. Calculations of Np-237 and U-238 transport using the maximum flow field (10 mm/yr for the mesa top, 5 mm/yr in Cañada del Buey, and 100 mm/yr in Pajarito Canyon) also showed no breakthrough, thus showing that the screening technique applies at the higher flow rates considered in this study. Co-60 and H-3 are eliminated from the analysis because of their short half-lives of 5.26 years and 12.3 years, respectively.

26

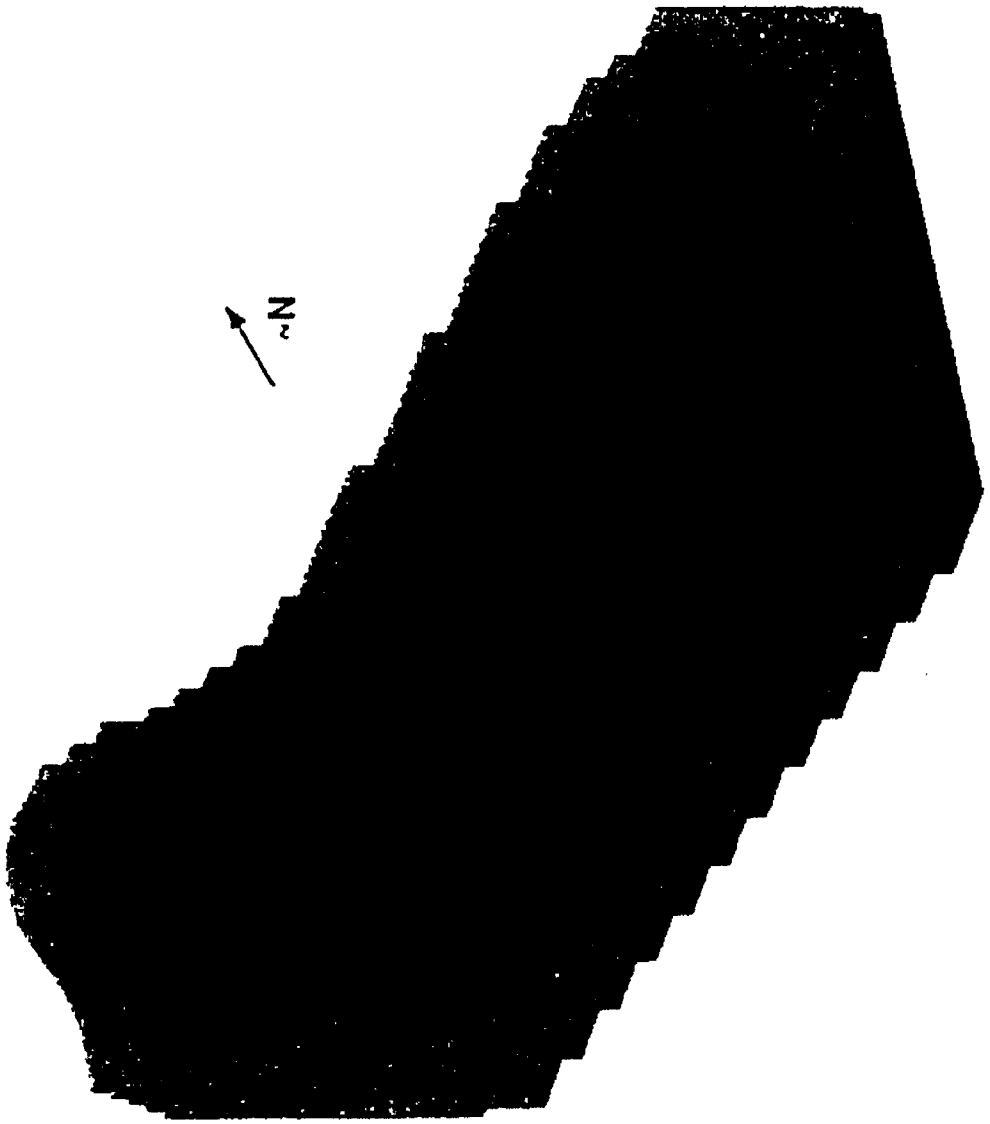

Figure 3.2-1. Steady-state vadose-zone saturation field (top view) for the base-case flow field (dark blue—saturation is ~0.03, light blue—saturation is ~0.2, green—saturation is ~0.5).

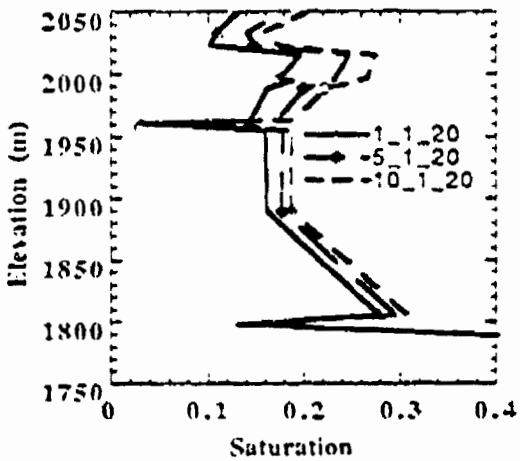

Figure 3.2-2. Saturation profiles near Pit 1 for three mesa-top infiltration rates.

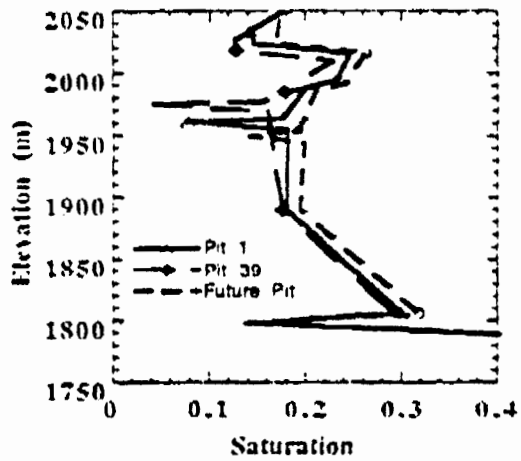

Figure 3.2-3. Saturation profiles for the base-case flow rate (5_1_50) at the three locations of interest.

Figures 3.3-1 show the simulated I-129 plumes for the four source regions (described in Table 3.1-3) after 1,000 years. Although the infiltration rate at each source region is the same (5 mm/yr), the plumes are quite different because of both inventory variations and differences in the thickness of the stratigraphic units. The inventory distribution in the disposal units is heterogeneous, leading to large variations in contaminant release rates from the disposal units to the unsaturated zone. For example, the 71 to SS inventory [Fig. 3.3.1(b)] dominates the total site release of I-129 to the aquifer at 1,000 years. Also, the historic shafts, located near the southern edge of the mesa (left side of Fig. 3.3.1(c)), concentrate nearly 80% of the I-129 historic inventory into a small area, thus producing the predominant plume shown at the south side of the mesa. The historic pits to the north and west produce the less concentrated plumes. The location of the basalt unit and the effect of the vertical, fracture-dominated flow through this unit (see Section 2.1) on plume migration is readily visible in these figures. We see that once solutes reach the basalt, they migrate quickly through the units. In the future waste scenario (Fig. 3.3.1(d)), only the plume's leading edge reaches the basalt after 1,000 years because the tuff units are much thicker beneath this proposed expansion area.

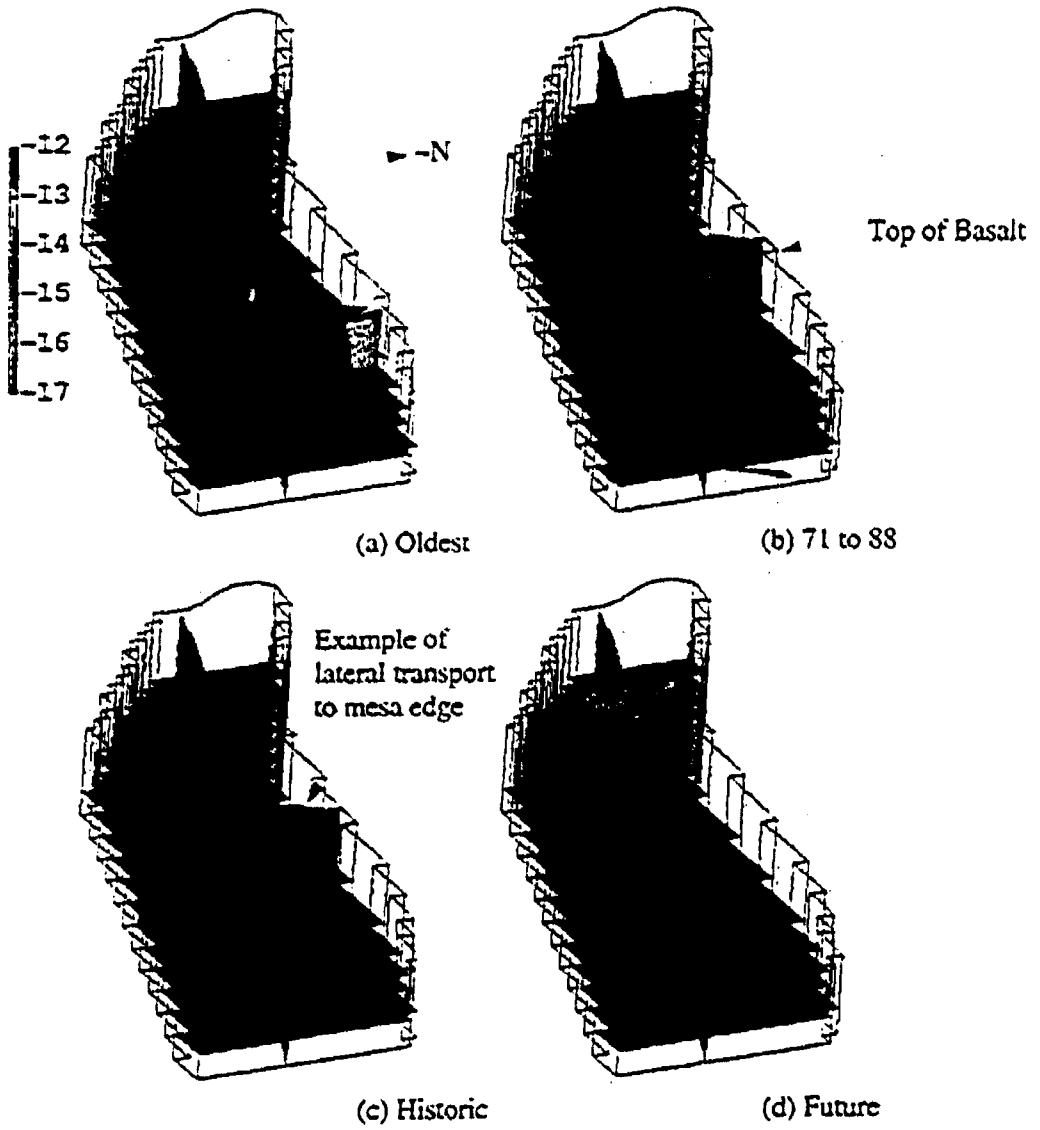

Figure 3.3-1. I-129 plumes (log scale concentration, moles/liter) in the vadose zone at 1,000 years for the four different source regions, base-case flow field.

3.3.1 Downward Transport toward the Water Table

3.3.1.1 Base-Case Flow Field

Figures 3.3-2 through 3.3-4 show the total time dependent flux of C-14, I-129, and Tc-99 from the vadose zone to the saturated zone for the four source classifications using the base-case, steady flow field (5_1_50). The exponential rapid-release model described in Section 3.1.5 controls the release of all three nuclides. This produces flux-versus-time curves that peak in less than 10,000 years. A solubility-limited release would produce flat flux curves with no peak that extend for the duration of the inventory lifetime. The transient flux information is supplied as input to the saturated-zone model, but is broken into 28 spatial footprints as shown in Figure 3.1-4, so that the spatial distribution produced by the various source regions is maintained.

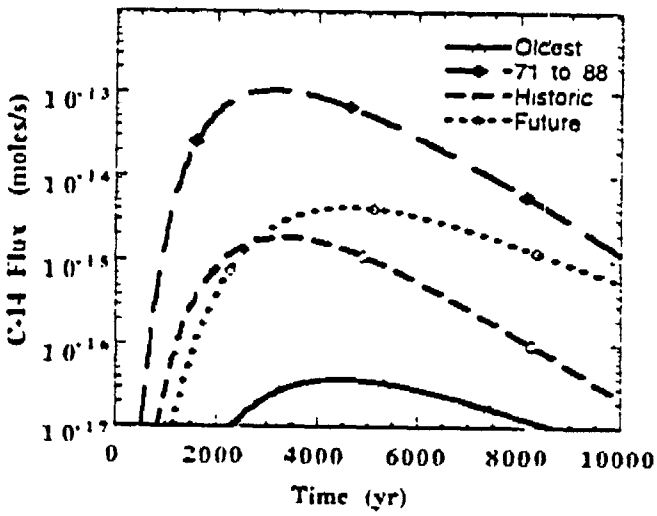

Figure 3.3-2. Total flux of C-14 from the vadose zone to the saturated zone from the four source regions, base-case flow field (5_1_50).

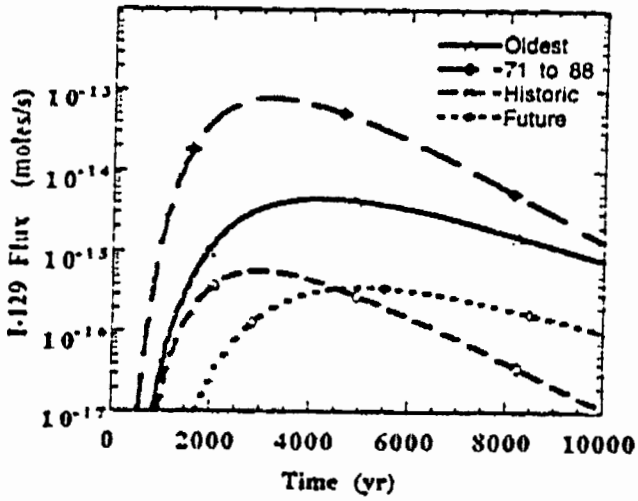

Figure 3.3-3. Total flux of I-129 from the vadose zone to the saturated zone from the four source regions, base-case flow field (5_1_50).

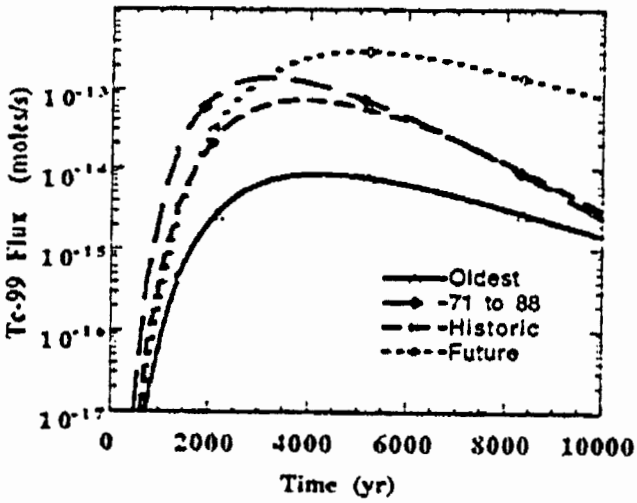

Figure 3.3-4. Total flux of Tc-99 from the vadose zone to the saturated zone from the four source regions, base-case flow field (5_1_50).

For each nuclide and each waste category, the flux is increasing at 1,000 years causing the 1,000-year peak dose to occur at 1,000 years. During the 1,000-year to 10,000-year uncertainty time frame, the peaks in the curves occur at various times, making the prediction of time of maximum dose over this time period less straightforward. For each of the three nuclides, the future inventory arrives latest at the base of the vadose zone because of the increased vadose-zone thickness at the western end of Area G.

3.3.1.2 *Other Flow Fields*

In order to assess the uncertainty in flow rate at the site on the transport results, we examined the transport of I-129 for the historical source for different flow rates and compared the flux from the vadose zone. Figure 3.3-5 shows the total flux of I-129 for five different flow rates as described in Table 3.3-1: 1_1_20, 5_1_20, 5_1_50, 10_1_20, and 10_5_100. By comparing the 1_1_20 case, the 5_1_20 case, and the 10_1_20 case, we see that an increased percolation rate through the mesa results in faster transport through the vadose zone and increased flux to the saturated zone. This flux dependency is compounded by the source release rate, which is highly flux dependent as shown in Figure 3.1-1. The flux at 1,000 years for the lowest flow case (1_1_20) is some five to seven orders of magnitude less than the other cases considered. This case is investigated further to estimate a lower bound dose as part of the uncertainty analysis. By comparing the 5_1_20 case to the 5_1_50 case, we see that additional water in Pajarito Canyon results in faster transport through the vadose zone and increased flux to the saturated zone. The 10_5_100 case represents the flow field with the most water added to the system. This case yields the fastest transport through the vadose zone, the highest flux rate to the saturated zone, and consequently will yield the highest dose over the first 1,000 years. For this reason, we study this case further in the uncertainty analysis to estimate an upper bound dose as part of the uncertainty analysis.

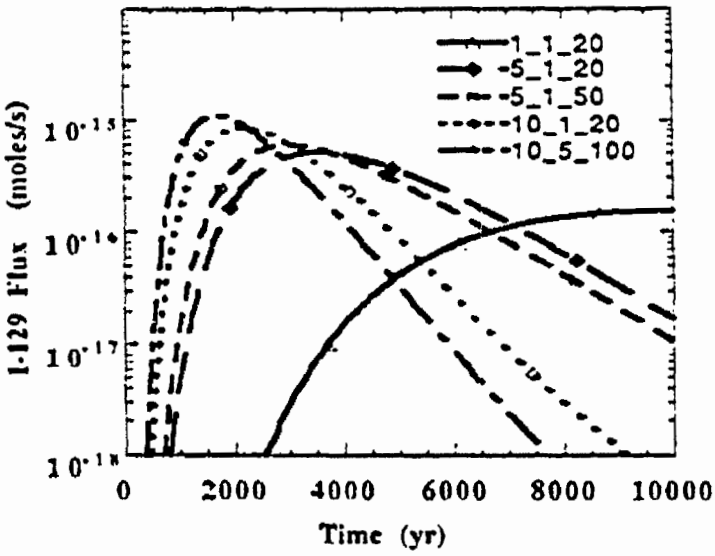

Figure 3.3-5. Total flux of the historical I-129 inventory from the vadose zone to the saturated zone for various flow cases.

Figures 3.3-6 (a), (b), and (c) show the total time dependent flux of C-14, I-129, and Tc-99 from the vadose zone to the saturated zone for the four source regions for the highest-flow case (10_5_100). If these results are compared to those shown in Figures 3.3-2 through 3.3-4 for the base-case flow rate, we see that the high-flow case yields curves that peak earlier and have higher contaminant fluxes to the vadose zone. For the base-case calculations, the time of first arrival was estimated to be at about 600 years. For the high-flow case, this time has decreased to about 300 years.

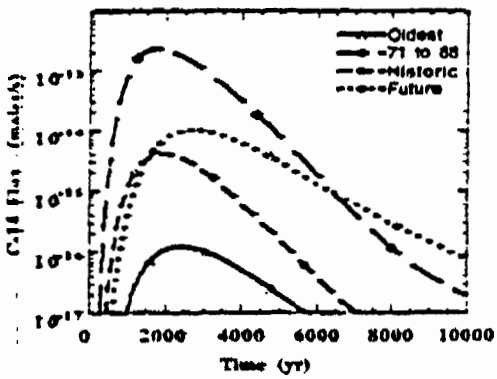

(a)

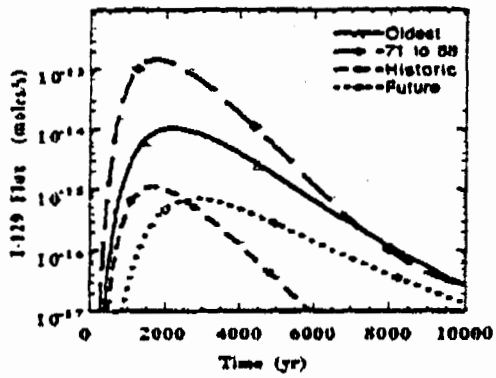

(b)

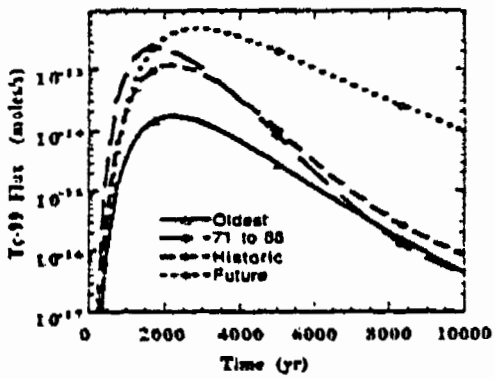

(c)

Figure 3.3-6. Total flux of (a) C-14, (b) I-129 and (c) Tc-99 from the vadose zone to the saturated zone for the highest-flow case (10_5_100) from the four source regions.

Figures 3.3-7 (a), (b), and (c) show the total time dependent flux of C-14, I-129, and Tc-99 from the vadose zone to the saturated zone for the four source regions for the lowest-flow case (1_1_20). If these results are compared to the base-case results (Figures 3.3-2 to 3.3-4), we see that the peak flux values for the low-flow case occur later than 10,000 years. For the base-case calculations, the time of first arrival was estimated to be at about 600 years. For the low-flow case, this time has increased to about 2,000 years, which is later than the 1,000-year compliance period.

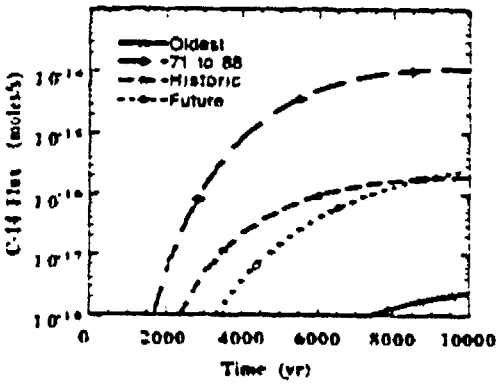

(a)

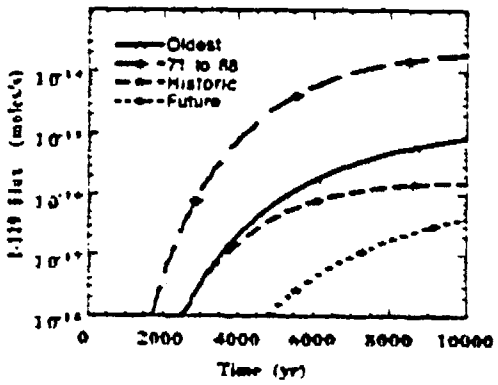

(b)

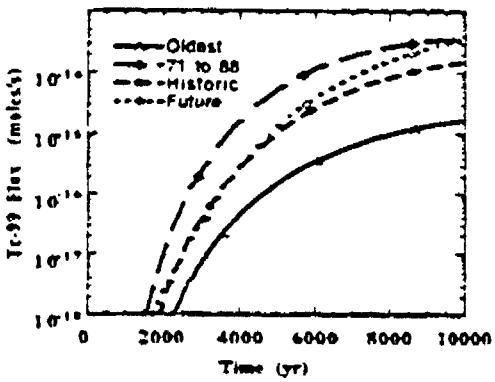

(c)

Figure 3.3-7. Total flux of (a) C-14, (b) I-129, and (c) Tc-99 from the vadose zone to the saturated zone for the lowest-flow case (1_1_20) from the four source regions.

3.3.2 Lateral Transport toward the Mesa Sides

3.3.2.1 *Base-Case Flow Field*

Figures 3.3-8 through 3.3-10 show the simulated results of lateral flux toward the north (Cañada del Buey) and south (Pajarito Canyon) mesa sides for C-14, I-129, and Tc-99. These calculated flux values are expected to be extremely conservative (high) compared to the true flux that occurs at the site for two reasons. First, the simulated lateral transport of the nuclides occurs because of the evaporative boundary condition imposed along the mesa sides. The very low, fixed saturation along the mesa sides causes a strong lateral pressure gradient that pulls water and subsequently the nuclides from the mesa interior toward the edges. Our hypothesis of evaporative processes at Area G is that evaporation occurs ubiquitously within the fractures in the mesa-top units and also along surge beds as discussed in Section 2.4. This hypothesis is supported by the extremely dry mesa-top tuff units (Krier, et al., 1996), by recent chloride and $\delta^{18}O$ profile analyses (Newman, 1996) and by high suction measured along the surge beds (Rogers et al., 1995; also see Figure 2.4-5 in this report). If drying occurs throughout the mesa (as we hypothesize) instead of only at the mesa exterior, the resulting lateral pressure gradient is much weaker, leading to less contaminant transport toward the mesa sides.

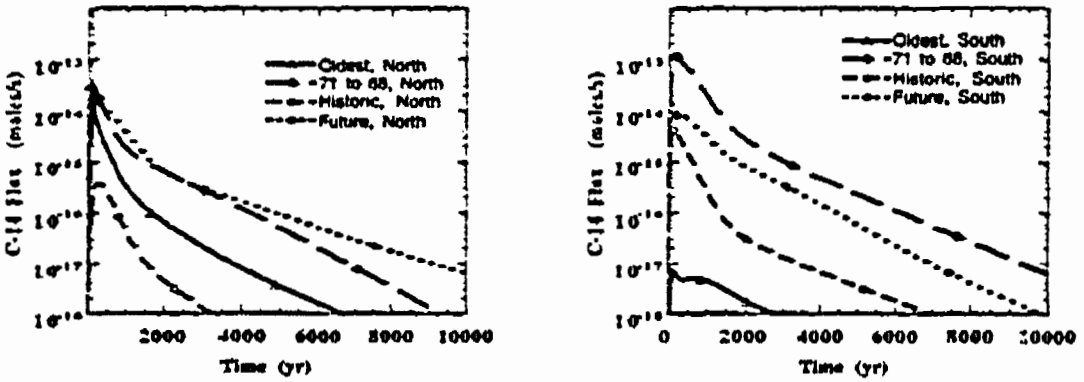

(a) (b)

Figure 3.3-8. Total lateral flux of C-14 toward the mesa sides along (a) Cañada del Buey and (b) Pajarito Canyon from the four source regions, base-case flow field (5_1_50).

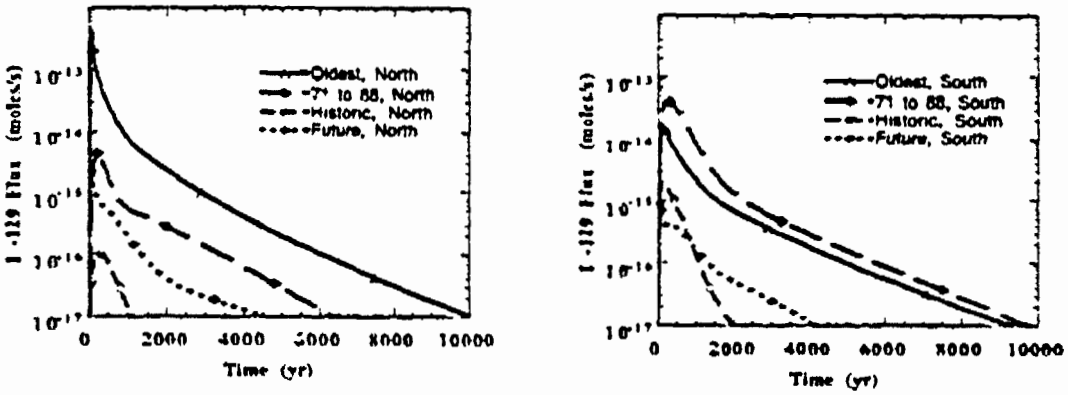

(a) (b)

Figure 3.3-9. Total lateral flux of I-129 toward the mesa sides along (a) Cañada del Buey and (b) Pajarito Canyon from the four source regions, base-case flow field (5_1_50).

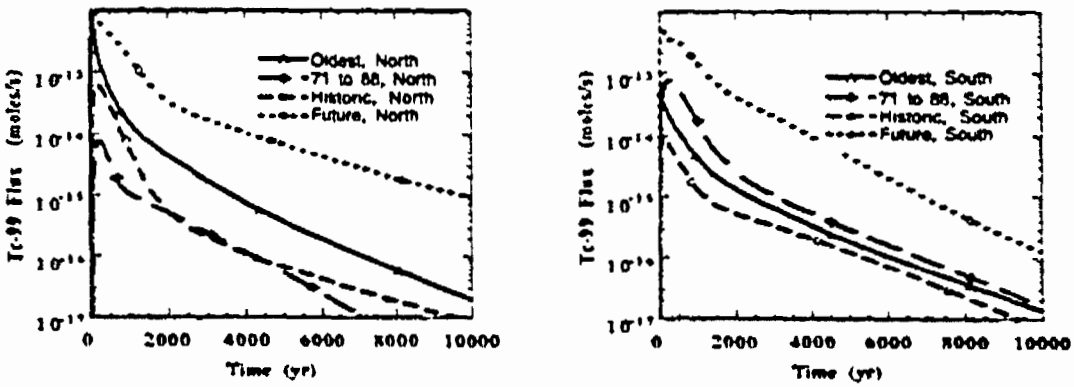

(a) (b)

Figure 3.3-10. Total lateral flux of Tc-99 toward the mesa sides along (a) Cañada del Buey and (b) Pajarito Canyon from the four source regions, base-case flow field (5_1_50).

31

Second, the flux is calculated as though the nuclides exit the system as they reach the mesa edge. In this case, the nuclides would be available for surface transport, perhaps by surface runoff. It is more likely that nuclides would accumulate along the mesa edge rather than moving beyond. Pore water evaporates but the heavy, nonvolatile nuclides will tend to concentrate. This same process happens along other evaporation sites (e.g., fractures) again resulting in less flux at the exterior of the mesa than shown in the calculations. Longmire et al. (1996) have observed elevated chloride, sulfate, and sodium concentrations in pore waters extracted from unsaturated-zone Bandelier tuff samples. They suggest that evaporation leads to the concentration of dissolved species. Newman's (1996) data on chloride and stable isotope concentrations also support this discussion.

The next step in this analysis is to consider the migration of this laterally transported waste to the water table from the two canyon floors adjacent to the site. For the simulations, we conservatively assume that the radionuclide flux out of the mesa sides is immediately available for transport from the canyon floors. This is performed for some generic cases and later scaled to estimate results for the specific cases. As seen in Figures 3.3-8 through 3.3-10, a flux of 10^{-13} moles/s is a typical peak lateral flux value. This value is chosen to represent the generic source term. These figures also indicate a peak flux occurring for a period of about 500 years. Therefore, a generic rapid-release source is modeled as a constant flux of 10^{-13} moles/s for a period of 500 years. The source release begins immediately so that no lag time for the nuclides to reach the mesa sides and then deposit in the canyon floors is included in the analysis.

Separate calculations are run for the two canyons, Pajarito Canyon (south) with a percolation rate of 50 mm/yr and Cañada del Buey (north) with a percolation rate of 1 mm/yr. The flux is applied over areas in the two canyons that represent the areas adjacent to the historic pits (Recorded 1988 to 1995 wastes). Figure 3.3-11 shows the resulting flux-versus-time curves at the base of the vadose zone for this set of calculations. The contaminant that is placed in Pajarito Canyon (south) reaches the water table more quickly than that placed in Cañada del Buey (north) because of the higher percolation rate in Pajarito Canyon. The peak flux occurs after 750 years. The simulated nuclide flux from the vadose zone for waste placed in Pajarito Canyon is used as input to the saturated-zone model so that the maximum possible dose for this mechanism can be predicted. These results are presented in Sections 4.3.2 and 4.3.3. The saturated zone results for the generic rapid-release case (flux rate of $1. \times 10^{-13}$ moles/s into Pajarito Canyon) are scaled by the approximate peak flux values for each of the three nuclides and each of the four waste categories from Figures 3.3-8 through 3.3-10. These scale factors, shown in Table 3.3-1, are used in the formal dose assessment (Shuman, 1997b).

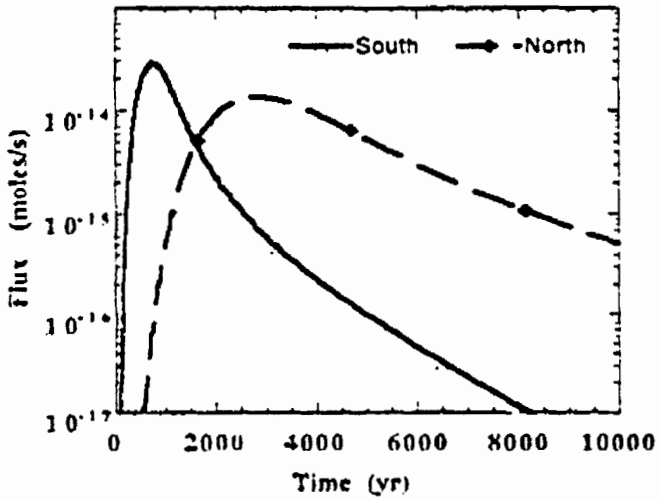

Figure 3.3-11. Generic total flux from the canyon floors through the vadose zone to the saturated zone for an extreme case of lateral transport. Pajarito Canyon (south) flow rate is 50 mm/yr. Cañada del Buey (north) flow rate is 1 mm/yr.

Table 3.3-1. Scale factors to correct generic concentration breakthrough curve for each nuclide and waste category using the base-case flow field (5_1_50).

	C-14	I-129	Tc-99
Oldest	0.0001	0.2	0.4
71 to 88	1.0	0.5	0.8
Historic	0.04	0.02	0.1
Future	0.09	0.005	3.5

32

3.3.2.2 *Other Flow Fields*

For the high-flow case (10_5_100), the simulated lateral transport toward the mesa side is quite similar to the base-case predictions shown in Figures 3.3-8 through 3.3-10. Slightly higher peak fluxes (1 to 4 times higher) of shorter duration are calculated. At this higher flow rate, the mesa-top saturation is higher. This produces a larger saturation gradient between the mesa-top units and the side evaporative (fixed, low-saturation) boundary, causing a stronger capillary pull of contaminated water toward the mesa sides than for the base case. There is, however, a competing advective force. The higher flow rate carries the contaminated water downward twice as fast as in the base case, thus moving it beyond the strong capillary forces exerted along the mesa edges. These factors help to explain the higher peak fluxes of shorter duration. The generic flux curve from Pajarito Canyon to the water table for this case is shown in Figure 3.3-12. The high- and low-flow flux rates shown in Figure 3.3-12 are calculated similarly to that for the base case (a constant source of 10^{-13} moles/s for a period of 500 years with no lag time) except for the background flow field. There is faster breakthrough to the water table because of the higher canyon flow rate of 100 mm/yr. The peak flux occurs after 580 years. Scale factors are shown in Table 3.3-2 for this higher-flow case. These are used in the formal dose assessment to scale results for the generic case of flow through Pajarito Canyon to estimate a worst-case release.

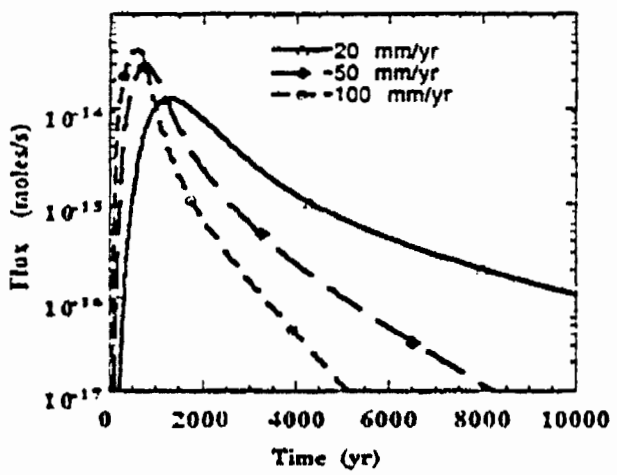

Figure 3.3-12. Generic total flux from the floor of Pajarito canyon through the vadose zone to the saturated zone for an extreme case of lateral transport. Pajarito Canyon flow rates are 100 mm/yr, 50 mm/yr, and 20 mm/yr.

For the low-flow case (1_1_20), the simulated lateral transport toward the mesa side is also similar to the base-case predictions shown in Figures 3.3-8 through 3.3-10. Slightly lower peak fluxes (2 to 4 times lower) with delayed arrival times and of longer durations are calculated. At this lower flow rate, the effects of the capillary and advective forces are the opposite of those explained in the previous paragraph for the high-flow case. Compared to the base case, the capillary pull toward the mesa edge is weaker because the internal mesa-top saturation is lower. The downward advective transport is five times slower than for the base case. The weaker capillary force helps to explain the delayed arrival time and the lower peak values. With the lower flow rate, the contaminated water remains within the strong capillary gradient for a longer time, which causes the longer duration of the flux curve. The generic flux curve from Pajarito Canyon to the water table (Figure 3.3-12) shows slower breakthrough to the water table because of the lower canyon flow rate of 20 mm/yr. The peak flux occurs after 1,290 years. Scale factors are shown in Table 3.3-3 for this lower-flow case. These are used in the formal dose assessment to scale results for the generic case of flow through Pajarito Canyon to estimate a lower bound release.

As in the base case, these calculated flux values are expected to be extremely conservative (high) compared to the true lateral flux that occurs at the site for the two reasons discussed in Section 3.3.2.1.

Table 3.3-2. Scale factors to correct generic concentration breakthrough curve for each nuclide and waste category using the highest flow rate (10_5_100).

	C-14	I-129	Tc-99
Oldest	0.0001	0.3	0.5
71 to 88	2.0	0.6	0.9
Historic	0.06	0.03	0.1
Future	0.2	0.007	6.0

3.3.3 Generic Transport Calculations for Nonradiological Contaminants

The migration of nonradiological contaminants from Area G through the unsaturated zone was modeled through a series of generic simulations. The results of these simulations are used to estimate minimum adsorption coefficients (Kd) that will result in acceptable contaminant breakthrough from the site to the aquifer. These results can be used to predict which nonradiological metals in the inventory may be hazards to the aquifer over the next 10,000 years and which are expected to be less threatening.

Four sets of predictions or cases were run with FEHM using unsaturated-zone input and three-dimensional grid files based on those developed for the PA and CA transport modeling. These four cases include (1) release from the historic pits and shafts assuming the base-case flow field, (2) release from the historic pits and shafts assuming the highest flow field, (3) release from the oldest pits and shafts assuming the base-case flow field, and (4) release from the oldest pits and shafts assuming the highest flow field. In each case, liquid-phase contaminant concentrations in the pits and shafts were held constant at 1.0 mole/l for 10,000-year simulations. The adsorption coefficient of the tuff units and the Puye Conglomerate was modified over a range of values from 0.0 to 1.0 ml/g to predict flux from the unsaturated zone to the aquifer. To ensure that the same mass of contaminant enters a given set of simulations, we assumed that no adsorption occurred on the crushed tuff that fills the pits. The basalt unit was also assumed to be nonsorbing. Only downward transport toward the aquifer is considered.

3.3.3.1 *Simulation Results*

Figures 3.3-13 through 3.3-16 show contaminant breakthrough curves (flux versus time) from the unsaturated zone to the saturated zone for the four sets of generic predictions discussed above and a variety of Kd values. The results demonstrate that a Kd as small as 0.1 ml/g can slow the arrival of a contaminant to the aquifer by over 1,000 years. For example, releases of 10^{-6} moles/s from the historic pits and shafts at the base-case flow rate (Figure 3.3-13) occur at about 1,000 years for Kd = 0, at about 4,000 years for Kd = 0.1, and at about 6,800 years for Kd = 0.2. In Table 3.3-4, we summarize the minimum Kd required in each of the four cases to result in contaminant fluxes after 1,000 years that are three orders of magnitude and six orders of magnitude lower than the peak flux.

Table 3.3-3. Scale factors to correct generic concentration breakthrough curve for each nuclide and waste category using the lowest flow rate (1_1_20).

	C-14	I-129	Tc-99
Oldest	6×10^{-5}	0.04	0.09
71 to 88	0.5	0.2	0.4
Historic	0.01	0.005	0.05
Future	0.03	0.002	1.0

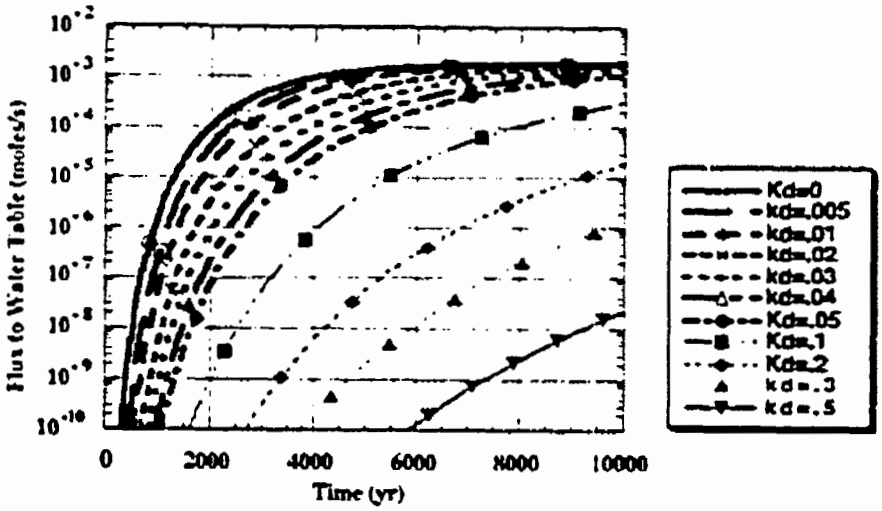

Figure 3.3-13. Total flux from the unsaturated zone as a function of Kd—the plot shows flux as a function of Kd for simulations with a generic source, from the historic pits, and at the base-case flow rate.

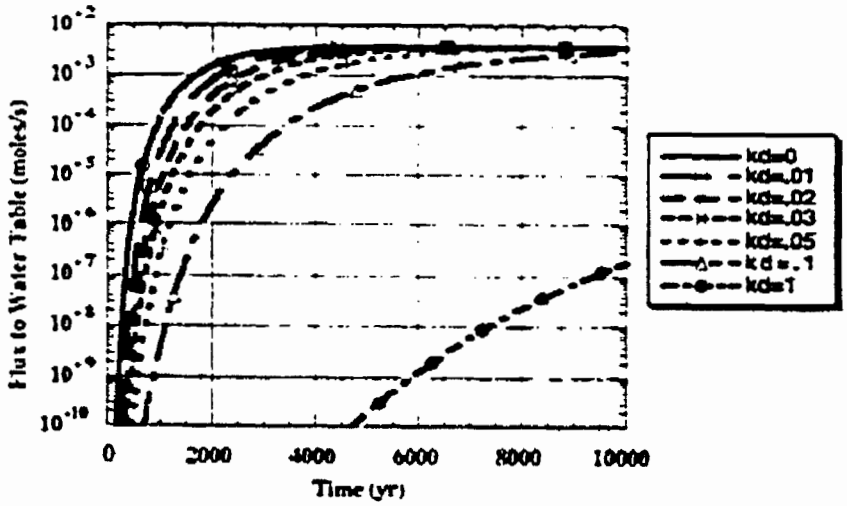

Figure 3.3-14. Total flux from the unsaturated zone as a function of Kd—the plot shows flux as a function of Kd for simulations with a generic source, from the historic pits, and at the base-case flow rate.

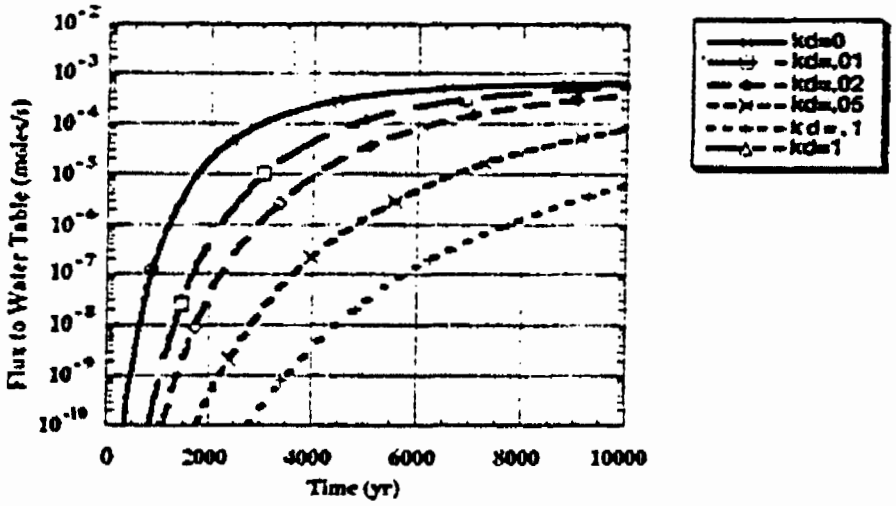

Figure 3.3-15. Total flux from the unsaturated zone as a function of Kd—the plot shows flux as a function of Kd for simulations with a generic source, from the historic pits, and at the base-case flow rate.

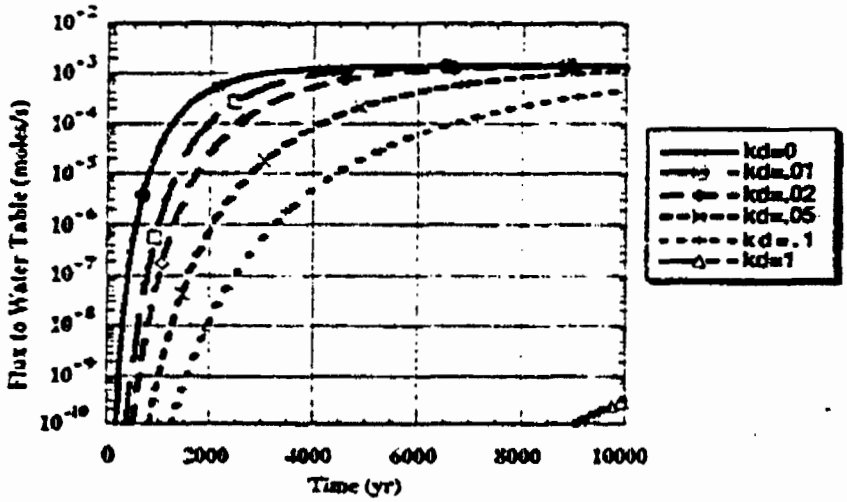

Figure 3.3-16. Total flux from the unsaturated zone as a function of Kd—the plot shows flux as a function of Kd for simulations with a generic source, from the historic pits, and at the base-case flow rate.

Table 3.3-4. Minimum Kd value required to result in a contaminant flux of 10^{-3} times the peak flux value after 1,000 years of migration.		
Case	Kd to result in 10^{-3} x peak flux	Kd to result in 10^{-4} x peak flux
Historic, Base Case Flow	0.0	0.03
Historic, Highest Flow	0.03	0.1
Oldest Base Case Flow	0.0	0.01
Oldest, Highest Flow	.0.2	0.05

The arrival time for the midpoint of a contaminant breakthrough curve is often expressed as a linear function of Kd,

$$t^* = t_o (1 + \rho_b Kd/\theta), \qquad (3.3\text{-}1)$$

where t^* is the arrival time for a retarded contaminant, t_o is the arrival time for a nonretarded contaminant, ρ_b is the bulk density, and θ is the soil moisture content. The arrival time is nonlinear for concentrations (or fluxes) other than the midpoint because of dispersive effects. However, we provide two linear functions that can be used for rough predictions of breakthrough times of sorbing components. These functions are based on the results for the historic source area and the highest flow field shown in Figure 2 because this simulation yields the most rapid transport through the unsaturated zone. For breakthrough that is 10^{-4} times the maximum flux, the estimated arrival time in years is

$$t^* = 240 (1 + 27^* Kd), \qquad (3.3\text{-}2)$$

but for breakthrough that is 10^{-3} times the maximum flux, the estimated arrival time in years is

$$t^* = 540 (1 + 25^* Kd). \qquad (3.3\text{-}3)$$

35

Equations 3.3-2 and 3.3-3 are conservative (i.e., they produce travel times that are less than expected) for Kd values less than or equal to 1.0. For higher Kd values, the coefficients that precede Kd drop, and the estimates are no longer conservative.

3.3.3.2 Discussion of Generic Cases

Because the breakthrough results are based on a constant source concentration, they can be directly scaled for solubility-limited species, assuming that release of the species is solubility limited in all of the pits and shafts. If the species is present only in a fraction of the pits, scaling the results by that fraction can also provide a good estimate. For species controlled by a rapid-release source mechanism, an upper bound contaminant flux can be obtained by estimating a maximum source concentration and scaling the breakthrough curves by that concentration. This approach should be used with caution for rapid-release components because the calculated upper bound may be several orders of magnitude higher than the expected value.

The concentration leaving the unsaturated zone can also be estimated by dividing the flux by the pore velocity and by the footprint area of the source region. In these examples, the pore velocities are the mesa-top infiltration rates of 5 mm/yr for the base case and 10 mm/yr for the highest flow case, and the footprint areas are approximately 23,000 m^2 for the historic pits and 33,000 m^2 for the oldest pits. These areas should again be scaled if only a fraction of the pits contain the contaminant.

The results of this study show the effect of adsorption coefficient on migration rates through the unsaturated zone at Area G from both the historic and oldest disposal units at the base-case and highest flow fields. It is difficult to suggest a minimum Kd value that will result in acceptable releases without knowing the specific compliance period or the regulatory limits on contaminants. However, we can draw the following conclusions for a 1,000-year and 10,000-year compliance period. We define "negligible" in the following conclusion as 10^{-6} times the maximum flux values shown in Figures 1 through 4. We assume that these same results hold for the other two source regions located at Area G.

- For a nonsorbing species, negligible breakthrough should occur for at least 240 years.

- For a compliance period of 1,000 years or less, we believe that the values given in the second column of Table 3.3-4 will sufficiently retard contaminants so that any releases to the aquifer will be negligible. Because a Kd of 0.1 ml/g is the highest value in this table, we propose that value as the minimum Kd value for a 1,000-year compliance period.

- For a compliance period of up to 10,000 years, it appears that a minimum Kd of 1.0 ml/g is sufficient. This value meets our definition of negligible for all but the historic source at the highest flow rate (Figure 3.3-14). In this case, the flux is reduced to almost 10^{-5} times the maximum flux.

- For other compliance periods, Equation (3.3-2) can be used to predict a rough estimate of the minimum Kd required to result in negligible releases.

4. THREE-DIMENSIONAL SATURATED-ZONE MODEL

4.1 SATURATED-ZONE MODEL DEFINITION

The groundwater that percolates through Area G is assumed to flow predominantly downward through the vadose zone and then to enter the main aquifer that underlies the Pajarito Plateau at Los Alamos National Laboratory. This vadose-zone groundwater may be a source of radionuclide contamination to the main aquifer, which in turn may flow to the Rio Grande. The potential levels of contamination in the main aquifer must be predicted in order to perform the PA and CA dose assessments for the site. These predictions of potential contaminant levels are made by modeling the groundwater flow and radionuclide transport with the finite-element code FEHM (Zyvoloski et al., 1995a). The calculations span a 10,000-year time period in order to predict doses in the aquifer for the required 1,000-year compliance period and the 10,000-year uncertainty period.

Although an understanding of the geology and groundwater system under the Pajarito Plateau is still being developed, one hypothesis (Purtymun, 1995) is that the groundwater in the main aquifer beneath Area G flows in a southeasterly direction until it flows into the Rio Grande. The numerical model of the saturated flow beneath Area G assumes that groundwater flow is southeasterly and that the hydrologic properties of the aquifer are homogeneous and isotropic. The groundwater is assumed to discharge from the aquifer to the Rio Grande. The radionuclides potentially entering the main aquifer are assumed to have traveled downward through the vadose zone from Area G. The flux of radionuclides from the vadose zone is predicted (Section 3.3.1) and applied as an upper boundary condition to the saturated-zone model. Although the flow system is simple, we have chosen to use a three-dimensional model in order to maintain the spatial distribution of the four disposal unit classifications (Section 3.1.6).

4.1.1 Geology and Hydrogeology

This brief description of the geology of the Pajarito Plateau is heavily dependent on Purtymun (1995). Purtymun (1984) states that the Rio Grande depression contains over 4570 m (15,000 ft) of volcanics and sediments that overlie the Precambrian crystalline rock. The upper part of the Pajarito Plateau consists of the Tshirege Member, the Otowi Member, the Guaje Member, the Fanglomerate member of the Puye Conglomerate, the Totavi Lentil, the Chaquehui Formation, the Chamita Formation, and the Tesuque Formations interbedded with basaltic rocks of the Chino Mesa and other basalts. The Tschicoma Formation is found to the west of the Pajarito Plateau.

Groundwater under the Pajarito Plateau can be found in the shallow alluvium near the surface, in perched water found above the main aquifer, and in the main aquifer. The main aquifer exists within the Puye Conglomerate (composed of the Fanglomerate member and the Totavi Lentil) and the Santa Fe Group (composed of the Chaquehui Formation, the Chamita Formation, and the Tesuque Formation). It may be unconfined toward the west, but in the east, it appears to be confined and under artesian and semiartesian conditions along the Rio Grande (Purtymun, 1984).

36

The main aquifer is thought to exist to great depth under the Pajarito Plateau but contains usable water (TDS less than 1,000 mg/l) to a depth of 1,830 to 2,130 m (6,000 to 7,000 ft). Salinity of the aquifer increases with depth (Purtymun, 1984). There is no evidence of perched groundwater under Area G or between Area G and the Rio Grande (Devaurs, 1985; Devaurs and Purtymun, 1985).

Waste that enters the saturated zone beneath Area G will enter the fanglomerate member of the Puye Conglomerate. It is expected that the waste will not enter any of the deeper units and will remain contained within the fanglomerate member. This unit consists of volcanic debris with pumice cobbles to boulders in a matrix of silts, clays, and sands. Clay, silt, and pumice lenses are common. The fanglomerate is widespread beneath the Pajarito Plateau. The basalts of the Chino Meso consist of a thick sequence of basaltic to andesitic rock and interflow breccias. They are interbedded with the Chaquehui Formation and the fanglomerate member.

Wells located directly to the northwest of Area G are PM-2, PM-4, and PM-5 within the Pajarito well field. There is no information from wells or outcroppings in the area of interest between wells PM-2, PM-4, and PM-5 and near the Rio Grande where outcropping and water levels found in the river and nearby springs give further information.

In the Pajarito well field, the average saturated thickness of the main aquifer penetrated by the wells is 552 m (1810 ft). The average specific capacity of the field is about 6.46×10^{-3} m^2/s (31.2 gpm/ft) of drawdown, transmissivity is 1.35×10^{-2} m^2/s (93,800 gpd/ft) and the field coefficient of permeability is 2.52×10^{-5} m/s (53.4 gpd/ft^2) (Purtymun, 1995). Purtymun has calculated the rate of movement of water in the top of the main aquifer near Area G as 9.2×10^{-7} m/s (95 ft/yr) based on hydrologic characteristics of the supply and test wells in the Pajarito well field.

Purtymun (1995) states that, based on pumping tests over the screened length of the PM-2 well, the hydraulic conductivity is 1.3×10^{-5} m/s (28 gpd/ft^2). Over the screened length of the PM-4 well, the hydraulic conductivity is 1.1×10^{-5} m/s (24 gpd/ft^2). Over the screened length of the PM-5 well, the hydraulic conductivity is 2.5×10^{-6} m/s (5.3 gpd/ft^2).

Springs exist at the Rio Grande in the Totavi Lentil, the Chaquehui, and the Tesuque. Spring 4A outcrops in the Totavi Lentil at an elevation of 1,698 m (5,570 ft). Spring 4 outcrops in the Totavi Lentil at an elevation of 1,698 m (5,570 ft). Spring 3AA outcrops in the Totavi Lentil at 1,664 m (5,460 ft). Spring 5 outcrops in the Totavi Lentil at 1,698 m (5,570 ft). Spring 3B outcrops in the Tesuque at 1,611 m (5,450 ft). Spring 5A outcrops in the Chaquehui at 1,644 m (5,395 ft). (Purtymun, 1995, p. 287).

Rogers et al. (1996) estimate canyon infiltration rates for the Pajarito Plateau at 0.01 to 0.20 cm/yr beneath dry canyons and 0.01-0.10 cm/yr beneath wet canyons. A rough water balance estimate shows that the volume of vadose-zone water entering the aquifer near Area G is negligible compared to the aquifer volume. Thus, water flux from the vadose zone to the aquifer is not included in the model.

4.1.2 Grid

It is apparent from the preceding discussion of the geology and geohydrology of the Pajarito Plateau that (1) due to interbedded basalts and deltaic and streambed deposition of sediments, there is a great deal of variation of the lithology of the area, and (2) in the area between Area G and the Rio Grande, there are no outcrops or wells to give information about the detailed geology. Therefore, very little geometric detail of the formations is known about this area. For the saturated model of flow beneath Area G, a complicated model is not justified by the current knowledge of the geology and geohydrology. However, a three-dimensional model is warranted to capture the spatial distribution of radionuclide flux from the vadose zone and to approximate dispersive effects.

A rectangular-shaped grid is used to model the saturated zone; 9,773 m (32,063 ft) long extending from just west of Area G to the Rio Grande, 1,280 m (4,199 ft) wide, and 100 m (328 ft) deep (Figure 4.1-1). These dimensions are chosen to capture any potential contamination leaving Area G and moving toward the Rio Grande. The grid is made up of 19,580 nodes and 102,960 tetrahedral elements. Only the upper 100 m of the main aquifer is modeled, which mainly encompasses the bottom of the fanglomerate member. The vertical element width decreases with elevation to better model contaminant plumes entering the top of the saturated zone from the vadose zone. Under Area G, the grid is refined in order to model the solute transport of any radionuclides entering the main aquifer from the unsaturated zone. These elements are 20 m in the groundwater flow direction and 44 m perpendicular to it. This element size was chosen to limit numerical dispersion in the solute transport calculations in the area beneath Area G. We expect an accurate flow solution throughout the grid with an accurate transport solution in the area of interest but some numerical dispersion in the less refined region that extends toward the Rio Grande. The model is oriented at -23° from the x-axis (Figure 4.1-2) in order to be approximately perpendicular to the groundwater equipotentials as shown in Purtymun (1995).

4.1.3 Boundary Conditions

Groundwater flow in the main aquifer is thought to be confined near the Rio Grande and unconfined further west. As an approximation, the main aquifer is modeled as entirely confined. This has a small effect on the total volume of flow through each cross section of the model, but the groundwater velocities, which control the movement of the contaminant plume, are unchanged. The boundary conditions of the model are no flow on top and bottom, no flow along the north and south sides, and fixed pressure along the east and west sides of the model. The pressures at the east and west sides of the model increase with depth to represent constant head conditions and can be related to the equipotentials of the groundwater system by (Strack, 1989):

$$\phi = p/\rho g + \text{elevation}, \qquad (4.1.3\text{-}1)$$

where ϕ is the equipotential, p is the water pressure, ρ is the water density, and g is the gravitational constant. The change in equipotential from east to west is set at 101 m, which corresponds to Purtymun's (1995) equipotentials. Time and position variant contaminant flux from the unsaturated zone is added to the upper boundary as a boundary condition for the transport solution.

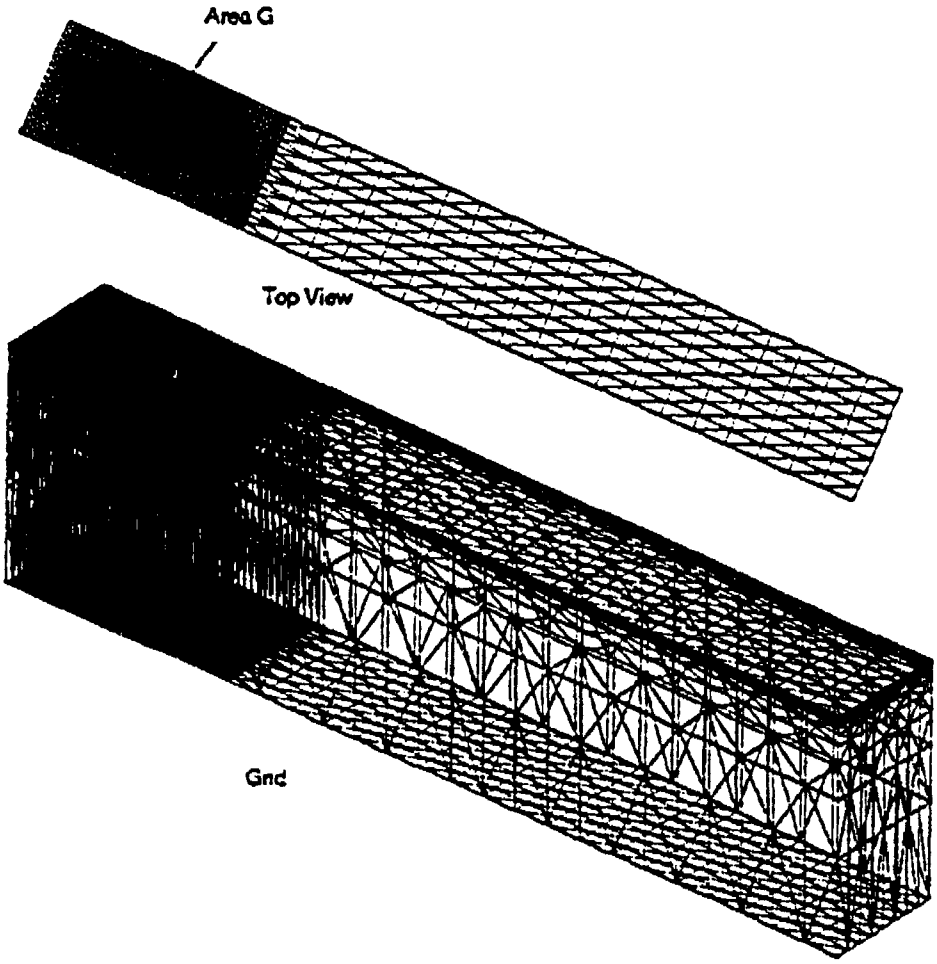

Figure 4.1-1. Three-dimensional finite element grid used for the saturated-zone flow and transport calculations.

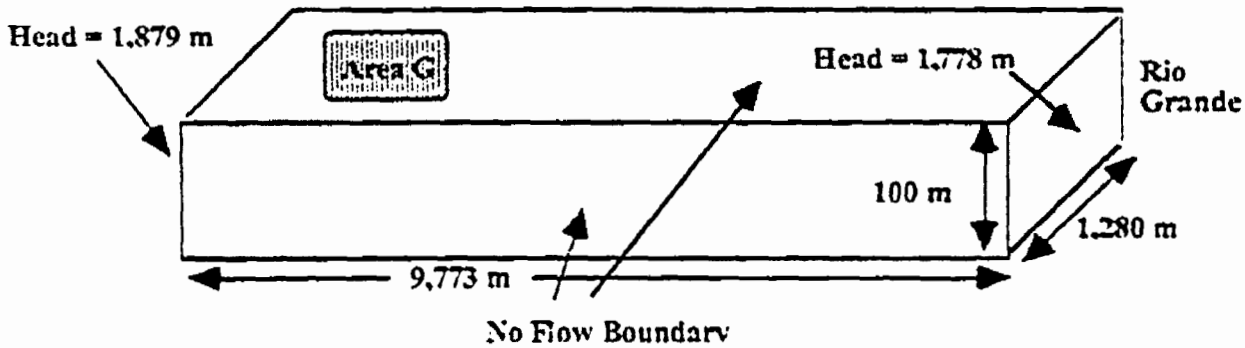

Figure 4.1-2. Saturated-zone model configuration.

4.1.4 Hydrologic and Transport Properties

Purtymun (1984) estimates that the hydraulic conductivity of the Puye Conglomerate is equal to 4.6×10^{-5} m/s. This results in an intrinsic permeability equal to 4.72×10^{-12} m^2. The material is assumed to be isotropic and homogeneous for the modeling with a porosity of 0.25, as described in Section 3.1.4.

The diffusion coefficient for the saturated zone is assumed to be 10^{-9} m^2/s, which is the same value used in the vadose zone at full saturation. Field studies have shown that the dispersivity increases with scale (Neuman, 1990; Gelhar et al., 1992). A dispersivity value of 20 m in the direction of flow and 2 m transverse to the flow are used for the simulations. These values are estimated using an empirical fit to field data developed by Neuman (1990) based on a length scale of interest of approximately 100 m, which is the distance from the Area G boundary to the compliance point. Even larger dispersivity values are justifiable, and the effect is discussed further in the uncertainty analysis presented in Section 5. The dispersivity limits the grid spacing to approximately 20 m (see Section 4.1.2). Table 3.1-4 gives the distribution coefficients that apply in the saturated zone.

4.2 SATURATED-ZONE FLOW RESULTS

A saturated-zone flow field is run to steady state using the boundary conditions described in Section 4.1.3. This results in a Darcy velocity of 52 ft/yr and a linear pressure profile along the direction of flow. The velocity is in the range of those calculated by Purtymun (1995).

4.3 SATURATED-ZONE TRANSPORT RESULTS

4.3.1 Downward Transport toward the Water Table

As discussed in Section 3.3.1, the radionuclide source term for the saturated-zone model is the simulated, time and position variant radionuclide flux that exits the base of the vadose-zone model. Nodes corresponding to the 28 spatial footprints shown in Figure 3.1-4 are defined for the saturated-zone model. This retains the spatial distribution of the four disposal unit classifications described in Table 3.1-5. Figure 4.3-1 shows the simulated aquifer plumes for the historic I-129 inventory assuming the base-case flow field in the vadose zone at 1,000 years and 10,000 years.

Figure 4.3-1. Historic I-129 plume (concentration, moles/liter) in the aquifer for the base-case, vadose-zone flow field: (top) side view at 1,000 years, (middle) top view at 1,000 years, (bottom) top view at 10,000 years.

The side view at 1,000 years shows that the plume disperses throughout the 100-m depth of the model soon after entering the saturated zone. Concentration profiles at the 100-m compliance point show a nearly uniform contaminant distribution with the highest concentration at the water table. This trend applies for the other I-129 source classifications and for the C-14 and Tc-99 simulations. The top views show that the inventory from the historic shafts dominates the aquifer concentration at 1,000 years, but the aquifer concentration is controlled by the various other pit inventories at 10,000 years.

Figure 4.3-2 shows concentration profiles at two locations in the saturated zone again for the historic I-129 inventory. The locations represent the point of maximum dose for the PA waste and the 100-m downstream compliance point. This point is 100 m downstream from the Area G fence line, but approximately 800 m from the location of the historic inventory. This information was submitted to be used in the formal dose assessment (Shuman, 1997b; Hollis et al., 1997). The two curves have the same shape in which dilution and mixing decrease the concentration by a factor of about 3 at the 100-m distance. The curves reflect the vadose-zone contaminant flux curve as shown in Figure 3.3-3. Similar results apply for the other nuclides and source terms. The dilution factor at the 100-m location increases as distance increases (i.e., the future inventory is more diluted at the 100-m compliance point than is the oldest inventory.) Aquifer dilution of vadose-zone concentrations is approximately a factor of 500 between the maximum vadose-zone concentration and the concentration at the 100-m compliance point.

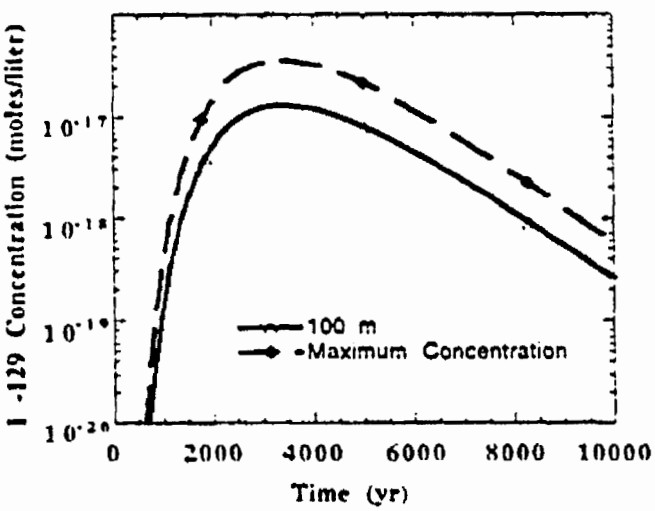

Figure 4.3-2. Concentrations in the saturated zone for the I-129 historic inventory at the point of maximum concentration and at the 100-m compliance point with the base-case flow field in the vadose zone.

4.3.2 Lateral Transport toward the Mesa Side

As shown in Figure 3.3-11, waste that is transported laterally through the vadose zone toward the mesa side and then deposited into Pajarito Canyon reaches the water table more quickly and at a higher flux over the first 1,000 years than waste that is transported laterally and deposited into Cañada del Buey. For this reason, this saturated-zone study focuses on the waste that migrates toward Pajarito Canyon to calculate possible contamination from lateral transport at the water table. Three concentration breakthrough curves are shown in Figure 4.3-3. These represent the time variant aquifer concentration at the location of maximum dose in the saturated zone for the three generic rapid-release cases (flux rate of 1. x 10^{-13} moles/s into Pajarito Canyon): the base case (5_1_50), the highest flow case (10_5_100), and the lowest flow case (1_1_20). These results are scaled by the approximate peak flux values for each of the three nuclides and each of the four waste categories as shown in Tables 3.3-1, 3.3-2, and 3.3-3. The base-case breakthrough curve closely mimics that from the vadose zone (Figure 3.3-11) with a lag time of approximately 50 years, the time for the nuclides to travel through the vadose zone at the canyon flow rate of 50 mm/yr. For each of the three vadose-zone flow cases, this pathway results in higher aquifer concentrations than the downward pathway during the first 1,000 years because we assume an instantaneous release into the canyon floor where the flow rate is higher than through the mesa. The scale factors along with the concentration breakthrough curves are used as part of the formal dose assessment.

The generic concentration curves represent the maximum concentration in the saturated zone beneath Pajarito Canyon adjacent to the historical pits and shafts. The scale factors (Tables 3.3-1 through 3.3-3) are applied to this curve not only for the historic wastes but also for the other three waste categories. In the formal dose assessment, the displacement of the different wastes is not taken into account (i.e., all of the wastes are assumed to enter the saturated zone at the same location), which again overestimates the dose for this pathway. Because the concentration is reported at a location directly beneath the canyon source rather than at a downstream location, the plume is not completely mixed. The concentration at a depth of 100 meters is approximately 10% that at the top of the aquifer.

4.3.3 Dose Assessment

Dose factors were applied to the three-dimensional C-14, I-129, and Tc-99 saturated-zone concentration fields to obtain dose fields. These dose fields were summed to obtain the total ground water dose and the all-pathways dose (for the water component) for the Entire PA Inventory (historic plus future waste) and the Composite Analysis Inventory (CA or all wastes). These calculations were performed in support of the formal dose assessment in order to locate the positions of maximum dose for various combinations of waste inventories. The concentrations of C-14, I-129, and Tc-99 at the locations of the maximum entire PA doses beneath Area G, maximum CA doses beneath Area G, and the maximum entire PA and CA doses at a distance 100 m downstream of Area G were supplied for the formal dose assessment. Table 4.3-1 shows the performance objectives along with the calculated maximum dose values for the base-case flow field and the 10_5_100 flow field at 1,000 years.

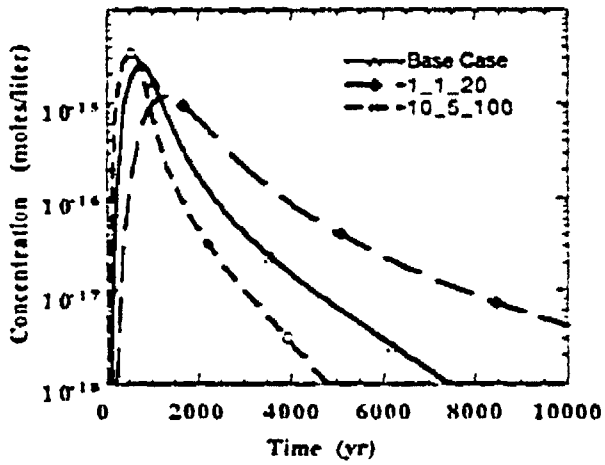

Figure 4.3-3. Time dependent concentration plots for the generic case of lateral transport at the location of maximum concentration in the saturated zone.

It also shows the peak doses during the 10,000-year uncertainty period, which occurs at about 4,500 years for the PA waste and 3,000 years for the CA waste for the base-case flow rate. All doses calculated for nuclides traveling downward through the vadose zone are six or more orders of magnitude lower than the performance objectives. For the low-flow case, doses are negligible because well over 99% of the inventory remains in the vadose zone as shown in Figure 3.3-7.

The full dose assessment for the site is presented in Shuman (1997b). Shuman calculated a higher dose during the first 1,000 years from the waste that is transported laterally to the mesa side than from waste that follows the continuous downward path to the water table. For example, the peak aquifer dose for the base-case, vadose-zone flow field caused by lateral migration toward the mesa side and subsequent deposition into Pajarito Canyon occurs after 800 years. The PA groundwater dose is 4.5×10^{-5}, and the PA all-pathways dose is 1.3×10^{-4}. These doses are higher than those reported in Table 4.3-1, but five to six orders of magnitude lower than the performance objectives. As explained in Section 4.3.2, the earlier arrival time and higher aquifer concentrations for this pathway are due to the assumption of immediate source release into Pajarito Canyon and the corresponding fast canyon recharge rate.

Recall from Section 3.3.2.1 that this pathway is thought to be vastly overestimated. Even still, doses from this route are five to six orders of magnitude less than the performance objectives. A mass balance comparison of the downward and lateral pathways was performed to calculate the possible impact of overestimating the lateral pathway. Over 10,000 years, approximately 30% of

Table 4.3-1. Maximum ground water and all-pathways doses for the PA and CA wastes, base-case flow field (mrem/yr).			
	PA - Ground Water	PA - All Pathways	CA - All Pathways
Performance Objective	4	25	100
1,000 yr (Base Case)	2.4×10^{-7}	6.5×10^{-7}	3.7×10^{-5}
Peak Dose (Base Case)	3×10^{-5} @ ~4500 yrs	1×10^{-4} @ ~4500 yrs	2×10^{-3} @ ~3000 yrs
1,000 yr (10_5_100)	8.0×10^{-6}	2.2×10^{-5}	1.4×10^{-3}
1,000 yr (1_1_20)	9×10^{-12}	2×10^{-11}	1×10^{-10}

the mass leaves laterally compared to the mass that exits at the base of the vadose zone. If this mass were transported downward instead, we would roughly predict a 30% increase in the dose for the downward pathway. As shown in Table 4.3-1, a 30% increase in dose for this pathway is insignificant to the dose assessment.

5 UNCERTAINTY

As in any predictions of the long-term migration of solutes through the subsurface, the results of these transport simulations contain intrinsic uncertainty. Here we will assess what we believe are the more important uncertainties and discuss their impact on the results. The greatest uncertainties associated with predicting aquifer-related doses from Area G are related to our understanding of the mechanisms that control flow and transport within the vadose zone and our ability to model these mechanisms. At this point, we feel that uncertainty associated with the hydrologic processes themselves (conceptual model uncertainty) dominates our ability to make predictions of transport at the site more so than uncertainty associated with the hydrologic and geochemical properties (data uncertainty). However, even with these uncertainties, predicted doses are so comfortably low that we do not expect that the uncertainties discussed below can elevate doses to levels of concern.

5.1 VADOSE-ZONE FLOW

In situ saturation data are difficult to match with any single infiltration rate using our current vadose-zone models, as was shown in Sections 2.1 and 3.2. Environmental tracer data (Newman, 1996) indicate distinct zones of varying flux with very low midmesa water flux rates (0.03 to 0.5 mm/yr) and increased submesa flux rates (0.2 to 5 mm/yr). It is possible that the mesa and the submesa units are not strongly connected hydrologic systems. The wetter saturations beneath the mesa may be the result of recharge from a different source region than from percolation through the mesa top or could represent a wetter climatic period of higher recharge than the present (e.g., during the Pleistocene). Evaporation is clearly an important mechanism controlling midmesa flux rates, yet it

is only indirectly incorporated into the flow modeling through the application of low infiltration rates of 1 to 10 mm/yr. Under this steady, low infiltration rate, the simulations predict a slow but smooth migration of waste through the vadose zone. However, by directly including evaporation in the simulations, the calculated migration of waste through the mesa may behave similarly to that seen with the environmental tracers such as chloride (Newman, 1996) that accumulate within the mesa and have estimated travel times on the order of 1,000 to 17,000 years through the Bandelier Tuff. The mesa itself may act as a dry barrier to downward migration of waste, which could lead to enhanced waste isolation. If this is the case, we expect that the dose estimates made in this report would be higher than if these effects were included.

The mesa-top infiltration rate is the strongest control on the calculated downward migration of waste through the vadose zone. It controls the source release of waste from the disposal units and the subsequent downward migration. We quantified this uncertainty somewhat by considering not only a base-case flow field, but also high- and low-flow cases. As shown in Table 4.3-1, a variation in mesa-top infiltration rate from 1 mm/yr to 10 mm/yr results in a difference in the 1,000-year groundwater-related doses of six orders of magnitude. Clearly, a good understanding of this key parameter is important to the dose assessment. However, because doses are so much less than the performance objectives, a conservative yet realistic value seems adequate for this site.

Other uncertainties are related to flow within the deeper vadose-zone units for which very little hydrologic data are available. Is there lateral flow in the Guaje Pumice bed? Do fractures control water flow through the basalts? The simulation results take almost no credit for transport times through the Cerros del Rio Basalts because we have no knowledge of the flow regime for this unit. Because the basalts make up more than 50% of the vadose zone, this assumption is extremely conservative. The inclusion of more realistic flow and transport properties for this unit is likely to add hundreds if not thousands of years to transport times and to result in lower peak concentrations in the saturated zone. Again, doses related to the groundwater pathways at Area G are orders of magnitude less than the PA or CA performance objectives (Shuman, 1997b). An understanding of the mechanisms that govern flow in the deeper vadose-zone units would greatly enhance our understanding of flow and transport at Area G. However, because the model assumptions concerning flow through these units add conservatism to the very low predicted doses, a more comprehensive model of the deep vadose zone would probably result in further reduction of predicted doses and is therefore not necessary.

The PA and CA transport calculations are based on the steady-flow assumption and on the use of matrix hydrologic properties for all but the basalts at the site. Our understanding of the response of this fractured system to transient flow events is another uncertainty in modeling of the site. The transient calculations (Section 2.2) indicate that the steady-flow assumption is adequate because fluctuations in both saturation and contaminant flux rates dampen with depth even when including fractures in the upper two units. The single fracture infiltration study led us to the conclusion that fracture flow is difficult to initiate (e.g., requires a large source of water) and is short lived once the water source is removed. This conclusion helps justify the use of the matrix hydrologic properties for the transport calculations. Again, we should note that only the upper two tuff units are considered to have significant fracturing (Krier et al., 1996) and that the uppermost unit is excavated during disposal operations. The waste travels through only one highly fractured unit (Unit 1v-u) above the

basalts and even if fracture flow dominates there, the matrix units below will help to attenuate any transient pulses.

Mean values were chosen for the hydrologic properties used in the modeling. Clearly there is some variability in hydrologic properties at the site. In Appendix 2, Orr performed a sensitivity analysis using the minimum and maximum reported hydraulic conductivity values for the units above the Guaje Pumice. In these one-dimensional simulations, he found that vadose-zone travel times vary by approximately ±25% from that calculated using mean values. If travel times are shorter in response to higher conductivity values, predicted doses would be higher because the simulated flux from the vadose zone would be further along the flux-versus-time curves (for example, see Figures 3.3-2 through 3.3-4). This could not elevate doses by more than two orders of magnitude, which is still four orders of magnitude below the performance objectives. However, it is important to point this out as an indicator of our assumptions being less than conservative in favor of our best estimate of the actual system behavior. Heterogeneity in hydrologic properties could lead to preferential flow paths through the vadose zone that could possibly produce faster travel times and regions with more concentrated flux at the base of the vadose zone. However, this waste would be diluted and dispersed in the aquifer, and it is again unlikely that this effect could elevate doses by the six orders of magnitude required to surpass the performance criteria.

5.2 SATURATED-ZONE FLOW

The saturated zone is modeled as a homogeneous and isotropic, single medium. However, the true system has interbedded basalts in the Puye Conglomerate. As described above, heterogeneity can lead to preferential flow paths that can yield higher aquifer concentrations. Aquifer concentrations are, however, limited by the flux of nuclides through the vadose zone and even at the point of maximum calculated dose in the aquifer, doses are again six orders of magnitude less than acceptable limits.

The aquifer velocity used in the simulations is 16 m/yr. Purtymun's (1995) estimated aquifer velocity of 29 m/yr would advect the plume more quickly toward the compliance point. However, the plume would be diluted by approximately a factor of two from the current calculation. Again, this effect is small because of the very fast travel time through the aquifer. One other uncertainty is related to the modeled aquifer depth. The plume disperses throughout the entire modeled depth of 100 meters. Had the depth been increased, the plume would have dispersed even further with a corresponding decrease in concentration. This aquifer depth produces conservative (higher) concentrations.

5.3 TRANSPORT PROPERTIES

The transport simulations are very sensitive to the value of the distribution coefficient, Kd. Uncertainty in this parameter for weakly sorbing nuclides is a data uncertainty that can play an important role in the results of the transport simulations and the subsequent human dose assessment calculations. According to our simulations, a nuclide with a Kd of approximately 2.5 or higher will not reach the saturated zone within 10,000 years. Previous simulations (Birdsell et al., 1995) indicate that a Kd value as low at 0.3 will retard nuclides sufficiently to prevent breakthrough to the aquifer

within 1,000 years. Site-specific values for several nuclides (Longmire et al., 1996) that have large inventories or were expected to have low distribution coefficients were measured in order to decrease the uncertainty in the transport predictions that results from data uncertainty for this parameter.

Longitudinal and transverse dispersivity values of 20 m and 2 m were used for the saturated-zone modeling. Larger dispersivity values are justifiable based on the distance of the pits to the 100-m compliance point. For example, the oldest pits are located approximately 180 m from the compliance point, but the future pits are on the order of 1,300 m from the compliance point. These distances lead to longitudinal dispersivity values ranging from 24 m to 130 m and transverse values ranging from 2.4 to 13 m based on Neuman's (1990) empirical fit to field data. Source-appropriate dispersivity values for the four source regions could have been applied. The effect of increasing the dispersivity on the simulated concentrations is that an increase in the longitudinal dispersivity would result in a faster arrival time for the plume's leading edge. Increases in both the longitudinal and transverse dispersivities would lead to a lower peak concentration. The dispersivity values used for the saturated-zone modeling yield conservative results for the dose assessment.

6 CONCLUSIONS

Numerical simulations are used to predict long-term migration rates of radionuclides for the Area G performance assessment and composite analysis. Results of the calculations show that only the three nonsorbing nuclides C-14, I-129, and Tc-99 reach the aquifer during the 1,000-year compliance period or the 10,000-year uncertainty period. Doses resulting from the aquifer concentrations of these three nuclides are six or more orders of magnitude less than the performance objectives for the site. As in any predictions of the long-term migration of solutes through the subsurface, the results of these transport simulations contain intrinsic uncertainty. However, even with these uncertainties, predicted doses are so comfortably low that we do not expect that the uncertainties described above can elevate doses to levels of concern.

These predictions require calculations of transport through the vadose and saturated zones. The two domains are simulated separately with the spatial and temporal flux leaving the vadose zone applied as input to the saturated zone. Both domains use steady flow fields. A range of vadose-zone flow rates were simulated in order to address the effect of uncertainty in the infiltration rate on aquifer concentrations. All flow fields produced very low aquifer concentrations.

Numerical studies were used to better understand vadose-zone flow through the dry mesa-top environment at Area G. These studies helped define the final model used to model flow and transport through the vadose zone. The study of transient percolation indicates that a steady-flow vadose-zone model is adequate for computing contaminant flux to the aquifer. The fracture flow studies and the investigation of the effect of basalt and pumice properties helped us define appropriate hydrologic properties for the modeling. Finally, the evaporation study helped to justify low infiltration rates.

ACKNOWLEDGMENTS

The authors would like to thank the following individuals for their assistance. Bruce Robinson wrote the subroutines to calculate source term and flux between the vadose-zone and saturated-zone models, and Bruce Robinson and George Zyvoloski provided technical discussions and assisted with running FEHM. Carl Gable carried out grid generation and graphics, and Dave Vaniman, Greg Cole, and Dave Broxton assisted in the construction of the geologic surfaces of the vadose zone. Mira Bussod-Dimitrijevic defined surface boundary conditions based on topography, David Rogers reviewed the document and provided many useful comments, and Janet Harry provided simulation support. The entire Area G PA team (Diana Hollis, Rob Shuman, Erik Vold, Everett Springer, Don Krier, David Rogers, Pat Longmire and Brent Newman) took part in the many technical and organizational discussions that have led to the success of this project.

7 REFERENCES

Barnard, R.W., and H.A. Dockery, "Technical Summary of the Performance Assessment Calculation Exercises for 1990 (PACE90)," Sandia National Laboratories report SAND 90-2726 (1991).

Birdsell, K.H., W.E. Soll, N.D. Rosenberg, and B.A. Robinson, "Numerical Modeling of Unsaturated Groundwater Flow and Radionuclide Transport at MDA G," Los Alamos National Laboratory document LA-UR-95-2735 (1995).

Birdsell, K.H., W.E. Soll, K.M. Bower, A.V. Wolfsberg, T.W. Orr, and T.A. Cherry, "Simulations of Groundwater Flow and Radionuclide Transport in the Vadose and Saturated Zones Beneath Area G, Los Alamos National Laboratory," Los Alamos National Laboratory document LA-UR-97-157 (1997).

Bishop, C.W., "Hydrologic Properties of Vesicular Basalt," Masters thesis, University of Arizona (1991).

Bowen, B.M., "Los Alamos Climatology," Los Alamos National Laboratory report LA-11735-MS (1990).

Broxton, D., Los Alamos National Laboratory, personal communication, 1996.

Carsel, R.F., and R.S. Parrish, "Developing Joint Probability Distributions of Soil Water Retention Characteristics," *Water Resources Research* 24, 755–769 (1988).

Conca, J.L., and J. Wright, "Diffusion and Flow in Gravel, Soil, and Whole Rock," *Applied Hydrogeology*, Vol. 1, No. 1, pp. 5–24 (1992).

Devaurs, M., "Core Analyses and Observation Well Data from Mesita del Buey Waste Disposal Areas and in Adjacent Canyons," Los Alamos National Laboratory document LA-UR-85-4003 (1985).

Devaurs, M., and W. D. Purtymun, "Hydrologic Characteristics of the Alluvial Aquifers in Mortandad, Cañada del Buey, and Pajarito Canyons," Los Alamos National Laboratory document LA-UR-85-4002 (1985).

Frenzel, P.F., "Geohydrology and Simulation of Groundwater Flow near Los Alamos, North-Central New Mexico USGS," Water-Resources Investigations report 95-4091 (1995).

Gable, C.W., T. Cherry, H. Trease, and G. A. Zyvoloski, "GEOMESH Grid Generation," Los Alamos National Laboratory document LA-UR-95-4143 (1995).

Gelhar, L.W., C. Welty, and K.T. Rehfeldt, "A Critical Review of Data on Field Scale Dispersion in Aquifers," *Water Resource Research* 28, 1955–1974 (1992).

Hollis, D., E. Vold, R. Shuman, K. Birdsell, K. Bower, W. Hansen, D. Krier, P. Longmire, B. Newman, D. Rogers, and E. Springer, "Performance Assessment and Composite Analysis for the Los Alamos National Laboratory Disposal Area G," Los Alamos National Laboratory document LA-UR-97-85, Report-54G-013 (1997).

Klavetter, E.A., and R.R. Peters, "Estimation of Hydrologic Properties of an Unsaturated Fractured Rock Mass," Sandia National Laboratory report SAND84-2642 (1986).

Krier, D., Los Alamos National Laboratory, personal communication, 1996.

Krier, D., R. Longmire, and H.J. Turin, "Geologic, Geohydrologic and Geochemical Data Summary of MDA G, TA-54, Los Alamos National Laboratory," Los Alamos National Laboratory document LA-UR-95-2696 (1996).

Longmire, P., C.R. Cotter, I.R. Triay, J.J. Kitten, C. Hall, J. Bentley, D. Hollis, and A.I. Adams, "Batch Sorption Results for Americium, Neptunium, Plutonium, Technetium, and Uranium Transport through the Bandelier Tuff, Los Alamos, New Mexico," Los Alamos National Laboratory document LA-UR-96-4716 (1996).

Montazar, P., and W. E. Wilson, "Conceptual Hydrologic Model of Flow in the Unsaturated Zone, Yucca Mountain, NV," Water Resources Investigations report 84-4355, U.S. Geological Survey (1984).

Neuman, S.P., "Universal Scaling of Hydraulic Conductivities and Dispersivities in Geological Media," *Water Resources Research* 26, 1749–1758 (1990).

Newman, B., "Vadose Zone Water Movement at Area G, Los Alamos National Laboratory, TA-54: Interpretations Based on Chloride and Stable Isotope Profiles," Los Alamos National Laboratory document LA-UR-96-4682 (1996).

Nilson, R.H., E.W. Peterson, K.H. Lie, N.R. Burkhard, and J.R. Hearst, "Atmospheric Pumping: A Mechanism Causing Vertical Transport of Contaminated Gases Through Fractured Permeable Media," *J. of Geophysical Research*, 96, B13, 21933–21948 (1991).

Purtymun, W.D., "Geologic and Hydrologic Records of Observation Wells, Test Holes, Test Wells, Supply Wells, Springs, and Surface Water Stations in the Los Alamos Area," Los Alamos National Laboratory report LA-12883-MS (1995).

Purtymun, W.D., "Hydrologic Characteristics of the Main Aquifer in the Los Alamos Area: Development of Groundwater Supplies," Los Alamos National Laboratory report LA-9957-MS (1984).

Rogers, D.B., Los Alamos National Laboratory, personal communication, 1996.

Rogers, D.B., and B.M. Gallaher, "The Unsaturated Hydraulic Characteristics of the Bandelier Tuff," Los Alamos National Laboratory report LA-12968-MS (1995).

Rogers, D.B., E.L. Vold, and B. M Gallaher, "Bandelier Tuff Hydraulic Characteristics from Los Alamos National Laboratory Borehole G-5 at MDA G, TA-54," *New Mexico Geologic Society Guidebook, 47th Field Conference, The Jemez Mountains Region*, 413–420 (1996).

Rogers, D.B., B.M. Gallaher, and E.L. Vold, "Vadose Zone Infiltration beneath the Pajarito Plateau at Los Alamos National Laboratory," Los Alamos National Laboratory document LA-UR-96-485 (1996).

Rogers, D.B., P. Longmire, B.D. Newman, K.H. Birdsell, W.E. Soll, and E.L. Vold, "Conceptual Model for Subsurface Transport at MDA G," Los Alamos National Laboratory document LA-UR-97-179 (1997).

Rosenberg, N.D., W.E. Soll, and H.J. Turin, "Potential Transport of PCBs through Fractured Tuff at Area G," Los Alamos National Laboratory document LA-UR-94-28 (1993).

Shuman, R., "Radioactive Waste Inventory for the TA-54, Area G Performance Assessment and Composite Analysis," Rogers and Associates Engineering Corp. report RAE-9629/91B-2 (1997a).

Shuman, R., "Radiological Dose Assessment for the TA-54, Area G Performance Assessment and Composite Analysis," Rogers and Associates Engineering Corp. document RAE-9629/91B-1 (1997b).

Soll, W.E., "Influence of Fracture Fills and Fracture Coatings on Flow in Bandelier Tuff," Los Alamos National Laboratory document LA-UR-95-2695 (1995).

Soll, W.E., and K. H. Birdsell, "Influence of Coatings and Fills on Flow in Fractured, Unsaturated Tuff Porous Media Systems," *Water Resources Research* 34, 193–202 (1998).

Springer, E. P., Los Alamos National Laboratory, personal communication, 1996.

Springer, E. P., "Area G Performance Assessment: Surface Water and Erosion," Los Alamos National Laboratory document LA-UR-95-2497 (1995).

Springer, E. P., "Surface Water and Erosion Calculations to Support the MDA G Performance Assessment," Los Alamos National Laboratory document LA-UR-96-4894 (1996).

Strack, O.D.L., *Groundwater Mechanics*, (Prentice Hall, New Jersey, 1989).

Turin, H. J., "Subsurface Transport Beneath MDA G: A Conceptual Model," Los Alamos National Laboratory document LA-UR 95-1663 (1995).

Vaniman, D., G. Cole, J. Gardner, J. Conaway, D. Broxton, S. Reneau, M. Rice, G. WoldeGabriel, J. Blossom, and F. Goff, "Development of a Site-Wide Geologic Model for Los Alamos National Laboratory," Los Alamos National Laboratory internal document (1996).

Vold, E.L., D. Hollis, P. Longmire, E. Springer, K. Birdsell, and R. Shuman, "The Role of a Detailed Aqueous Phase Source Release Model in the LANL Area G Performance Assessment," Los Alamos National Laboratory document LA-UR-96-368 (1996).

Vold, E.L., "Analysis of Liquid Phase Transport in the Unsaturated Zone at a Mesa Top Disposal Facility," Los Alamos National Laboratory document LA-UR-96-370 (1996).

Vold, E.L. and R. Shuman, "Phase Two of the Source Release Modeling or the Los Alamos Area G Disposal Facility Performance Assessment," Los Alamos National Laboratory document LA-UR-96-4786 (1996).

Wang, J.S., and T.N. Narisimhan, "Hydrologic Modeling of Vertical and Lateral Movement of Partially Saturated Fluid Flow in a Fault Zone at Yucca Mountain, NV," Sandia National Laboratory report SAND87-7070 and Lawrence Berkeley National Laboratory report LBL-23510 (1987).

Weeks, E.P., "Effect of Topography on Gas Flow in Unsaturated Fractured Rock," *Flow and Transport through Unsaturated Fractured Rock, AGU Geophysical Monograph* #42, 165–170 (1987).

Wight, J.R., and J.W. Skiles, Eds., "SPUR: Simulation of Production and Utilization of Rangelands. Documentation and User Guide," U.S. Department of Agriculture, Agricultural Research Service report, ARS 63 (1987).

Wood, M.I., R. Khaleel, P.D. Rittmann, A.H. Lu, S.H. Finfrock, R.J. Serne, K.J. Cantrell, and T.H. DeLorenzo, "Performance Assessment for the Disposal of Low-Level Waste in the 200 West Area Burial Grounds," Westinghouse Hanford Company report WHC-EP-0645 (1994).

Zyvoloski, G.A., B.A. Robinson, Z.V. Dash, and L.L. Trease, "Models and Methods Summary for the FEHMN Application," Los Alamos National Laboratory document LA-UR-94-3787, Rev. 1 (1995a).

Zyvoloski, G.A., B.A. Robinson, Z.V. Dash, and L.L. Trease, "User's Manual for the FEHMN Application," Los Alamos National Laboratory document LA-UR-94-3788, Rev. 1 (1995b).

This report has been reproduced directly from the best available copy. It is available electronically on the Web (http://www.doe.gov/bridge).

Copies are available for sale to U.S. Department of Energy employees and contractors from—

Office of Scientific and Technical Information
P.O. Box 62
Oak Ridge, TN 37831
(423) 576-8401

Copies are available for sale to the public from—

National Technical Information Service
US Department of Commerce
5285 Port Royal Road
Springfield, VA 22616
(800) 553-6847

Los Alamos
NATIONAL LABORATORY
Los Alamos, New Mexico 87545